ATOMIC ALKALI LASERS PUMPED BY THE DISSOCIATION OF PHOTOEXCITED ALKALI-RARE GAS COLLISION PAIRS

BY

JASON DANIEL READLE

DISSERTATION

Submitted in partial fulfillment of the requirements
for the degree of Doctor of Philosophy in Electrical Engineering
in the Graduate College of the
University of Illinois at Urbana-Champaign, 2010

Urbana, Illinois

Doctoral Committee:

Professor J. Gary Eden, Chair
Professor James J. Coleman
Professor James M. Lisy
Associate Professor P. Scott Carney
Professor Emeritus Joseph T. Verdeyen

ABSTRACT

A new class of photoassociation lasers has been demonstrated in which photoexcited alkali-rare gas collision pairs dissociate in order to produce inversion on atomic alkali transitions. The pump acceptance bandwidths of these excimer bands, historically referred to as spectral satellites, have been observed to be as broad as $\geq$5 nm. This characteristic makes excimer-pumped alkali-vapor lasers (XPALs) attractive candidates for the spatial mode conversion of laser diode arrays with nominal linewidths of $\sim$2 nm in order to produce high quality ($M^2 \sim 1$) beams. Quantum efficiencies exceeding 98% have been measured and may potentially mitigate heat extraction issues associated with high power, large volume lasers.

XPALs operating on both the $n^2P_{1/2} \rightarrow n^2S_{1/2}$ (D_1) or $n^2P_{3/2} \rightarrow n^2S_{1/2}$ (D_2) transitions of Cs (n = 6) and Rb (n = 5) have been experimentally investigated and show promise for scaling to high power, diode pumped systems. Both semiclassical and quantum mechanical formulations of the free→free transitions which produce satellites are presented, culminating in an improved CsAr($B^2\Sigma^+_{1/2}$) potential. A time-dependent rate equation model is also described which clearly shows the validity and utility of employing the laser itself as a sensitive probe of the underlying photoassociation kinetics.

ACKNOWLEDGMENTS

First and foremost, I would like to thank my family for their unconditional love and support over the years. I never would have gotten this far without them.

I also thank my adviser, Professor Gary Eden, for being a great mentor and making the Laboratory for Optical Physics and Engineering such a fun place to work. His unending enthusiasm and optimism are not only infectious but were invaluable for getting through the tougher parts of graduate school. I am especially thankful for everything he has taught me about clearly communicating my ideas, as this skill has already proven invaluable.

Special thanks to Tom Spinka, my officemate and close friend for the entirety of graduate school. I cannot thank him enough for always being such a great and patient teacher as well as for all of the time he generously spent helping me to better frame my ideas, especially with regards to this thesis. Working and learning with Tom was one of the highlights of graduate school.

Thanks also to Dominic Siriani, my roommate for the past three years. He is a great friend whom I have really enjoyed living with. Not only is he an excellent scientist, but I especially appreciate that he is always up for an adventure.

I wish to also extend my gratitude to Dr. Clark Wagner, the most gifted experimentalist I have ever known. I would not be where I am today without his help, and I will forever brag about the training he gave me. I also know that the lab would not have been nearly as much fun without his enthusiasm, energy, and fantastic pranks. I am similarly indebted to Ellen Keister for her help over the years, experimental and otherwise, especially her careful editing of this thesis. It was an honor to work with Professor Joe Verdeyen, who always treated me as an equal and peer despite his overwhelmingly superior knowledge of plasma and laser physics. The funding provided by AFOSR through grants administered by Dr. Howard Schlossberg and by HEL-JTO through an MRI Program administered by Dr. Michael Berman are gratefully acknowledged.

I would like to thank the following colleagues, past and present, in no particular order: Andrew Price, Tom Galvin, Paul Tchertchian, Jeff Putney, Darby Hewitt, Brittany Zheng, Tom Houlahan, Brenda Li, Hoon Sung, Brian Ricconi, Dr. Sung-Jin Park, and Dr. Dave Carroll. I am also especially grateful for the friendships of Dan Hvala, Jenni Lieberman, John Vericella, Bob Schoonover, Dan Arnzen, and Kate Tobin. I consider myself extremely fortunate to know all of these great people.

Finally, I would like to thank my longtime girlfriend Daphne Kao. Even when we are geographically far apart she is always there to offer loving support and advice. I have often heard that graduate school can be one of the most difficult times in a person's life. Although I did work very hard over the past four years, these people have all helped make them some of my best.

TABLE OF CONTENTS

CHAPTER 1

INTRODUCTION

At the time of this writing, the laser has just reached its 50th birthday. Although incredible advances have been made in laser technology over the intervening years, a high power (MW class), high beam quality ($M^2 \sim 1$), continuous wave (CW), electrically driven laser system operating in the near-infrared has not yet been demonstrated. The multitude of uses for such a system, ranging from industrial processing to military applications, has served as the driving force for efforts to increase the output powers of a variety of laser technologies. Although these efforts have produced extremely valuable tools such as the excimer lasers used today primarily for medical treatments and photolithography [1], to date there is no laser system which meets all of the aforementioned requirements.

Technologies which have successfully met one or more of these requirements include chemical oxygen iodine lasers (COILs) designed for missile defense, which offer MW-class output powers but face significant engineering and operational lifetime challenges because of the requisite hazardous chemicals [2]. Diode laser arrays are another important technology, capable of offering efficiencies approaching 70% and scalable to powers as high as 1 kW CW from a single bar [3], but suffer from extremely poor beam qualities ($M^2 \gg 1$) [4]. Diode-pumped solid state (DPSS) lasers offer a hybrid approach in which a solid state crystal serves as a brightness converter that effectively improves the incident diode beam quality. DPSS lasers with individual output powers as high as 15 kW have been reported, although scaling to higher power typically requires inefficient beam combining of many such systems [5]. Modular design is necessary because of the poor thermal conductivity of the crystal which causes thermal gradients that severely limit beam quality.

An alternative hybrid approach lies in diode-pumped gas lasers. Similar to DPSS systems, these lasers take advantage of highly efficient, scalable diode arrays by utilizing a gaseous medium as a spatial mode converter. However, as opposed to solid state gain media, the relatively low density and extremely fast (ps time scale) collisional processes in gases minimize thermal gradients and dramatically simplify heat extraction. In an effort to realize these advantages, the first of a class of three-level alkali vapor lasers, operating on the long wavelength transition of the first principal series of Rb, was reported in 2003 [6]. The pumping scheme was later demonstrated in both Cs [7] and K [8]. Figure 1.1 depicts the energy level diagram for this laser scheme for Cs. An optical pump tuned to the $6^2P_{3/2} \leftarrow 6^2S_{1/2}$ (D_2) transition of Cs serves to populate the $6^2P_{3/2}$ state. A collisional relaxant, typically a hydrocarbon such as ethane (C_2H_6), then transfers this population to the $6^2P_{1/2}$ state [9]. Lasing occurs on the $6^2P_{1/2} \rightarrow 6^2S_{1/2}$ (D_1) transition.

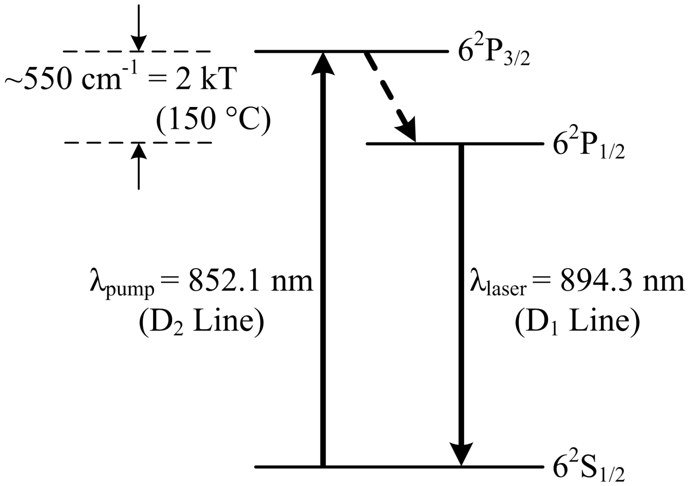

Figure 1.1: Optically pumped three-level laser scheme first demonstrated in Cs. The dashed arrow corresponds to collisional mixing of the upper states.

It should be noted that Fig. 1.1 is not to scale and that the quantum efficiency of this Cs laser is >95%. Cs has the largest energy difference between the $^2P_{3/2}$ and

$^2P_{1/2}$ states among the alkalis (sometimes referred to as an energy defect), with Rb and K having even higher quantum efficiencies of >98% and >99%, respectively. Because quantum efficiency represents the maximum possible efficiency of the laser, this is a critical characteristic. Additionally, these three-level alkali lasers operate in the ~750–900 nm spectral region where high-power, commercial diode arrays are efficient and cost effective [4] and over which there is low atmospheric attenuation [10]. However, because the $n^2P_{3/2} \leftarrow n^2S_{1/2}$ transition has a collisionally broadened linewidth of only ~10 GHz in the presence of $[\mathrm{He}] = 2.4 \times 10^{19}$ cm^{-3} (~1 atm at room temperature), efficient optical coupling with diode arrays, which have typical bandwidiths of ~1 THz, is not possible [11]. Spectrally narrowing the output of diode arrays lowers their efficiency and requires that each diode emitter be electronically locked to the $n^2P_{3/2} \leftarrow n^2S_{1/2}$ transition [12]. A combination of these factors has limited the highest output power yet reported to only 130 W [13].

The work presented in this thesis consists of the demonstration of a new class of photoassociation lasers which offer similar advantages to three-level atomic alkali lasers but do not require spectrally narrow pump sources. This advantage is realized by circumventing direct atomic excitation and instead photoexciting transient alkali-rare gas collision pairs. This produces excimers which subsequently dissociate to populate the excited atomic alkali state. This pumping scheme is referred to as an excimer-pumped alkali-vapor laser (XPAL). The energy diagram of a Cs-Ar XPAL is presented in Fig. 1.2. Two possible laser transitions are indicated in Fig. 1.2, with the dominant transition dependent on the coupling between the members of the 6P doublet.

As indicated by Fig. 1.2, it is possible for an XPAL to operate in the absence of a collisional relaxant. This has numerous advantages, including an increase in quantum efficiency. Also, although hydrocarbons (such as C_2H_6) efficiently transfer population, they pyrolyze over time by reacting with the alkali species to produce alkali-hydrides

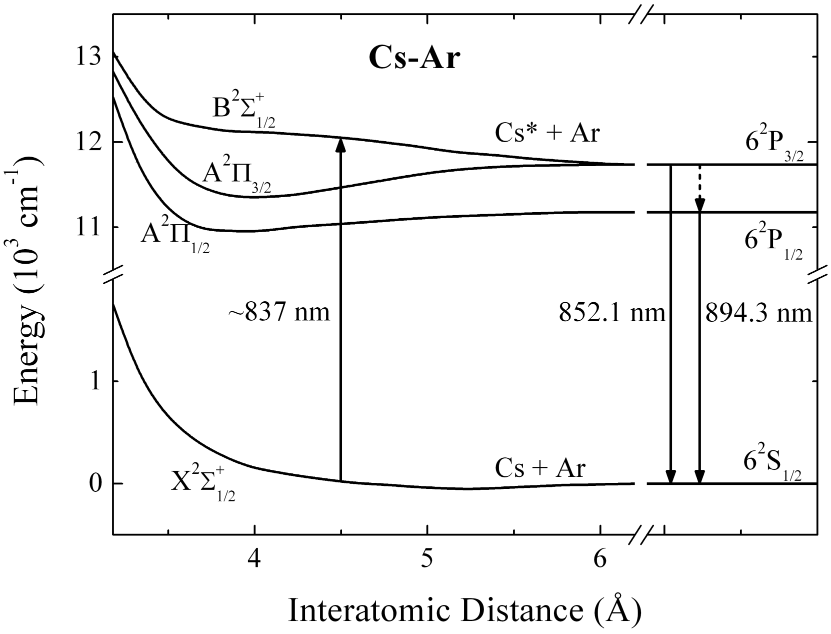

Figure 1.2: Cs-Ar interaction potentials (adapted from [14]) with two possible XPAL transitions indicated. The system is optically pumped near 837 nm and laser action can occur at either 852.1 nm or 894.3 nm. The dashed arrow indicates nonradiative collisional transfer.

(known as laser snow) and carbon (black soot) [15,16]. This degradation process limits the maximum temperature/alkali densities and laser lifetime. Another advantage of removing the collisional relaxant is that it reduces the opportunity for the population to bottleneck in energy levels where other, competing processes may siphon excited species, thereby reducing system efficiency.

Another unique aspect of the pumping scheme illustrated in Fig. 1.2 is that it involves a free→free transition of the molecule. This means that the molecule is never in a bound state and that the collision pairs are formed and dissociated on the picosecond time scale. This characteristic is a key component of the broad pump acceptance bandwidth of an XPAL.

A requirement for XPAL operation is that a region of internuclear separation R must exist in which the classically allowed transition energy between two molecular electronic states varies slowly with R. Such a region is centered near 4.5 Å for the

$B^2\Sigma^+_{1/2}$ and $X^2\Sigma^+_{1/2}$ states in Cs-Ar. This corresponds to spectrally broad features in both absorption and emission which are associated with the atomic transition with which these states are correlated. These spectral features are called satellites and may lie to either the blue or the red of the corresponding atomic transition. Figure 1.3 presents the transmission through a 10 cm cell containing Cs and Ar at a temperature of 460 K, with [Cs] = 1.1×10^{15} cm^{-3} and [Ar] = 1.6×10^{19} cm^{-3}. It is observed that the blue satellite in Fig. 1.3 has a spectral breadth $\geq$5 nm – more than twice the bandwidth of a unbroadened diode array with a linewidth of 2 nm.

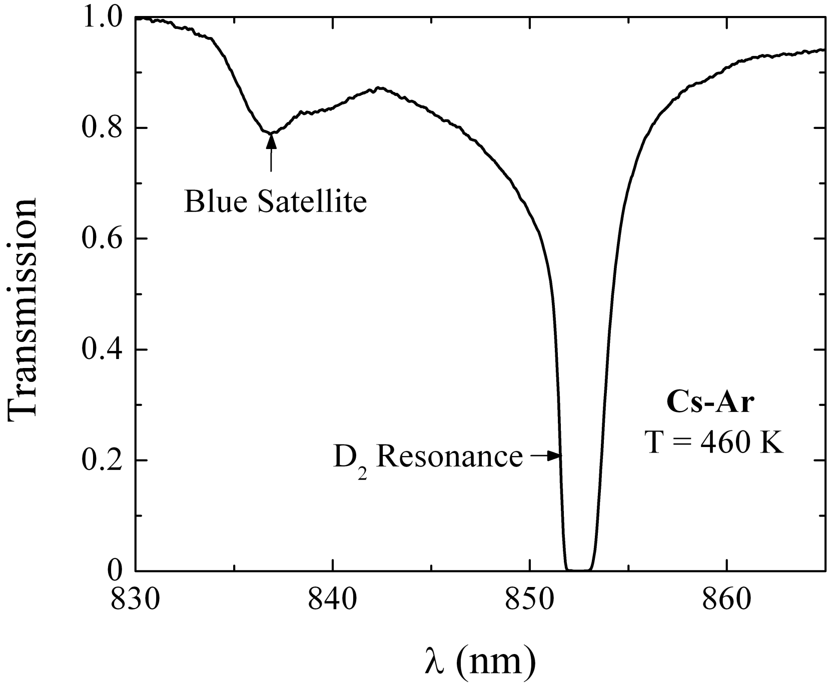

Figure 1.3: Transmission through a 10 cm cell containing Cs and Ar where [Ar] = 1.6×10^{19} cm^{-3}. The temperature of the cell is 460 K, corresponding to [Cs] = 1.1×10^{15} cm^{-3}.

Over the course of this work, several different XPAL variants have been demonstrated. In addition to the experimental work to characterize these lasers, a time-dependent rate equation model has been developed in an effort to further elucidate XPAL laser kinetics and to investigate scaling opportunities. Beyond laser development, XPAL lasers are a sensitive probe of the photoassociation processes which make this pumping scheme possible. In addition to the semiclassical description of photoassociation most commonly employed in the literature, a fully quantum mechanical treatment of free→free transitions is developed and used to provide an improved interaction potential for the $B^2\Sigma^+_{1/2}$ state of CsAr.

Finally, one of the most exciting results to come out of this research was the unexpected observation of three-body photoassocation, which can dramatically alter the lineshape and absorption strength from those of binary gas mixtures. These results represent the least understood component of photoassociation dynamics but may be useful in laser design as well as illuminating weaknesses in the present understanding of transient molecules.

CHAPTER 2

HISTORICAL BACKGROUND

In order to put this work into context, it is important to recognize the key spectroscopic and laser developments that preceded it. It is intended that this brief historical overview will provide additional insight into the key physical processes by clearly differentiating this free→free pumping scheme from previously demonstrated atomic and molecular lasers.

2.1 Excimer Lasers

Although the XPAL acronym contains the word excimer, it it quite distinct from the pumping scheme employed in the traditional class of excimer lasers. In 1970, Basov et al. observed spectral line narrowing at 172 nm in liquid Xe_2 using an electron beam pump [17]. The first conclusive reports of excited dimer (excimer) laser action were reported in gaseous Xe_2, Ar_2, and Kr_2 in 1973 [18, 19]. These demonstrations were followed by the rare gas-halide excimer lasers which were first reported by a number of groups almost simultaneously in 1975 [20–22]. Although, strictly speaking, these heteronuclear molecules correspond to excited complexes or exciplexes, they are still generally referred to as excimers.

The excimer laser transitions occur between a bound excited molecular state and a dissociative molecular ground state as illustrated in Fig. 2.1. An unbound ground state is often observed for diatomic molecules which include a rare gas since its closed-shell configuration makes it chemically inert. However, excitation of the rare gas atom

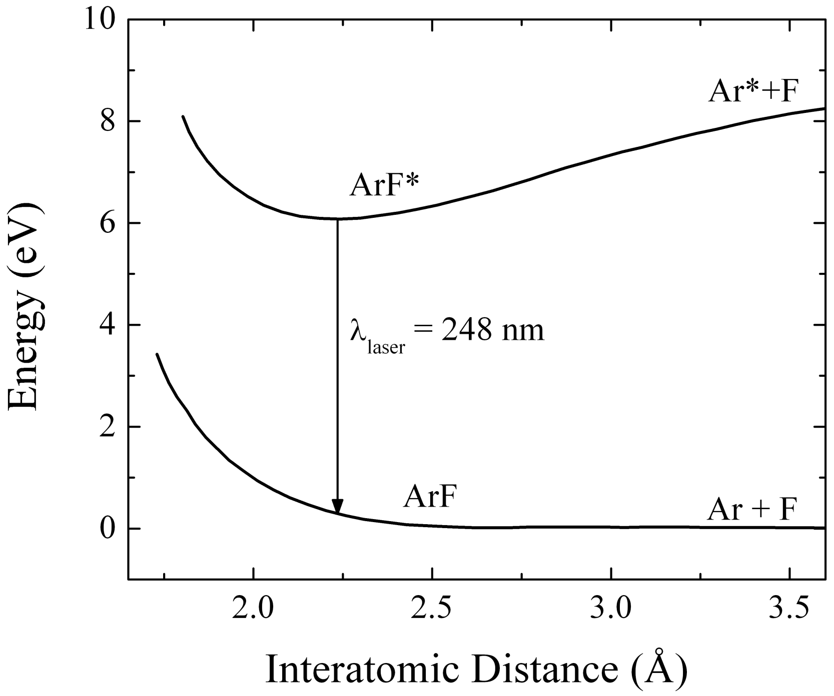

Figure 2.1: Representative energy level diagram of excimer laser operation in ArF where the large arrow indicates the bound→free laser transitions (adapted from [23] and [24]).

(typically with a discharge) changes its electronic configuration to np^5ns, for example, (where $n = 3 - 6$ for Ne – Xe) such that it can form a stable bound diatomic molecule such as ArF*. For sufficiently deep potential wells (such as are observed for the rare gas-halides) with relatively long excited state lifetimes, significant population can be stored in these states. Vibrational relaxation ensures that the system does not behave in a two-level manner and, because the ground state is repulsive, reaching inversion is relatively straightforward. The dominant factor limiting the scaling of these lasers in power is the difficulty in producing uniform, streamer-free discharges in large volumes. Nevertheless, fast dissociation of the ground state molecules allows excimer lasers to have very high throughputs.

Around the same time the first excimer lasers were being demonstrated, A. V. Phelps proposed an alkali-rare gas laser operating in the same manner in mixtures such as Li-Xe, Cs-Ar, and H-He [25]. In these systems, laser action would occur between the $A^2\Pi \rightarrow X^2\Sigma^+_{1/2}$ transitions. This work was further expanded by York and Gallagher in 1974 with particular emphasis on high power laser opportunities [26]. Despite these efforts, these systems were never experimentally realized due in part to the weakly bound (on the order of $\sim$2 $k_B T$) nature of the $A^2\Pi$. This, combined with slow rates of three-body formation, make it extremely difficult to build up enough population in these states to achieve inversion [27]. As excimer laser research slowed dramatically toward the end of the 1970s, interest in these systems faded.

2.2 Spectral Satellites

Prior to the development of the excimer lasers, work was underway to catalog and better understand spectral satellites. Satellites were observed as early as 1927, over 30 years prior to the demonstration of the first laser, and were regarded as a peculiarity in the absorption spectra of gaseous atomic species perturbed by another species [28]. The satellites manifested themselves as spectrally broad absorption bands distinct from the resonance transition or as a strong asymmetry of the atomic line itself [28]. Although the XPAL demonstrations presented here focus primarily on satellites lying to the blue of the D_2 atomic alkali transition, satellites are just as likely to exist to the red. The characteristics of the satellites, including spectral position, breadth, and strength are entirely dependent on the identity and number density of the species involved. A variety of theories describing the origin of satellites were suggested until 1972 when Hedges, Drummond, and Gallagher conclusively attributed red and blue satellites to collision pair photoassociation [29]. As excimer laser research slowed, there was a corresponding reduction in the spectroscopic studies of satellites.

The first report of using satellites as an integral part of a laser pumping scheme was made by in Chilukuri in 1978 using Tl-Hg and Tl-Cd-Ar mixtures [30]. In this work, lasing was observed on the $Tl(7^2S_{1/2} \rightarrow 6^2P_{3/2})$ transition at 535.1 nm by pumping into the red satellite of the $7^2S_{1/2} \leftarrow 6^2P_{1/2}$ transition at 377.6 nm. This laser scheme is presented in Fig. 2.2. Laser action on the same Tl 535.1 nm line by pumping to the blue of the Tl resonance in a Tl-He mixture was reported by Atamas et al. in 1984 [31]. Although both of these laser schemes share several characteristics with the systems that are the subject of this thesis, they differ in that they utilized an intermediate state approximately 1 eV above ground as the lower laser level.

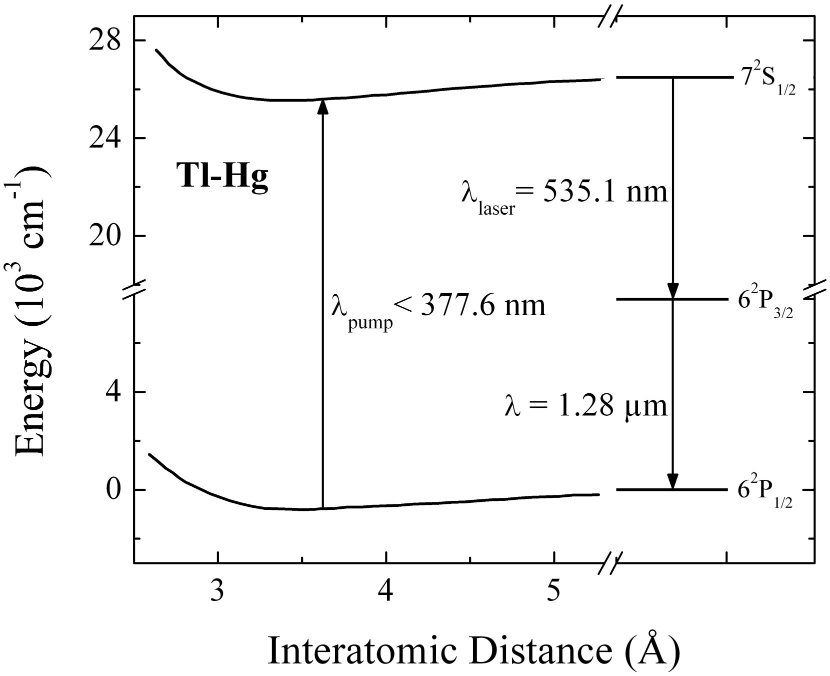

Figure 2.2: Laser pumping scheme demonstrated in Tl-Hg (adapted from [30]).

2.3 Atomic Alkali Lasers

By the late 1990s, laser diode arrays had been developed to the point that they were capable of emitting tens of watts [4]. Since that time output powers and efficiencies have steadily increased, making diodes especially valuable in materials processing applications such as laser welding. As discussed previously in Chapter 1, efforts to develop a hybrid gas-diode system capable of producing high power, high beam quality output led to the first demonstration of a three-level alkali laser in Rb in 2003 [6].

This demonstration employed a Ti:sapphire laser as a surrogate pump source and was followed by the first diode-pumped alkali vapor laser (DPAL) in 2006 [32].

To date, slope efficiencies as high as 68% and optical-to-optical conversion efficiencies as high as 62% have been reported for low power (10 W) Cs DPALs [33]. Although these numbers are very encouraging, coupling diode radiation into the D_2 transition remains the most significant challenge in efficiently scaling to higher powers. There have also been innovations in altering the DPAL kinetics, such as using He as both a means of collisionally broadening the atomic transitions *and* as a collisional relaxant [8, 34]. However, because He provides a $n^2P_{3/2} \rightarrow n^2P_{1/2}$ mixing rate $\sim$20 times smaller than C_2H_6, data suggests that high power, hydrocarbon-free DPAL variants will require extremely high ($\geq$10 atm) partial pressures of He [34]. Pressures of this magnitude dramatically increase the engineering complexity of constructing and heating the gas cell.

The first XPAL was actually demonstrated in a Na-He mix in 2002 by Markov et al. [35]. In this paper, laser action was reported on both the $3^2P_{3/2} \rightarrow 3^2S_{1/2}$ and $3^2P_{1/2} \rightarrow 3^2S_{1/2}$ lines (in some cases simultaneously) when photoexciting Na-He pairs. It is interesting to note that the majority of the results presented in this dissertation were obtained without knowledge of the work done by Markov et al. This is attributed to the different interests and viewpoints of the authors, who considered the system as two perturbed atomic states. Additionally, the authors did not discuss high power laser opportunities or an extension of the technique to other gas mixtures. By evaluating these and other aspects of XPALs, this dissertation builds on the work of Markov et al. who recognized that “A more detailed description of the experiment needs a more developed theory, which should include real interaction potentials of excited and unexcited sodium atoms with helium atoms” [35].

CHAPTER 3

SPECTROSCOPIC FOUNDATION

For over 80 years, spectral satellites associated with atomic resonances have been observed in both the absorption and emission spectra of a wide variety of gas mixtures [28]. Many of these reports observe broad absorptions to the blue side of single photon-allowed atomic transitions, including the principal series of the alkali metals, alkaline earths [36], Tl [37], and In [37] among others. Red satellites are often observed as asymmetrical broadening on the long wavelength side of a transition. A requirement for observation of these satellites is the presence of a collision partner, examples of which include the rare gases, hydrocarbons, N_2, and H_2 [38]. Until recently, only semiclassical investigations concerning satellite origin and behavior have been undertaken. The results of this prior work are briefly reviewed and a fully quantum mechanical treatment of free→free photoassociation is presented, culminating in an improved $\mathrm{CsAr}(\mathrm{B}^2\Sigma^+_{1/2})$ potential.

3.1 Semiclassical Formulation

The origin of satellites was a subject of significant debate in the years following their initial observation. In 1972, Hedges, Drummond and Gallagher developed a quasistatic, semiclassical model which provided an intuitively satisfying picture of the molecular dynamics that lead to satellite observation [29].

For any electronic state of a molecule, there is an associated molecular interaction potential which varies with the internuclear separation R of the composite species.

Consider a diatomic molecule consisting of an absorbing atom of species A and a perturbing collision partner of species B. The difference in potential energy between two electronic states at a given value of R between A and B corresponds to a transition frequency $\nu(R)$. Referring to the two electronic state potentials $V_u(R)$ and $V_l(R)$ (upper and lower, respectively), $\nu(R)$ is given by the Franck-Condon relation

$$\nu(R) = \frac{V_u(R) - V_l(R)}{h}, \tag{3.1}$$

which can be written alternatively as

$$\lambda(R) = \frac{hc}{V_u(R) - V_l(R)}. \tag{3.2}$$

These expressions make use of the fact that electrons move much faster than molecules and, therefore, R remains essentially constant during an electronic transition.

Figure 3.1 shows the $B^2\Sigma^+_{1/2}$ – $X^2\Sigma^+_{1/2}$ difference potential for Cs-Ar. For convenience, transition wavelength is plotted as a function of R. The dashed line corresponds to the 852.1 nm (D_2) atomic Cs resonance. There are two extrema in the difference potential of Fig. 3.1. One, a local minimum, is observed at ∼831 nm on the short wavelength (blue) side of the atomic resonance. A local maximum near ∼853 nm is also observed on the long wavelength (red) side. Both of these turning points correspond to regions where the upper and lower state potentials run parallel to one another. Qualitatively, this would indicate that a number of Cs-Ar pairs with different values of R would have very similar transition frequencies, giving rise to a broad, pronounced spectral feature in either absorption or emission. This is illustrated in Fig. 3.2 in which the reduced absorption coefficient k (cm^{-5}) for Cs-Ar near the D_2 resonance is presented with both the red and blue satellites indicated. It should be noted that the Cs D_2 red satellite is also attributed to pumping of the $A^2\Pi_{3/2}$ molecular state, although the relative population transfer of this process compared to that of $B^2\Sigma^+_{1/2}$ has not been measured.

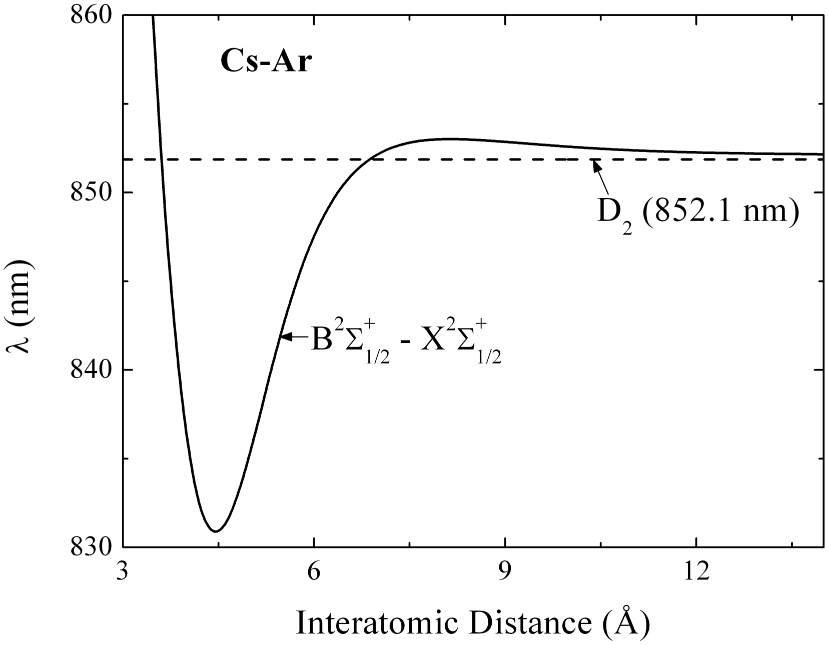

Figure 3.1: $B^2\Sigma^+_{1/2} - X^2\Sigma^+_{1/2}$ difference potential (converted to wavelength in air for convenience) of Cs-Ar.

It is important to note that the value of k presented in Fig. 3.2 is related to the absorption coefficient α (cm^{-1}) by

$$\mathrm{k}(\nu) = \frac{\alpha(\nu)}{[N_A][N_B]}, \tag{3.3}$$

where $[N_A]$ and $[N_B]$ correspond to the number densities of participating species A and B, respectively. Figure 3.3 presents the transmission through a 10 cm cell containing $[\mathrm{Ar}] = 1.6 \times 10^{19}$ cm^{-3} at temperatures of 448 K ($[\mathrm{Cs}] = 6.6 \times 10^{14}$ cm^{-3}), 460 K($[\mathrm{Cs}] = 1.1 \times 10^{15}$ cm^{-3}), and 475 K ($[\mathrm{Cs}] = 1.9 \times 10^{15}$ cm^{-3}). The data in Fig. 3.3 can be converted to α with the expression

$$\alpha(\nu) = -l \log_{10}(T), \tag{3.4}$$

where l is the optical path length through the absorbing medium. Applying this

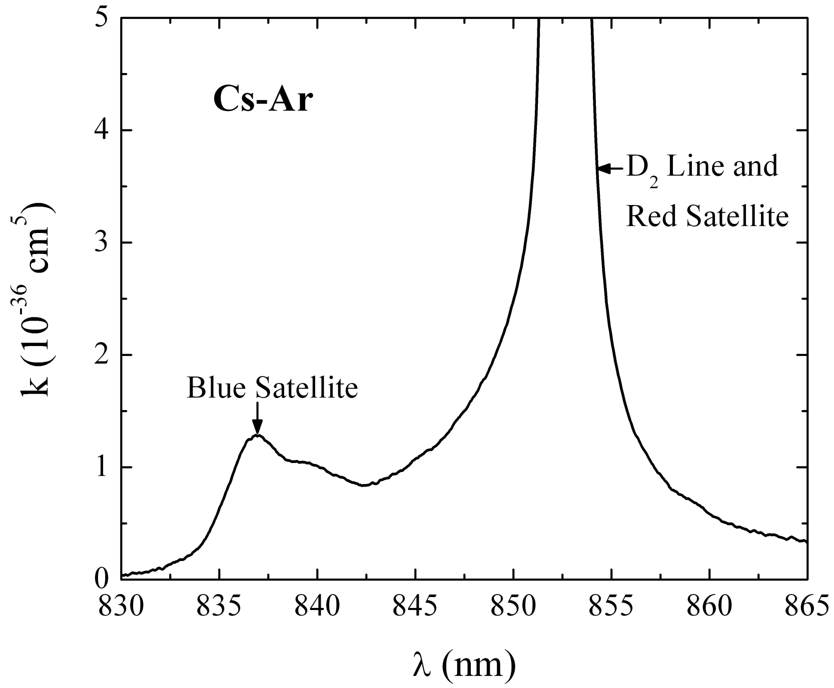

Figure 3.2: Reduced absorption coefficient obtained experimentally from a Cs-Ar mixture with both the red and blue satellites indicated.

formula to Fig. 3.3 leads to the traces of α presented in Fig. 3.4.

For the satellite regions in Fig. 3.4, it can be shown that

$$\alpha(\nu) \propto [N_A][N_B], \tag{3.5}$$

which has several implications. First, one can vary the density of either of the participating species to modify the absorption profile. The density of alkali atoms in a saturated vapor is dependent on the temperature of the system. However, for a perturbing species such as the rare gases, Eqn. 3.5 illustrates how the value of α may also be altered *independently* of temperature. Also, the linear dependence of α on $[N_A]$ and $[N_B]$ indicates that binary contributions to the satellite are the most significant. This assumption is an important component in the semiclassical treatment of satellites [29] and has been comprehensively validated for Cs-Ar [39] .

The value of converting to k from α, such as in Fig. 3.2, is that the resulting

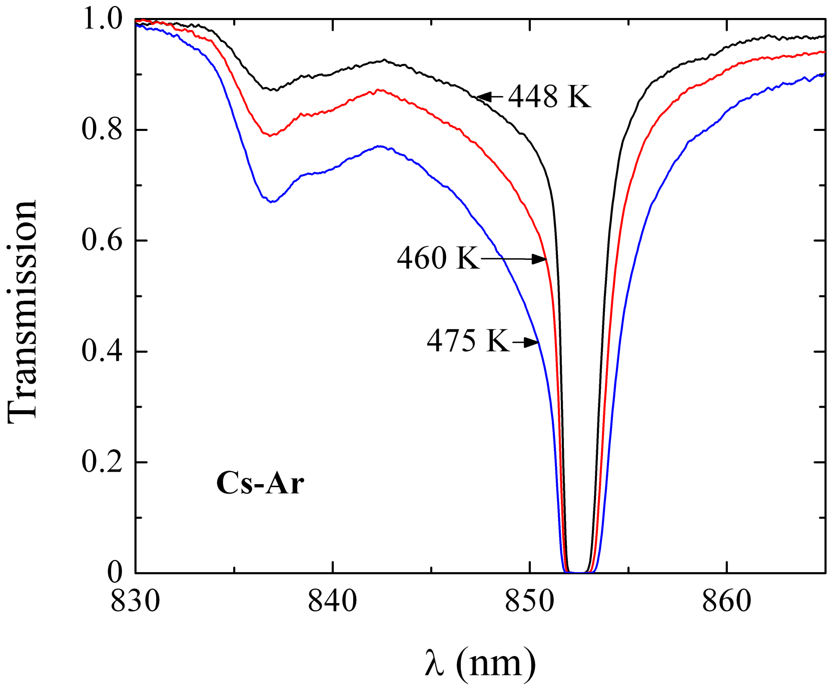

Figure 3.3: Transmission near the D_2 resonance through a 10 cm gas cell containing Cs and and Ar. The cell contains $[\mathrm{Ar}] = 1.6 \times 10^{19}$ cm^{-3} and the temperatures of 448 K, 460 K, and 475 K correspond to $[\mathrm{Cs}] = 6.6 \times 10^{14}$ cm^{-3}, 1.1×10^{15} cm^{-3}, and 1.9×10^{15} cm^{-3}, respectively.

curve is independent of the partial pressures of the participating species. Quantitatively, Hedges et al. showed, starting from Eq. 3.1 and statistical distributions of perturber positions, that the reduced absorption coefficient $\mathrm{k}(\nu)$ of a gas mixture can be calculated from the expression:

$$\mathrm{k}(\nu) \propto \alpha(\nu) \frac{A(R)}{[N_A][N_B]} \frac{1}{|d\nu(R)/dR|}, \tag{3.6}$$

where $A(R)$ is the spontaneous emission rate and is a weak function of R. The term $|d\nu(R)/dR|^{-1}$ indicates the strong dependence of $\mathrm{k}(\nu)$ on the shape of the difference potential. According to Eq. 3.6, $\mathrm{k}(\nu)$ becomes large at any value of R where the derivative of the difference potential approaches zero. As discussed previously, this occurs both to the red and blue of the Cs atomic resonance in Cs-Ar mixtures and is correspondingly observed in the absorption spectra.

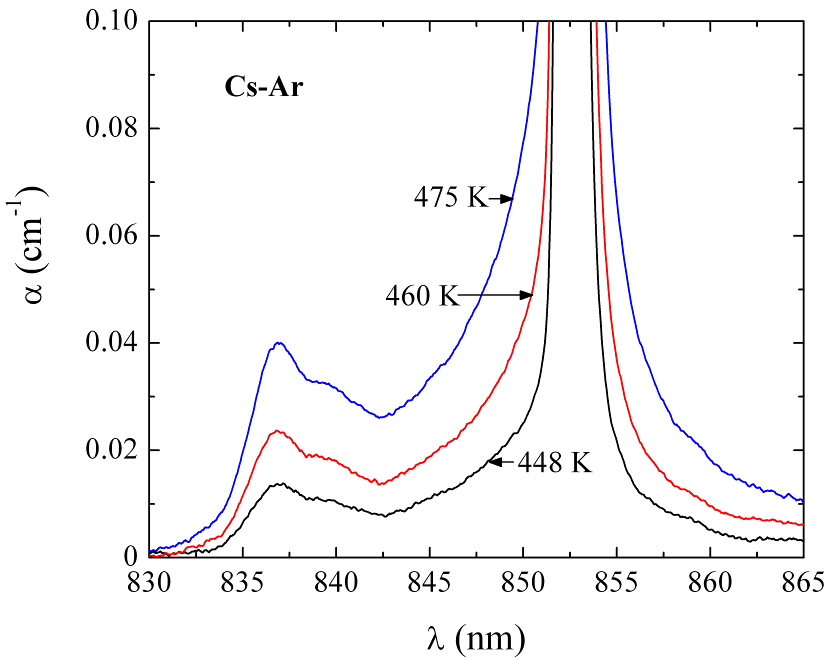

Figure 3.4: Absorption coefficient as a function of λ for a cell containing $[\mathrm{Ar}] = 1.6 \times 10^{19}$ cm^{-3} at temperatures of 448 K, 460 K, and 475 K (corresponding to $[\mathrm{Cs}] = 6.6 \times 10^{14}$ cm^{-3}, 1.1×10^{15} cm^{-3}, and 1.9×10^{15} cm^{-3}, respectively).

As mentioned previously, satellites are by no means limited to Cs-Ar mixtures. For example, Fig. 3.5 compares the $\mathrm{B}^2\Sigma^+_{1/2}$ - $\mathrm{X}^2\Sigma^+_{1/2}$ difference potentials of Cs-Ar with that of Cs-Kr. Similar to the case of Cs-Ar, Cs-Kr is predicted by Fig. 3.5 to have a blue satellite near ∼824 nm and a red satellite near ∼853 nm. This illustrates the sensitivity of a satellite's presence and spectral characteristics to the identities of the species involved.

The prediction of Fig. 3.5 that the Cs-Ar and Cs-Kr satellites peak at different transition wavelengths is demonstrated conclusively in Fig. 3.6. However, despite this qualitative agreement, Fig. 3.5 is quantitatively incorrect as the satellites actually peak at 836.7 nm (Cs-Ar) and 841.1 nm (Cs-Kr). Interestingly, this is opposite the prediction that the blue satellite of Cs-Ar would lie to the red of the Cs-Kr blue satellite. This discrepancy is primarily attributable to limitations in the semiclassical treatment, including the allowance of only transitions which conserve kinetic energy

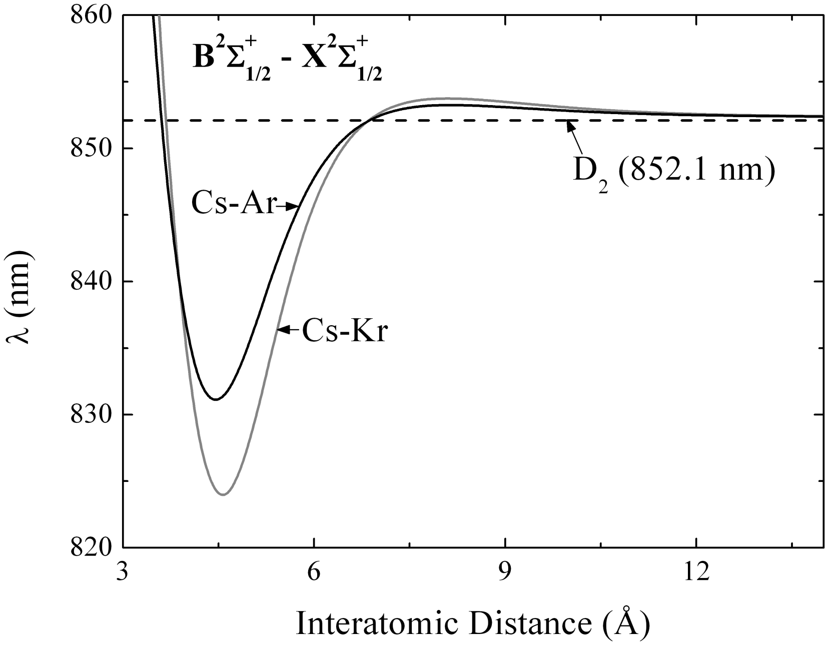

Figure 3.5: Difference potentials for Cs-Ar and Cs-Kr.

and a small probe region in R. Efforts to overcome these limitations by employing a quantum mechanical treatment are discussed in the next section.

3.2 Quantum Mechanical Formulation and Improved CsAr $B^2\Sigma^+_{1/2}$ Interaction Potential

Although the semiclassical treatment provides valuable insight into the origin of spectral satellites, its accuracy is limited by the semiclassical assumptions discussed at the end of Section 3.1. However, modern advances in computers have made a fully quantum mechanical treatment of collision pair absorption computationally tractable. The calculation process leading to the simulation of free→free absorption spectra, which shares many characteristics with those for free↔bound transitions [40–42], will be described. These derivations are followed by a discussion of how to employ these techniques to iteratively improve upon the interaction potentials currently available in the literature. CsAr will be used as a representative species, but this technique is

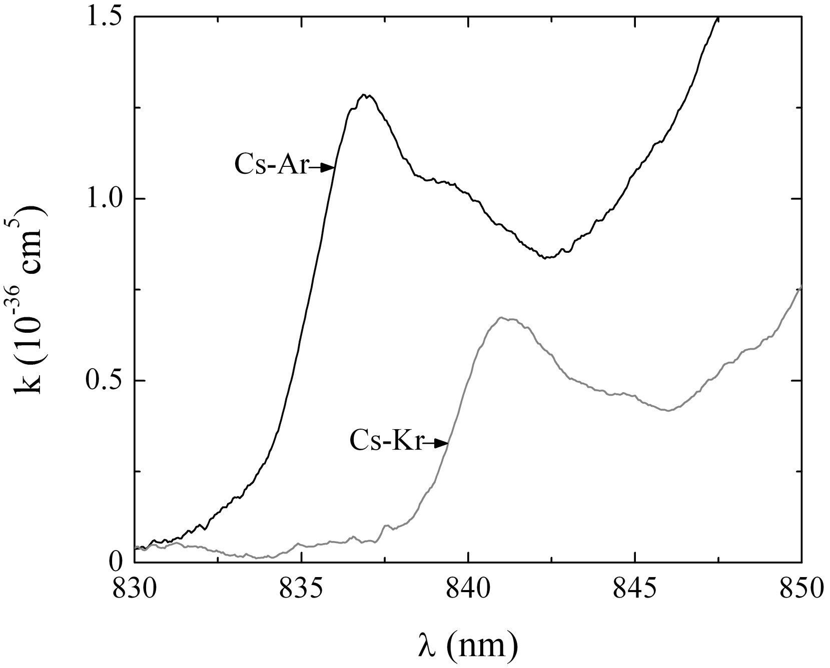

Figure 3.6: Experimental comparison of the reduced absorption coefficient as a function of wavelength in Cs-Ar and Cs-Kr mixtures.

applicable to *any* molecular states photoexcited by free→free transitions.

The most general form of the time-dependent Schrödinger equation is

$$i\hbar\frac{\partial}{\partial t}\psi = \hat{H}\psi = E\psi, \tag{3.7}$$

where $\hat{H}$ is the Hamiltonian operator and E is the total energy of the system. Equation 3.7 may be rewritten for time-independent systems as

$$-\frac{\hbar^2}{2m}\nabla^2\psi + V\psi = E\psi, \tag{3.8}$$

where the $-(\hbar^2/2m)\nabla^2$ term corresponds to kinetic energy and V to potential energy. In order to investigate diatomic molecules using Eqn. 3.8, it is necessary to invoke the Born-Oppenheimer approximation,

$$\psi_{total} = \psi_{nuclear}\psi_{electronic}, \tag{3.9}$$

which states that the total wavefunction of a molecule can be separated into its nuclear and electronic composite wavefunctions. This approximation is valid whenever the nuclei are significantly heavier than the electrons because this allows for the assumption that nuclear positions remain fixed for the duration of electronic energy level transfer.

It is possible to reduce the diatomic two-body problem into a one-body problem by introducing the reduced mass of the pair and performing wavefunction calculations only in the R coordinate. Combining Eqns. 3.9 and 3.8 leads to

$$E\psi_e = -\frac{\hbar^2}{2m_e}\nabla^2\psi_e + V_e\psi_e \tag{3.10}$$

$$E\psi_n = -\frac{\hbar^2}{2m_e}\nabla^2\psi_n + U(R)\psi_n, \tag{3.11}$$

where the subscripts e and n indicate the electronic and nuclear wavefunctions, respectively. In the approach presented here, initial calculations employ energy curves available from the literature to estimate the $U(R)$ term in Eqn. 3.11 which represents the rotationless potential energy associated with the electronic wavefunctions for nuclei separated by R. An alternative approach, employed by many physical chemists, would be to perform *ab initio* calculations of the electron wavefunctions.

In any molecular analysis, it is important to include the effects of rotational motion on the potential energy of the molecule. The rotational energy may be calculated by

$$V_J(R) = \frac{hJ(J+1)}{8\pi^2 c\mu R^2}, \tag{3.12}$$

where J is the rotational quantum number and μ is the reduced mass of the molecule. Therefore, the effective potential energy can be written as

$$V_{eff}(R,J) = U(R) + \frac{hJ(J+1)}{8\pi^2 c\mu R^2}. \tag{3.13}$$

It is easy to see how, particularly for large J and/or small μ, Eqn. 3.13 can produce potentials significantly different from those in the rotationless case. This is illustrated by Fig. 3.7 where the $X^2\Sigma^+_{1/2}$ and $B^2\Sigma^+_{1/2}$ potentials of Cs-Ar are plotted for J = 0, 150, and 300.

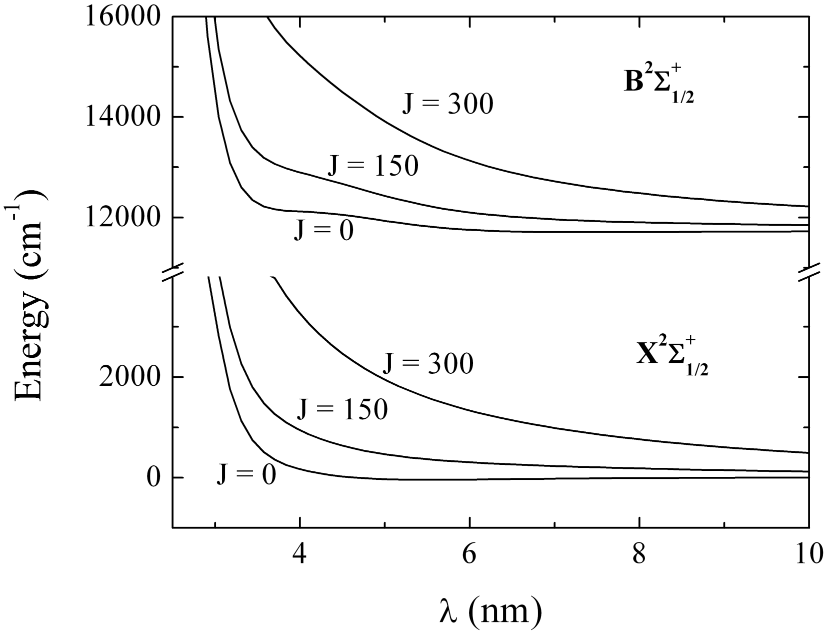

Figure 3.7: Plot of the $X^2\Sigma^+_{1/2}$ and $B^2\Sigma^+_{1/2}$ potentials from [14] for J = 0, 150, and 300 cases.

Upon replacing $U(R)$ with $V_{eff}(R,J)$ from Eqn. 3.13, Eqn. 3.11 can be rewritten as

$$\frac{d^2\psi(R)}{dR} + H[\epsilon''_J - V_{eff}(R,J)]\psi(R) = 0, \tag{3.14}$$

where ϵ''_J is the kinetic energy of the ground state molecule. The subscript J indicates that some fraction of the kinetic energy is associated with rotational motion. For unbound states, ϵ''_J is continuous and may take on any value.

The most straightforward method of calculating the wavefunctions in Eqn. 3.14 is by employing the Numerov-Cooley method [43]. In this calculation, each individual wavefunction corresponds to a particular ϵ''_J and J and is solved as a function of R

by using outward integration from small R. To begin the calculations, the value of ψ for the smallest value of R considered (R_0) is set to 0 and the value of ψ for the next smallest value of R (R_1) is set to an an arbitrarily small number. For all subsequent values of R, $\psi(R)$ is calculated by

$$\psi(R_i) = \frac{2\psi(R_{i-1})(1 - \frac{h^2}{12}V(R_{i-1})) - \psi(R_{i-2})(1 - \frac{h^2}{12}V(R_{i-2})) + h^2 V(R_{i-1})\psi(R_{i-1})}{1 - \frac{h^2}{12}V(R_i)}, \tag{3.15}$$

where the explicit dependences of ψ on ϵ''_J and J and of V on J have been omitted for clarity. It is important that each wavefunction calculated using Eqn. 3.15 is normalized to

$$P = 0.27844 \left(\frac{\mu_A}{\epsilon''_J}\right)^{1/4}, \tag{3.16}$$

where μ_A is the reduced mass in amu [40, 44, 45]. P has units of (cm^{-1} × $\mathring{A}$)$^{1/2}$ and this normalization introduces the density of states to the wavefunctions calculated with Eqn. 3.15 for various values of ϵ''_J and J. Without proper normalization, it is impossible to extract meaningful results from the calculations.

Once the wavefunctions have been calculated for a particular J, Franck-Condon overlap integrals between the upper and lower states for every ϵ''_J (initial) and ϵ'_J (final) eigenenergy combination are tabulated. These integrals have the form

$$\left|< \epsilon'_{J\pm1}|\mu_e(R)|\epsilon''_J >\right|^2 \approx \mu_e \left|< \epsilon'_{J\pm1}|\epsilon''_J >\right|^2, \tag{3.17}$$

where the dipole transition moment $\mu_e(R)$ is assumed to be a constant. The $J \pm 1$ subscript refers to the selection rule that only these transitions are allowed from J, although the approximation that $\Delta J = 0$ can be employed in these simulations [41,42]. It is important to note that the Franck-Condon overlap factors can be nonzero even for transitions that do not conserve kinetic energy. Figure 3.8 presents a logarithmic color map of the Franck-Condon factors as a function of ϵ''_J and ϵ'_J for $J = 0$. Although the largest factors correspond to the red line along which $\epsilon''_J = \epsilon'_J$, there are significant regions to either side of this line in which the factors are nonzero. In particular, Fig. 3.8 indicates that transitions where $\epsilon''_J < \epsilon'_J$ are more favored than those in which $\epsilon''_J > \epsilon'_J$ although there is no obvious explanation for this behavior. The fact that the quantum treatment takes all of these transitions into account is a significant advantage over semiclassical calculations which can only predict those spectral components which exactly match points on the difference potential.

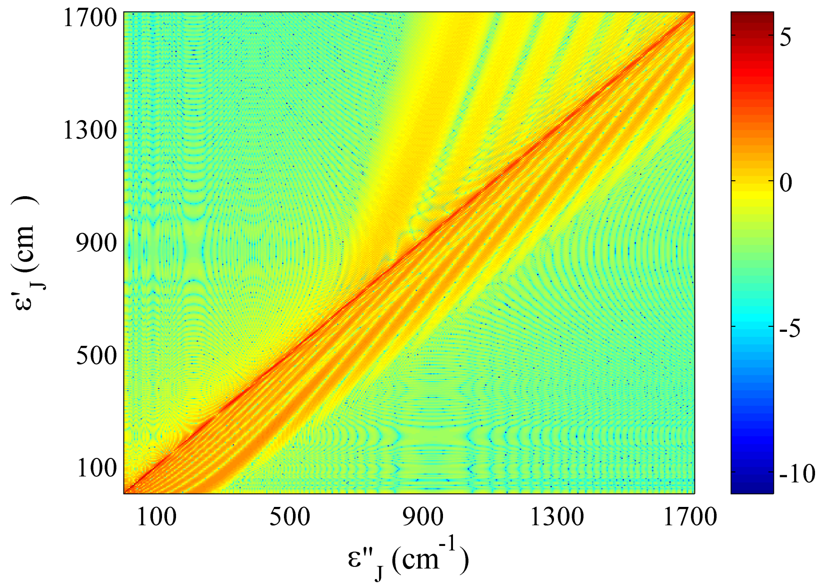

Figure 3.8: Color map for $J = 0$ of the Franck-Condon factors as a function of the initial (ϵ''_J) and final (ϵ'_J) kinetic energy of the molecule. The numbers associated with the bar at right represent the log of the factors.

Upon calculation of the Franck-Condon factors and summing over the corresponding transition energies, it is necessary to determine the J^{th} state's contribution to the overall absorption spectra. This contribution was weighted according to the expression [41, 42]

$$S(\nu) = \int (2J+1)e^{-\epsilon''_J/\mathrm{k_B T}} \left|< \epsilon'_{J\pm1}|\mu_e(R)|\epsilon''_J >\right|^2, \tag{3.18}$$

where the $(2J+1)$ term accounts for the rotational degeneracy and the $e^{-\epsilon''_J/\mathrm{k_B T}}$ term corresponds to the Boltzmann distribution of thermal energies in the ground state [46].

The reduced photoassociation absorption coefficient can be calculated with the expression [41]

$$k_{PA} = \frac{8\pi^3}{3\lambda} q^2 a_0^2 \frac{1}{g_e Q_t} S(\nu)[N_A][N_B], \tag{3.19}$$

where g_e is the electronic degeneracy and Q_t is the translational partition function given by

$$Q_t = \left(\frac{2\pi\mu \mathrm{k_B T}}{h^2} \right)^{3/2}. \tag{3.20}$$

In this work, the simulated spectrum is scaled to match the experimental data, therefore necessitating only the inclusion of the $1/\lambda$ factor in Eqn. 3.19 into the expression for S(ν).

The most straightforward method for modifying an interaction potential is by choosing a functional form with constants that can be adjusted. The ground state of CsAr and a variety of other diatomic molecules were fit very well to a four-parameter model proposed by Cvetko et al. [47] using the expressions

$$\begin{aligned} U(R) &= \frac{C_6}{120}\left(\frac{b}{3}\right)^6 \left(ae^{-bR} - \chi e^{-2bR/3} - e^{-bR/3}\right), \qquad & bR \leq 16.6 \\ U(R) &= \frac{C_6}{120}\left(\frac{b}{3}\right)^6 ae^{-bR} - \frac{C_6}{R^6 - Q^2R^4}, \qquad & bR \geq 16.6 \end{aligned} \tag{3.21}$$

where χ in Eqn. 3.21 is determined by continuity of the two expressions at $bR = 16.6$.

Because accurate calculation of the wavefunctions requires values for the interaction potentials at larger R values than are included in Refs. [29] and [48], the available portions of the $\mathrm{B}^2\Sigma^+_{1/2}$ curves in these papers were fit using Eqns. 3.21.

In order to properly simulate absorption spectra, it is necessary to calculate wavefunctions for a sufficient number of J values and range in ϵ''_J. The maximum value of ϵ''_J is determined by estimating the maximum thermal energy of the system where there is sufficient population to impact the results. For CsAr, this value was estimated to be $5\mathrm{k_B T}$ and the corresponding energy range extended for ϵ''_J extended from 1 cm^{-1} to 1700 cm^{-1}. Energy steps of 4 cm^{-1} were determined to be sufficiently small that they satisfactorily approximated the free particle energy continuum.

Only J values up to 300 were included in the calculations since further increases in J had a negligible impact on the simulated spectra. Similarly, it was determined that only calculations of the wavefunctions corresponding to $J = 0$, 50, 100, 150, 200, 250, and 300 were necessary. For a given rotational level, the lower bound on the value of ϵ''_J had to be sufficiently large that the solution was classically allowed. This was accounted for by adjusting the minimum value of ϵ''_J to twice the minimum rotational value of the computation domain for each value of J.

Values of R in the calculations ranged from 3.5 Å to 37 Å in 0.005 Å steps. Typically, the step size in R, ΔR, should be larger than the minimum step size as defined by [40]

$$\Delta R = 5 \times 10^6 \left(\frac{h}{2\mu c \epsilon''_{J,max}} \right)^{1/2}, \tag{3.22}$$

where $\epsilon''_{J,max}$ is the maximum kinetic energy of the molecule. In order to check the validity of the simulations, it is important to verify that neither changing the bounds on R nor reducing ΔR has a significant effect on the simulation output.

In fitting the potentials, the first step was to perform a sensitivity analysis to determine reasonable step sizes for altering the C_6, Q, b, and a potential constants. A self-optimizing routine was then employed which randomly selected which of the four constants would be incremented (up or down) by its predetermined step size. In order to determine the quality of the resulting $B^2\Sigma^+_{1/2}$ potential, the predicted absorption spectra was corrected for the index of refraction of air (1.00027454 at 900 nm [49]) and the $1/\lambda$ factor prescribed by Eqn. 3.19.

In order to compare the simulated spectra with the experimental results, the relative scaling of the simulated spectra was extremely important. This scaling was performed by finding the constant scaling factor for the simulated spectra which minimized the sum of least squares error (SSQE) with respect to the experimental results. The SSQE for each curve was obtained by squaring the point-by-point difference of the predicted spectra from the experimental data and summing the results. The corresponding value of the SSQE was then used as a measure of the fit quality and whether or not a change in the constant improved the results. Iterations in this process with decreasing step sizes were performed to arrive at the new $B^2\Sigma^+_{1/2}$ potential provided in Fig. 3.9. Table 3.1 shows the final C_6, Q, b, and a constants used in obtaining the best fit alongside the fit constants for other potentials available in the literature.

Table 3.1: Potential fit constants for the $X^2\Sigma^+_{1/2}$ and $B^2\Sigma^+_{1/2}$ states of CsAr.

	$X^2\Sigma^+_{1/2}$	$B^2\Sigma^+_{1/2}$		
Ref.	[47]	[29]	[48]	Present Work
C_6	392	354	1990	491
Q	9.4	5	40	12.9
b	0.83	0.59	0.36	0.46
a	1160	1321	3001	1349

After obtaining best-fit constants for $B^2\Sigma^+_{1/2}$ state, the code was altered to perform a similar optimization of the $X^2\Sigma^+_{1/2}$ state by treating the $B^2\Sigma^+_{1/2}$ state as fixed. The

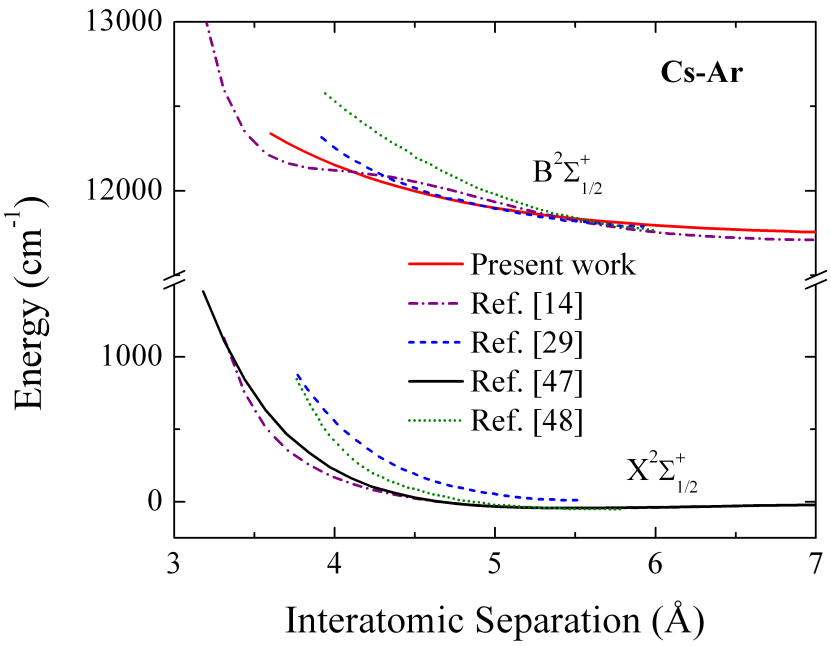

Figure 3.9: New $B^2\Sigma^+_{1/2}$ state potential compared with previous curves available in the literature.

best fit for the $X^2\Sigma^+_{1/2}$ state did not vary significantly (<15 cm^{-1} at any point) from the ground state potentials of [14] and [47] which both agreed quite closely with one another as observed in Fig. 3.9. This led to the use of the $X^2\Sigma^+_{1/2}$ potential suggested by [47], a result that is consistent with the assumption that the ground state is better known experimentally than the $B^2\Sigma^+_{1/2}$ state.

The data in Fig. 3.10 were generated from the values in Table 3.1 and those fit to the other curves of Fig. 3.9. The spectral region 827 nm$\leq\lambda\leq$849 nm was considered and the quality of the fits were evaluated by calculation of the SSQEs. These results are summarized in Table 3.2.

Although experimentally the blue satellite peaks at ∼837 nm, none of the previous potentials accurately reproduced this characteristic. References. [14] and [48] predicted this feature at ∼832 nm and ∼834 nm, respectively, both to the blue of the actual value. The potentials of Ref. [29] predict the blue satellite peaking to the red at ∼846 nm. The best fit provided by the present work peaks at ∼837 nm.

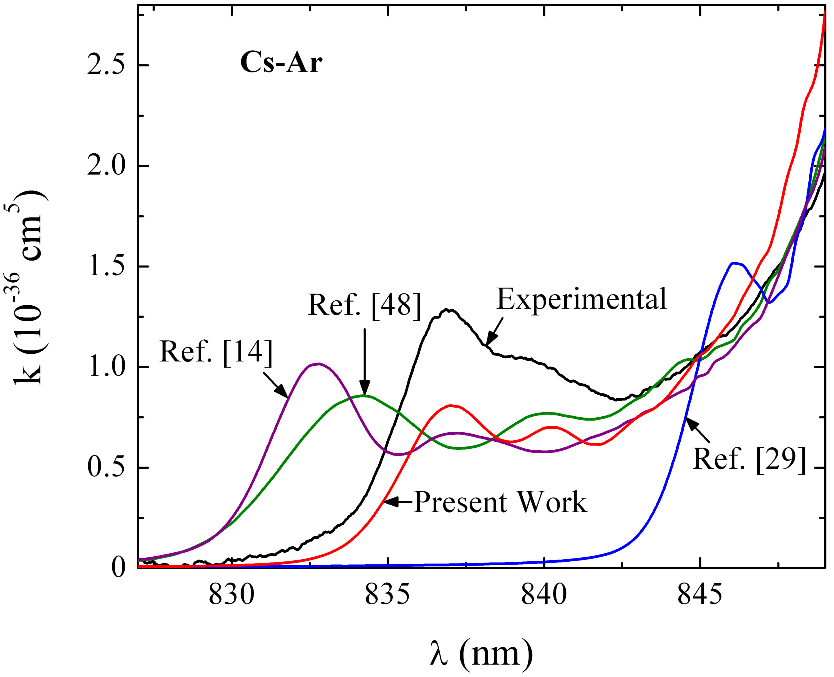

Figure 3.10: Spectral predictions of the best fit obtained in this work compared to the experimental data and the simulations using other potentials available in the literature.

For all of the potentials investigated with the exception of Ref. [29], the undulatory structure on the red side of the blue satellite appears to be overstated. No obvious reason for this behavior exists. In the longer wavelength (>845 nm) region, both Refs. [14] and [48] more closely match the experimental data. However, as indicated by Table 3.2, the SSQE values of these potentials indicate that the overall quality of fits for these potentials are lower than those of the present work by a minimum of ∼44%. This result highlights the fact that fitting only to a small portion of the spectra can severely limit the overall accuracy of a potential.

It is possible that the true $B^2\Sigma^+_{1/2}$ state which would completely reproduce the experimental results requires a more complicated functional form than can be provided by Eqn. 3.21. Nevertheless, these efforts demonstrate the advantages of employing computationally intensive quantum calculations as a means of investigating free→free photoassociation.

Table 3.2: Summary of the SSQE values for the Cs-Ar $X^2\Sigma^+_{1/2}$ and $B^2\Sigma^+_{1/2}$ available in the literature.

Ref.	SSQE	$\text{SSQE}_{\text{Present Work}}/\text{SSQE}$
Present Work	1.54	1.00
[48]	2.21	1.44
[14]	3.26	2.11
[29]	8.71	5.66

CHAPTER 4

ABSORPTION EXPERIMENTS AND THREE-BODY PHOTOASSOCIATION

For many of the gas mixtures employed in these experiments, detailed absorption spectra were not available in the literature. One notable exception to this was in the case of Cs-Ar [29,39]. In particular, the comprehensive absorption spectra in Ref. [39] served as a benchmark for corroborating the results obtained here.

At the outset of the experiments described here, binary contributions to spectra were assumed to be dominant. However, results from ternary and quaternary gas mixtures demonstrate a significant dependence on three-body interactions. As will be discussed in greater detail, this unexpected behavior has both practical and physical implications.

4.1 Experimental Setup

The experimental setup employed in the absorption experiments is illustrated in Fig. 4.1. The broadband light source is a microscope light box modified in several ways to improve its performance. These enhancements include an external dc power supply in place of the internal circuitry to stabilize lamp output and a gold coating of the bulb reflector housing which increases IR reflectance. A computer controlled, 0.67 m scanning monochromator with a first order reciprocal dispersion of 12 Å/mm and entrance/exit slit widths of 8 μm with a photomultiplier tube (PMT) detector is employed to provide approximately 1 Å resolution.

All of the data presented here are expressed in terms of the reduced absorption

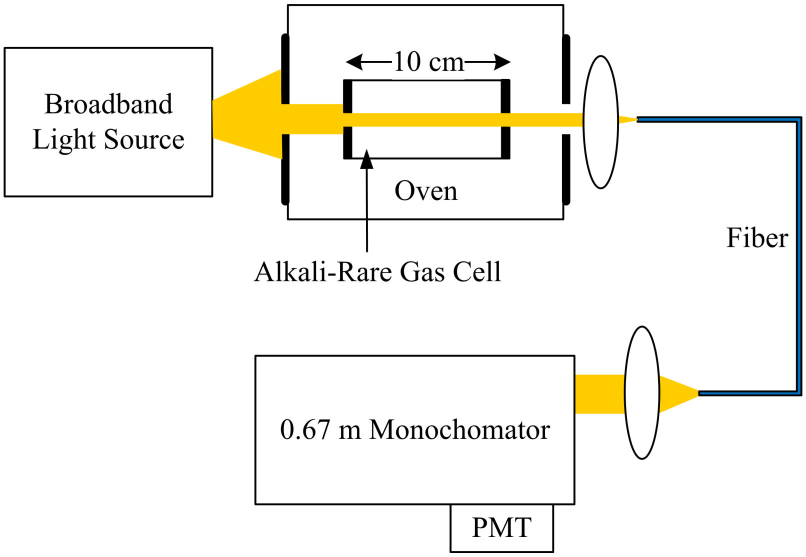

Figure 4.1: Experimental setup employed in the absorption experiments.

coefficient k (cm^{-5}) obtained with Eqn. 3.3. The primary reason for this reduction is that, at the temperatures and partial pressures of interest, k(λ) remains constant. This behavior is illustrated for wide ranges of [Cs] and [Ar] in Ref. [39].

This result has important implications regarding the photoassociation kinetics of satellites because it indicates that satellites arise predominantly from two-body interactions. This is a key assumption on which all of the previous work on satellites is based. Although this explanation is useful and intuitively satisfying, the actual situation is more complicated, as will be discussed in the next section.

It should be noted here that initial absorption experiments did not observe the expected overlap of reduced absorption coefficients as was expected. Intensive efforts to explain this discrepancy resulted in attributing the difference to waveguiding along the edges of the cell which increased the effective path length of the light through the cell. This issue was mitigated by adding black foil end caps with holes punched into them on either end of the cell as shown in Fig. 4.2. Every absorption spectrum presented here was verified by the observation of reduced absorption curves at multiple temperatures. The data presented here corresponds to the highest cell temperatures investigated as the increased absorption provided superior signal-to-noise ratios. Without this correction to the experiment, much of the relevant kinetics (particularly with regard to three-body photoassociation) would have been significantly obscured.

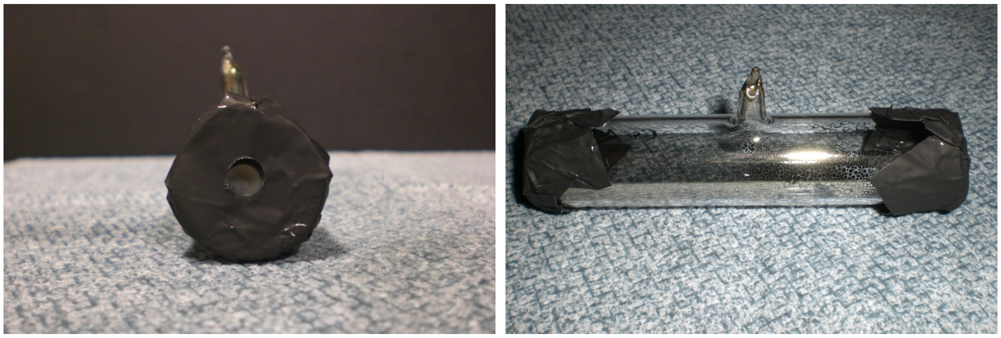

Figure 4.2: (Left) End-on and (right) side-on images of a 10 cm long gas cell with black foil end caps introduced to mitigate uncollimated light from contributing to the output signal.

The most significant of the experimental uncertainties was the temperature. A proportional-integral-derivative (PID) temperature controller was used to minimize cell temperature fluctuations and, accounting for the calibration of the thermocouples, there was an estimated ±2 K temperature uncertainty. This corresponds to approximately 10% uncertainty in alkali number density with number densities calculated using the expressions in [50] and [51]. Another source of error was PMT nonlinearity, which was evaluated by inserting neutral density filters into the optical path and was estimated to be ∼2-3%. Absorption scans performed near room temperature ([Cs]$\sim 5 \times 10^{10}$cm^{-3}) showed very little absorption and provided a means of quantifying wavelength-dependent instrumental sensitivy as well as a cell-specific wavelength calibration by means of the D_2 line. Noise, some of it structured, was present in the scans regardless of temperature and was attributed to external vibrations that varied daily and could not be completely eliminated. A primary means of mitigating this noise was achieved by averaging two scans at each temperature to obtain the data presented here.

The repeatability of the experimental data and its agreement with a Cs-Ar absorption spectrum from Ref. [39] is illustrated in Fig. 4.3. The curves overlap well within experimental error with the exception of the region 841$\leq \lambda \leq$844 nm where discrepancies as high as 25% are observed. This discrepancy is most significant at ~842.5 nm although no satisfactory explanation for this observation is available. The best agreement between the previously reported results and the present work is at 475 K and was attributed to the higher signal-to-noise ratio corresponding to increased absorption.

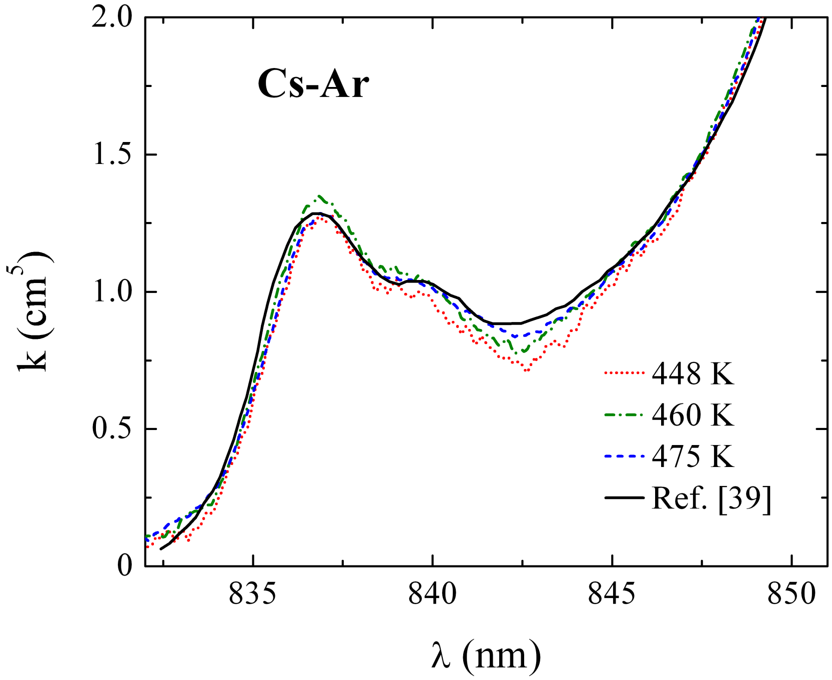

Figure 4.3: Comparison of k in Cs-Ar from [39] with that obtained in this work for gas cell temperatures of 448 K, 460 K, and 475 K, corresponding to [Cs] $= 6.6\times10^{14}$ cm^{-3}, 1.1×10^{15} cm^{-3}, and 1.9×10^{15} cm^{-3}, respectively.

4.2 Three-Body Photoassociation

4.2.1 Ternary Cs-Rare Gas Mixtures

As discussed in Section 3.1, different collision pair combinations produce unique spectral satellites. At the outset of this work, it was expected that, since most signs pointed to binary contributions to the satellite spectra as dominant, mixing of multiple perturbing species would result in a satellite consisting of the simple superposition of two composite satellites. For example, a ternary mixture containing Cs-Ar-Kr would normally be expected to have a satellite consisting of the linear superposition of Cs-Ar and Cs-Kr weighted by the relative densities of Ar and Kr perturbers. This would allow for the realization of a certain degree of spectral engineering.

Experimentally, this simple superposition was not observed in any of the ternary or quarternary gas mixtures investigated. For Cs-Ar-Kr, the results are presented in Fig. 4.4. In this data, each mixture has the same total rare gas perturber density, with the Cs-Ar mixture (blue), the Cs-Kr mixture (red), and the Cs-Ar-Kr mixture having [Ar] = [Kr] (black). The upper graph of Fig. 4.4 shows the reduced absorption coefficient for each of the three mixtures. While the Cs-Ar and Cs-Kr have peaks near 837 nm and 841 nm, respectively, the Cs-Ar-Kr lineshape is most similar to that of Cs-Ar.

The lower portion of Fig. 4.4 includes three traces: the experimental data from the Cs-Ar-Kr mixture (black), the expected results from binary superposition of the Cs-Ar and Cs-Kr satellites (red), and the best fit combination of superposition the Cs-Ar and Cs-Kr (blue). The fact that the fit can be made to closely match the experimental data suggests that binary interactions still play an important role. However, this fit relies on scaling of the individual contributions which, in turn, suggests the Cs-Ar lineshape is enhanced by a factor of $\sim$2.1 over the expected value and the Cs-Kr is suppressed by a factor of $\sim$0.4. These characteristics of Fig. 4.4 show that heterogeneous three-

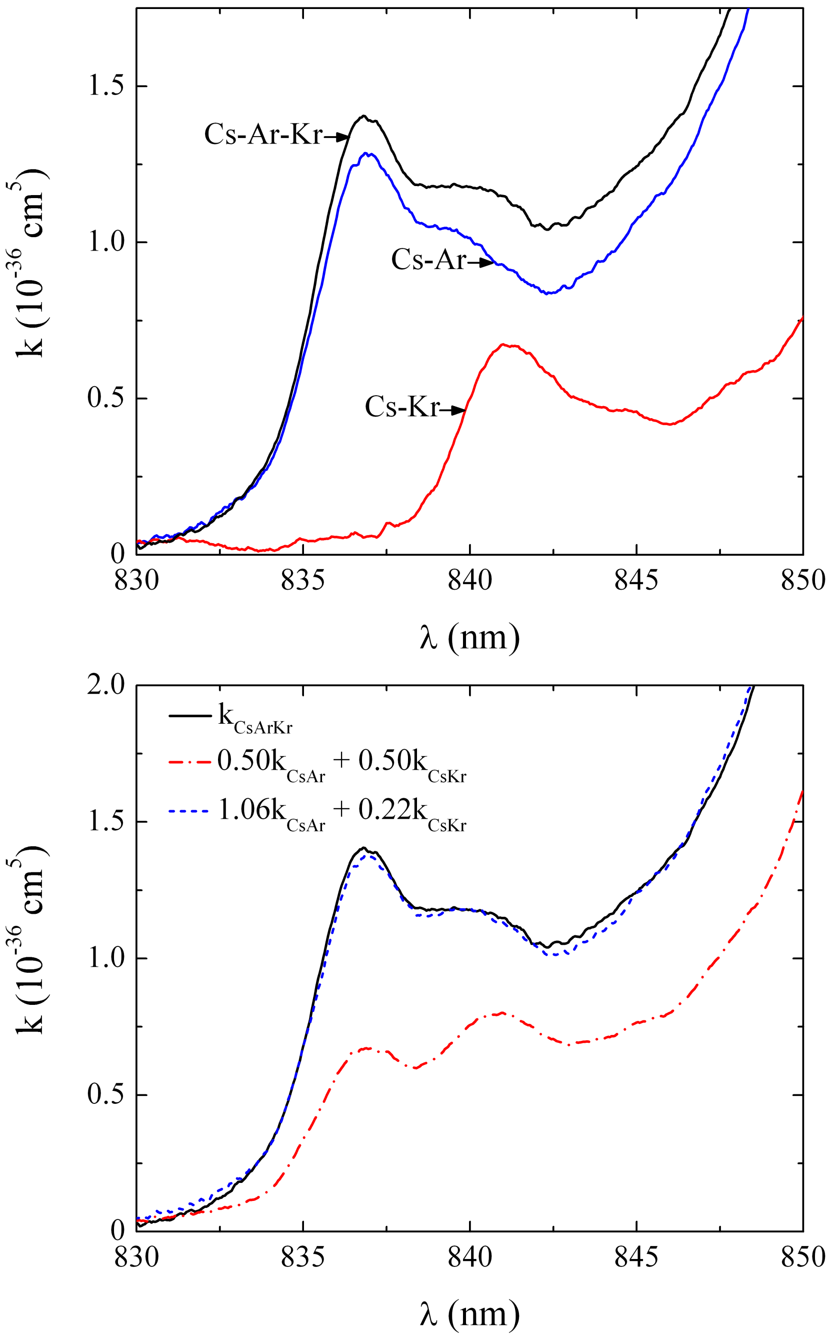

Figure 4.4: Comparison of the reduced absorption coefficient for Cs-Ar, Cs-Kr, and Cs-Ar-Kr mixtures.

body interactions are being observed, although there is no satisfactory explanation for the mechanism behind these results.

In an attempt to study this behavior, similar experiments were carried out with other rare gas combinations. The upper graph of Fig. 4.5 shows the results from a Cs-Ar mixture (blue), a Cs-Xe mixture (red), and a Cs-Ar-Xe mixture for which [Ar] = [Xe] (black). The Cs-Xe blue satellite peaks near 843 nm, further to the red than either the Cs-Ar or Cs-Kr features.

As in the case of Fig. 4.4, the lower portion of Fig. 4.5 plots the experimental Cs-Ar-Xe absorption (black), the predicted absorption of a 50/50 mixture (red), and the best fit superposition of Cs-Ar and Cs-Xe (blue). The superposition fit indicates that there is a factor of $\sim$4.5 enhancement in the Cs-Ar contribution, over twice the enhancement observed in Cs-Ar-Kr. The Cs-Xe contribution is suppressed by a factor of $\sim$0.6, approximately 20% less than the suppression of Cs-Kr.

The third possible combination of Ar, Kr, and Xe is Cs-Kr-Xe. The upper graph of Fig. 4.6 shows absorption traces for Cs-Kr (blue), Cs-Xe (red), and Cs-Kr-Xe where [Kr] = [Xe] (black).

From Figs. 4.4 and 4.5, one might expect that the lighter and less polarizable of the rare gas species present would dominate the spectra and experience the greatest enhancement. As indicated by the lower graph of Fig. 4.6, the opposite is observed and the Cs-Xe satellite is enhanced by a factor of approximately 14% while the Cs-Kr is once again supressed, in this situation by $\sim$40%.

4.2.2 Ternary and Quaternary Cs-Rare Gas-C_2H_6 Mixtures

Further experiments demonstrated that these observations are not limited to alkali-rare gas combinations. Because several of the oscillator experiments relied on C_2H_6 as a collisional relaxant, it made an excellent candidate for study of what differences

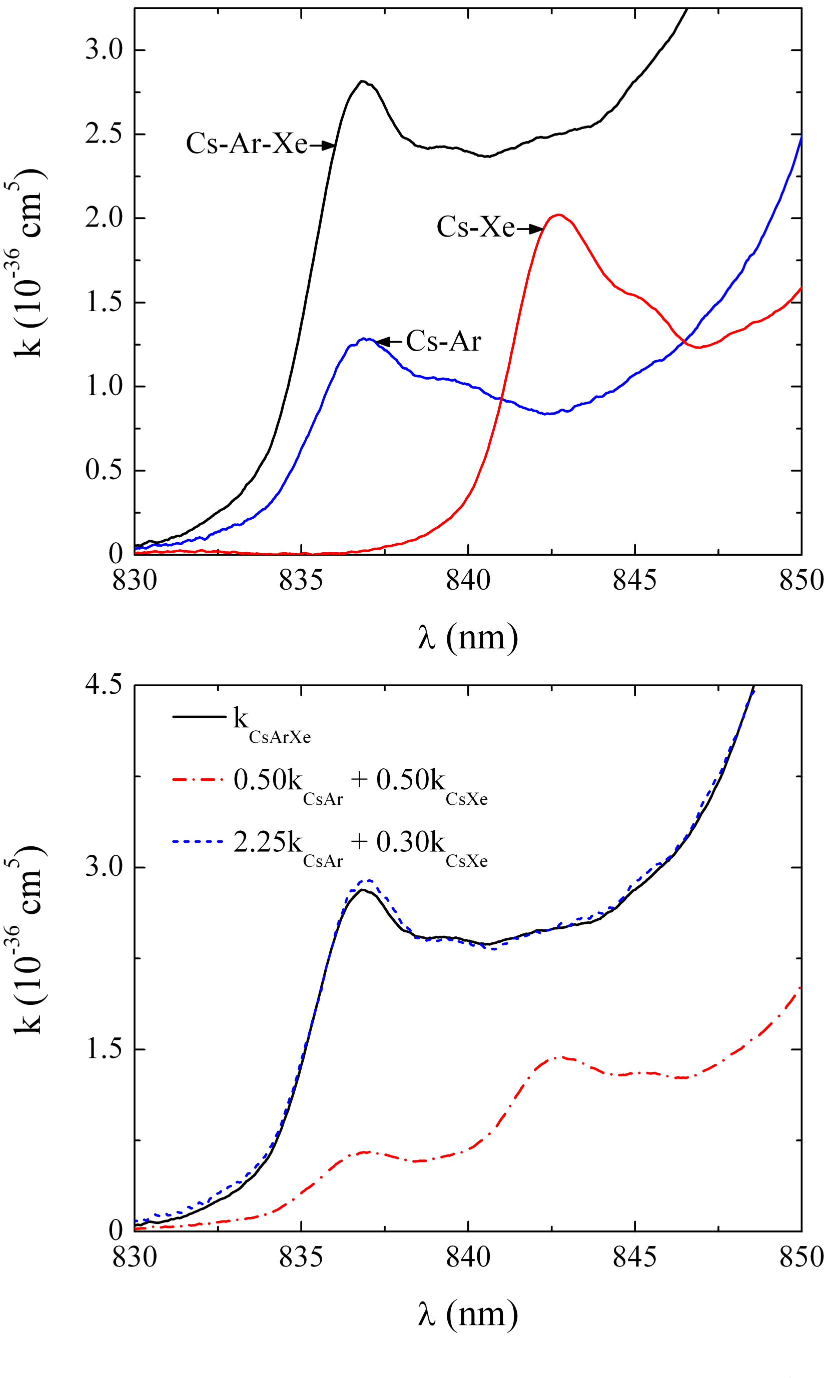

Figure 4.5: Comparison of the reduced absorption coefficient for Cs-Ar, Cs-Xe, and Cs-Ar-Xe mixtures.

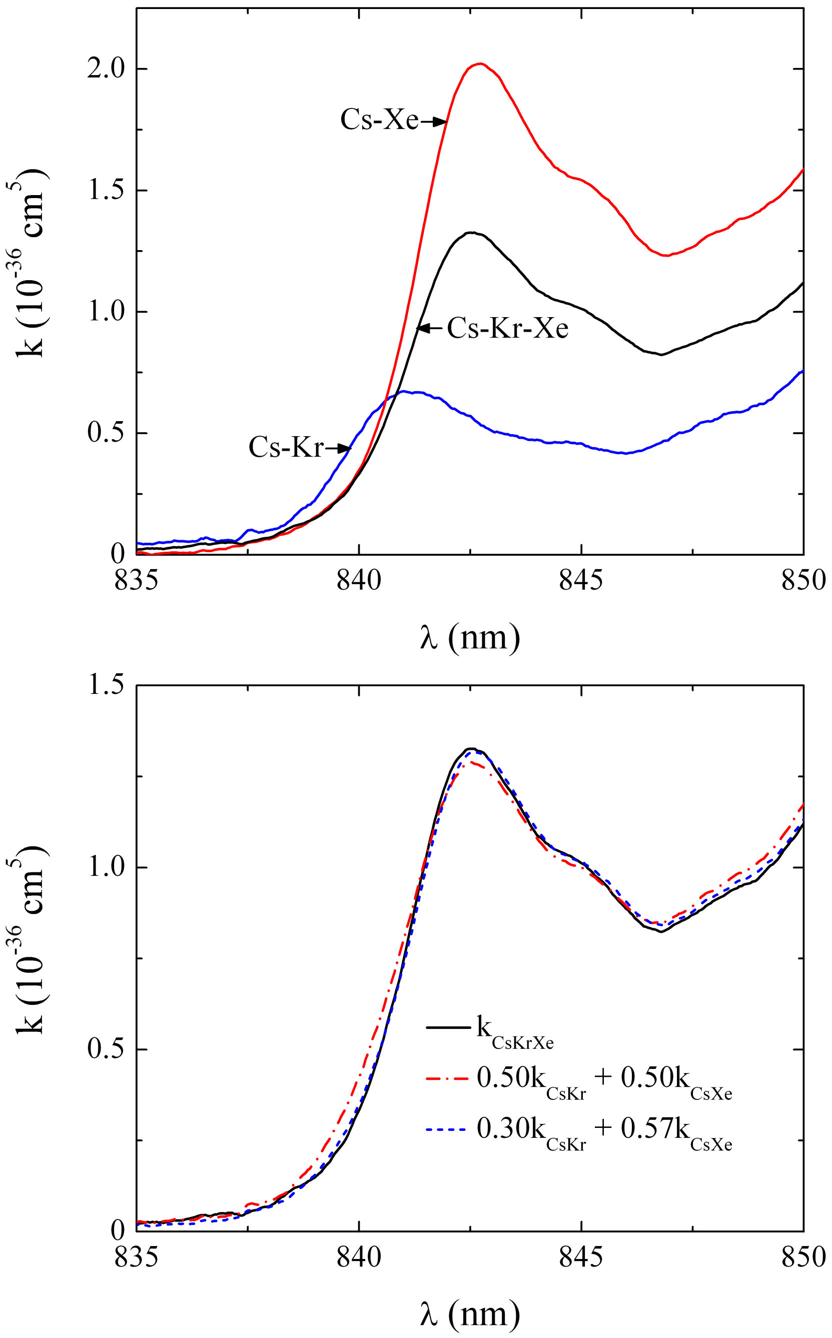

Figure 4.6: Comparison of the reduced absorption coefficient for Cs-Kr, Cs-Xe, and Cs-Kr-Xe mixtures.

may exist when using a molecular perturber as opposed to a rare gas atom.

Figure 4.7 compares the reduced absorption of a Cs-Ar (blue) mixture, a Cs-C_2H_6 (red) mixture, and a Cs-Ar-C_2H_6 (black) mixture where $[Ar] = 5[C_2H_6]$. As observed in the upper portion of Fig. 4.7, the D_2 blue satellite peaks near 835 nm in the Cs-C_2H_6 mixture. In addition, the Cs-C_2H_6 satellite extends significantly further to the blue than does the Cs-Ar satellite (or Cs-Kr/Cs-Xe).

As in the alkali-rare gas combinations, the lower graph of Fig. 4.7 compares the Cs-Ar-C_2H_6 experimental data (black) with the expected lineshape from binary superposition (red) and the best fit of the scaled lineshapes (blue). According to the best-fit scaling factors, the Cs-Ar contribution experiences an enhancement factor of $\sim$1.3 while the Cs-C_2H_6 factor is suppressed by a factor of $\sim$0.4. The results are similar to those of Cs-Ar-Kr and Cs-Ar-Xe in that Cs-Ar is observed to be the species which experiences an enhancement while the other contribution is suppressed.

In addition to the ternary gas mixtures, a quaternary gas mixture of Cs-Ar-Kr-C_2H_6 was tested. The upper graph of Fig. 4.8 compares the absorption traces of Cs-Ar-Kr (where $[Ar] = [Kr]$), Cs-C_2H_6, and Cs-Ar-Kr-C_2H_6 (where $[Ar] = [Kr] = 2.5[C_2H_6]$). The lower graph of Fig. 4.8 compares the experimental Cs-Ar-Kr-C_2H_6 data (black) with the predicted superposition (red) and the scaled best-fit superposition (blue). The Cs-Ar-Kr contribution, itself dominated by the Cs-Ar lineshape, experiences an enhancement factor of approximately 2.5, a dramatic increase for a relatively low (100 Torr) partial pressure of C_2H_6. The best-fit constants for this data are unique in two ways. First, the fit appears to have an extended region of relatively poor lineshape fit from approximately 838 nm to 843 nm. Qualitatively, it appears that there is no way for the composite contributions to provide the more pronounced second peak centered near 840 nm. Also, this is the first observation of a fit constant having a negative value. It is possible this factor is sufficiently small that its negative value corresponds to noise, although this does not explain why the Cs-C_2H_6 contribution

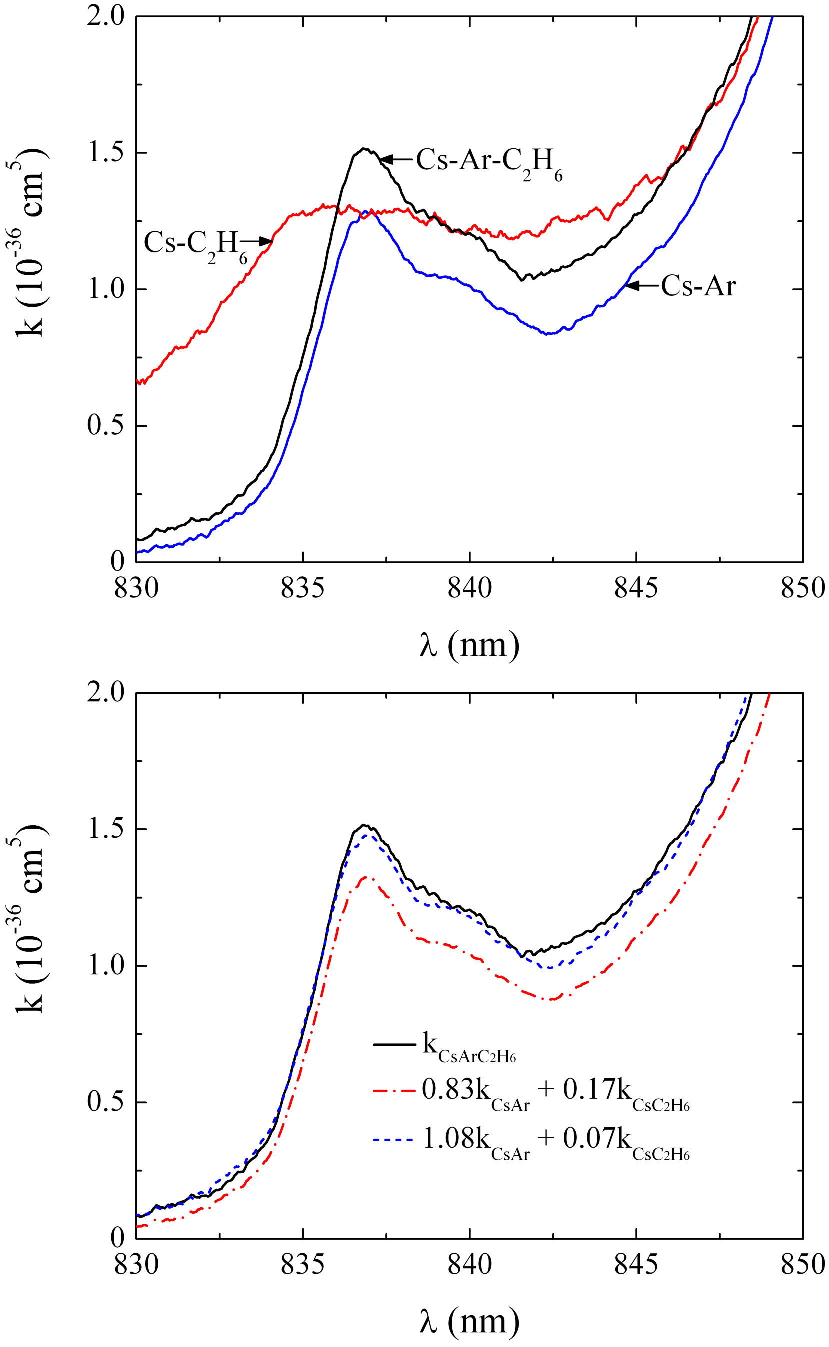

Figure 4.7: Comparison of the reduced absorption coefficient for Cs-Ar, Cs-C$_2$H$_6$, and Cs-Ar-C$_2$H$_6$ mixtures.

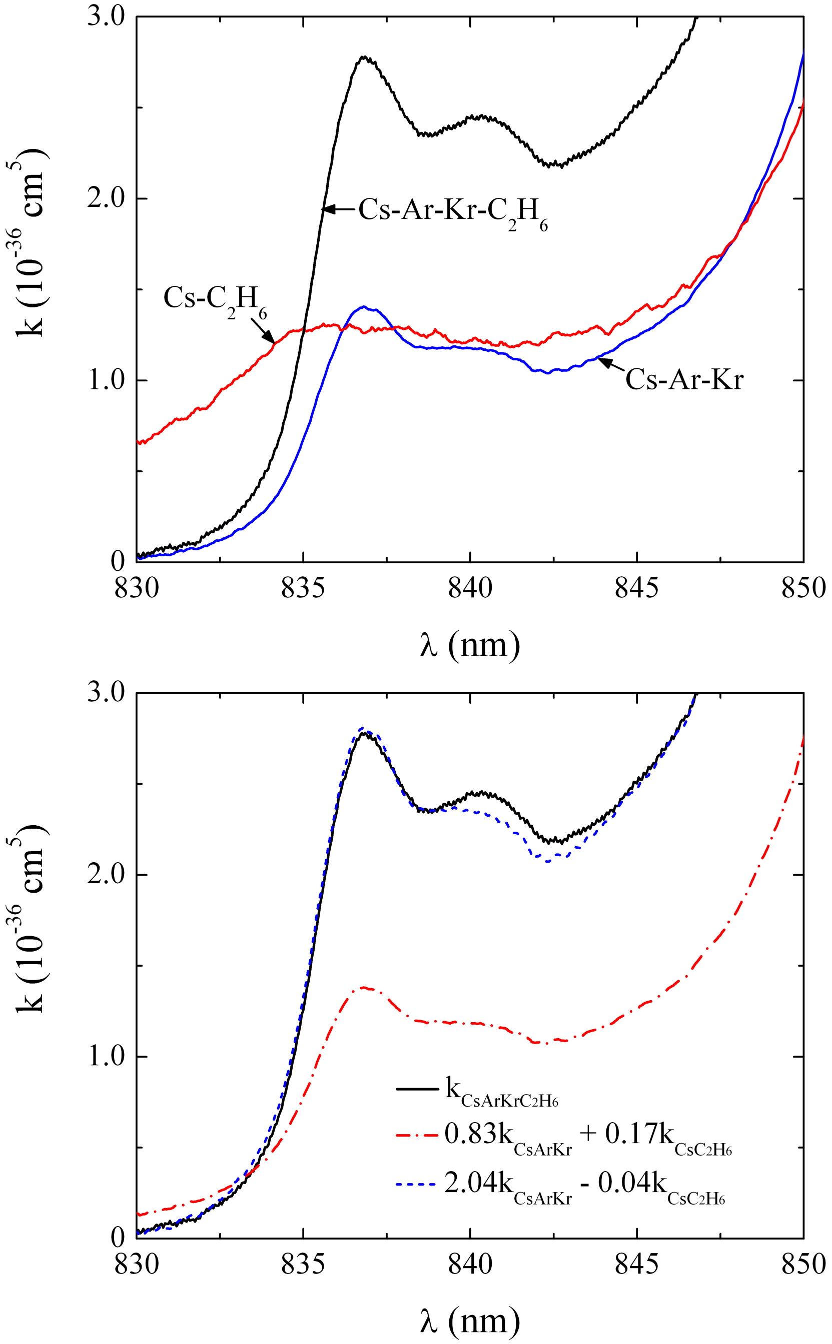

Figure 4.8: Comparison of the reduced absorption coefficient for Cs-Ar-Kr, Cs-C_2H_6, and Cs-Ar-KrC_2H_6 mixtures.

is, therefore, completely absent in the experimental spectra.

4.2.3 Possible Explanations

From the data presented in Figs. 4.4–4.8, there is no clear trend with respect to the variation in perturber characteristics such as mass, polarizability, or molecular shape. Two possible explanations for these observations are described here, although further experimentation is necessary before a complete theory can be developed and rigorously tested.

The first proposed explanation of this behavior is that, in three-or-more species mixtures, the distribution of pairs is different from that of a binary mixture. Figure 4.9 shows the pair distribution of the first and second nearest perturbers for a perturber density of 1.6×10^{19} cm^{-3} in the interactionless case [52].

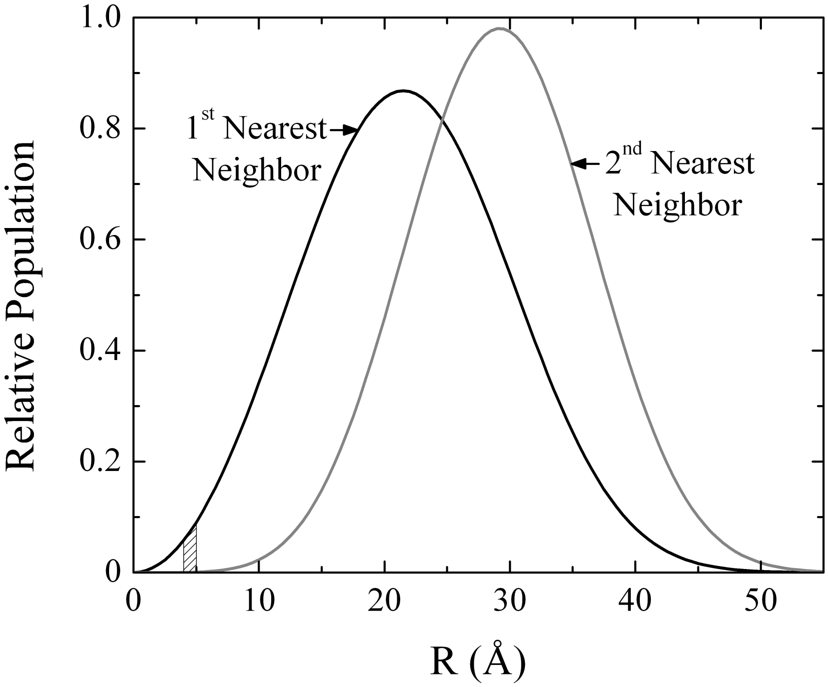

Figure 4.9: Plot of the relative distributions for the first and second nearest neighbor distribution as seen by a Cs atom for any identity of buffer gas with [Rg] $= 1.6 \times 10^{19}$ cm^{-3} [52]. The shaded region corresponds to 4.5±0.5 Å.

In the case of Cs-Ar, the blue satellite corresponds approximately to the region of 4.5±0.5 Å. According to Fig. 4.9, approximately 0.6% of the total Ar atoms are within the annulus 4.5±0.5 Å of a Cs atom. The percentage of Cs atoms with a second perturber within 10 Å is <0.2%. Between this small fractional population, the fact that the $X^2\Sigma^+_{1/2}$ state potential is nearly flat for $R \geq 10$ Å, and the fact that the total lineshape appears to be the result of a scaled superposition of the binary mixture lineshapes, it seems unlikely that the observed three-body enhancement/suppression can be attributed to triatomic molecules.

What may be occurring is related to the fact that Fig. 4.9 does not include the R dependence of the interaction potentials. The 4.5±0.5 Å region is within several Å of where the Cs-Ar potentials become significantly repulsive. It is possible that, by introducing a third species with a unique repulsive nature at small R, that first nearest neighbor distribution in Fig. 4.9 could be altered or shifted to small R, slightly altered such that the percentage of population in the 4.5±0.5 Å region would increase. For example, simply shifting the distribution by 1 Å could increase the fractional population to ∼1.1%, approximately a factor of two larger. Similarly, the distribution could be altered such that there are fewer pairs in the region of interest. These two effects could occur simultaneously with certain perturber combinations, explaining the enhancement and suppression observed in all of the ternary and quarternary mixture experiments.

An alternative explanation of three-body photoassociation involves a change in the transition dipoles of the pairs rather than a change in the pair distribution. Referring again to Fig. 4.9, a pair having a separation of 4.5±0.5 Å would have a significant probability of having a third atom a distance of 10 to 20 Å away. Although this distance may be too great for the third species to perturb the energy levels of the pair (thus maintaining the binary lineshape), it could influence the relative dipole alignment of the pair. Depending on the nature of the alignment, this could effectively change the $B^2\Sigma^+_{1/2} \rightarrow X^2\Sigma^+_{1/2}$ cross section and lead to the results in Figs. 4.4–4.8.

Validating either of these theories or developing the groundwork for others will require comprehensive experimental data and computational efforts. However, regardless of the nature of these unexpected observations, a better understanding of three-body photoassociation is exciting for a number of reasons. From the perspective of high power laser design, three-body photoassociation provides yet another means by which careful selection of the identity and partial pressure of perturbers can be used to manipulate the spectral position, breadth, and absorption coefficient of the satellites of an atomic pair. From a physical perspective, this phenomenon has never been reported in the literature and indicates that previous interpretations of satellites was incomplete. Further investigations of satellite dependence on gas mixture heterogeneity will provide new insight into photoassociation kinetics. This understanding may prove valuable in a much broader range of applications, such as detection schemes based on free→free transitions or directing energy transfer on the atomic scale in chemical reactions.

CHAPTER 5

OSCILLATOR EXPERIMENTS

5.1 Experimental Setup

To date, the majority of XPAL experiments have focused on utilizing Cs as the lasing species. This is due primarily to its high vapor pressure compared with other alkali species and the large amount of spectroscopic data available in the literature [29], [39]. Although it is envisioned that future XPALs will take advantage of diode pumping to produce efficient and compact systems, the experiments described here employ a pulsed dye laser in order to provide high peak intensities and spectral tunability. The experimental setup is illustrated in Fig. 5.1.

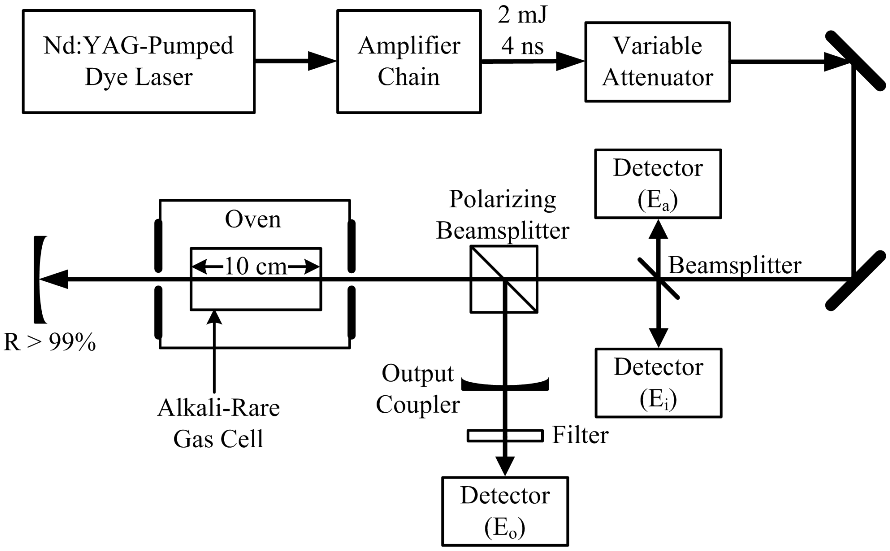

Figure 5.1: Experimental arrangement for the oscillator experiments.

The dye laser is pumped by the second harmonic of an Nd:YAG laser (532 nm) operating at 10 Hz. Two external, homemade dye amplifiers [53] are used to achieve pulse energies on the order of 1–2 mJ with durations of approximately 4 ns. In all of the Cs oscillator experiments, a dye mixture of LDS 821 and LDS 867 is employed to provide spectral tuning over the range of ∼819–856 nm. The nominal spectral width of the dye laser at these wavelengths is approximately 0.2 cm^{-1} or 7 GHz. Although the geometry of the pump beam is complex, it can be approximated by an ellipse with major and minor axis lengths of 7 and 5 mm, respectively.

The gas cells are made of quartz or Pyrex, and are 10 cm long with 2.5 cm diameter windows that are mounted onto the cell so as to be plane parallel or have an 11° angle. Originally, plane parallel windows were thought to be sufficient but were phased out due to issues with parasitic lasing between them. The primary reason for parasitic lasing is the extremely high gain of the atomic alkali lasers, reported to be 0.9 cm^{-1} for a Rb master oscillator power amplifier [54].

Prior to entering the laser cavity, a beamsplitter is used to sample the pump beam to determine the incident pulse energy (E_i). All energy measurements are performed with carefully calibrated pyroelectric detectors. The pump beam then enters the cavity through a polarizing beamsplitter, passes through the gas cell, and encounters the high reflector. This causes the remaining pump light to retrace its initial path through the gain medium after which it exits the cavity and is sampled a second time as indicated in Fig. 5.1. This measurement of unabsorbed pump energy may be used to calculate the pump energy absorbed (E_a) by subtracting it from E_i and accounting for non-alkali sources of pump loss through similar measurements for a cold cell (∼300 K). Considering E_a in addition to E_i provides valuable insight into laser operation and potential scaling opportunities.

The L-shaped laser cavity is approximately 80 cm in length with the highly reflective mirror on one end and a ∼50% output coupler on the other unless otherwise specified. Both mirrors have a radius of curvature of 3 m. A bandpass filter prevents scattered pump photons from contributing to the measurement of E_o.

5.2 Five-Level Laser Operation on the $n^2P_{1/2} \rightarrow n^2S_{1/2}$ Transition

Initial oscillator experiments focused on observation of five-level operation of the XPAL pumping scheme as illustrated in Fig. 5.2. In order to operate in this manner, C_2H_6 was employed as a collisional relaxant to facilitate $6^2P_{3/2} \rightarrow 6^2P_{1/2}$ population transfer. Because of the successful demonstration of three-level alkali lasers which also incorporated doublet relaxation [6], [7] and the equal degeneracy (g = 2) of the upper and lower laser levels, this configuration was deemed to be the most straightforward with which to reach inversion.

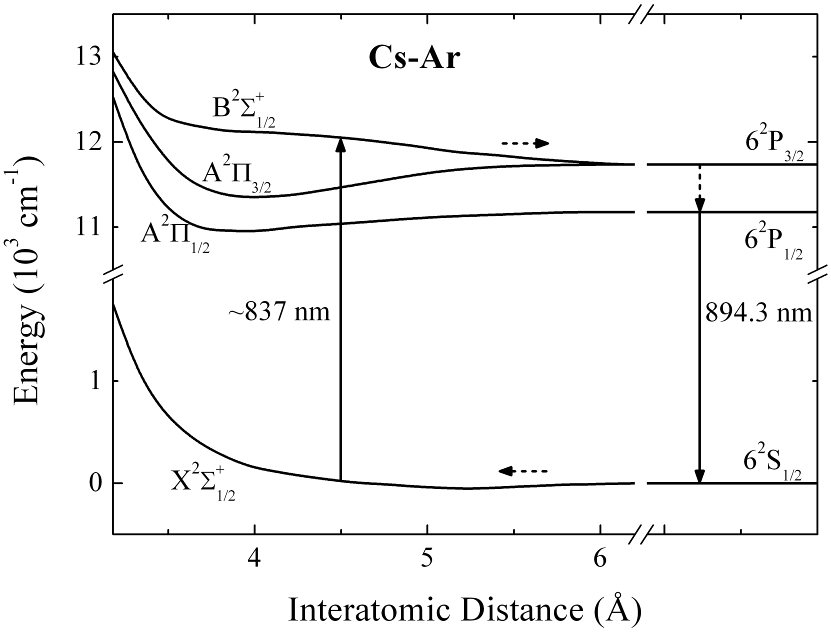

Figure 5.2: Representative five-level Cs XPAL operation in a Cs-Ar-C_2H_6 gas mixture.

5.2.1 Cs-Ar-C_2H_6 Laser Operation at 894 nm

The first experimental demonstration of laser action at 894 nm via excimer photoexcitation was in a mixture of Cs vapor, [Ar] $= 1.6 \times 10^{19}$ cm^{-3}, and [C_2H_6] $= 3.2 \times 10^{18}$ [55, 56]. As in all subsequent laser demonstrations described in this thesis, the following set of characteristics were checked to ensure that laser action was, in fact, occurring.

1. Pulse output temporally distinct from the laser pump pulse.
2. Sensitivity to cavity mirror(s) alignment.
3. Observation of threshold.

Characteristic 1 is illustrated in Fig. 5.3 where the temporal behavior of the pump (black) and output (gray) laser pulses are scaled to simplify comparison. In this experiment, a fast silicon avalanche photodiode with 250 ps rise time and peak spectral response at ∼850 nm together with a 1 GHz bandwidth, externally triggered oscilloscope were employed to provide 1 ns temporal resolution. Each trace in Fig. 5.3 has been normalized to unity for convenience and consists of the average of 30 pulses at a cell temperature of 423 K (corresponding to [Cs] $= 2.2 \times 10^{14}$). Any time delays caused by cable lengths and coupling are accounted for by utilizing the same detector and cables for both sets of pulse measurements.

From the data in Fig. 5.3, it is possible to estimate the minimum gain of the system. The fractional increase in intensity corresponding to prorogation along a distance l with a small signal gain γ_0 may be expressed as

$$\frac{I_{out}}{I_{in}} = e^{\gamma_0 l}. \tag{5.1}$$

The minimum value of $\gamma_0 l$ required for experimental observation of the laser is approximately 30. The data of Fig. 5.3 suggests that the output laser pulse traverses

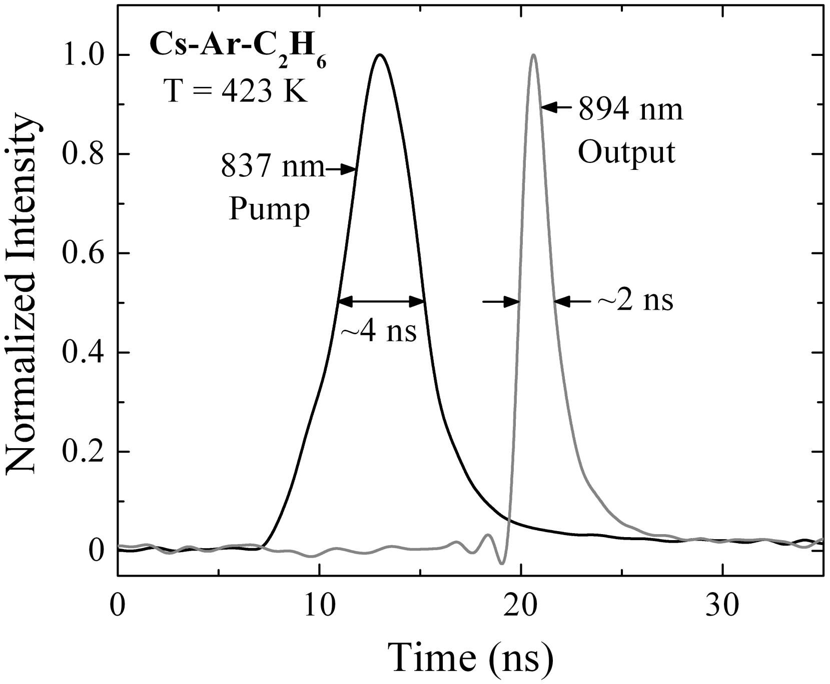

Figure 5.3: Normalized temporal waveforms of the pump (black) and output (gray) laser pulses in a Cs-Ar-C_2H_6 mix where [Cs] = 2.2×10^{14} cm^{-3} (T = 423 K).

the gain medium only twice, corresponding to $l = 20$ cm. This indicates that γ_0 has a minimum value of 1.5 cm^{-1} which is in qualitative agreement with the reported Rb gain of 0.9 cm^{-1} [54].

In addition to indicating laser action on the $6^2P_{1/2} \rightarrow 6^2S_{1/2}$ transition, Fig. 5.3 provides valuable insight into the kinetics of this laser system. First and foremost, the temporally narrow output laser pulse with a zero-to-peak rise time of ∼1 ns highlights the high gain of an atomic alkali laser. Similarly, the ∼8 ns between the pulse peaks corresponds closely to the time it takes the light to travel along the cavity and to the output measurement point. This behavior, coupled with observations of a small dependence of threshold intensity on the output coupler, indicates that the laser is likely operating in a superradiant mode. As will be detailed further, this is also observed with direct atomic excitation and is attributed to the high peak intensity of the dye laser – it is believed that this behavior will not be observed in future CW and quasi-CW systems.

As a complement to the absorption spectra, excitation spectra were obtained by measuring the alkali laser output while scanning the dye laser wavelength. Figure 5.4 shows the excitation spectra obtained for laser action at 894 nm in a gas mixture of Cs, $[\mathrm{Ar}] = 1.6 \times 10^{19}$ cm^{-3}, and $[C_2H_6] = 3.2 \times 10^{18}$ cm^{-3} for gas cell temperatures of T = 410 K (red), 434 K (green), and 450 K (blue) (corresponding to $[\mathrm{Cs}] = 1.2 \times 10^{14}$ cm^{-3}, 3.6×10^{14} cm^{-3}, and 7.2×10^{14} cm^{-3}, respectively). In order to reduce the influence of pump energy variation as the dye laser was scanned, each point in Fig. 5.4 corresponds to a single pulse measurement in which the output energy was divided by the incident energy. An absorption trace (black triangles) at T = 471 K ($[\mathrm{Cs}] = 1.7 \times 10^{15}$ cm^{-3}) is included in Fig. 5.4 for comparison. Note that the absorption data in the 851.5 – 853 nm spectral region has been omitted for clarity.

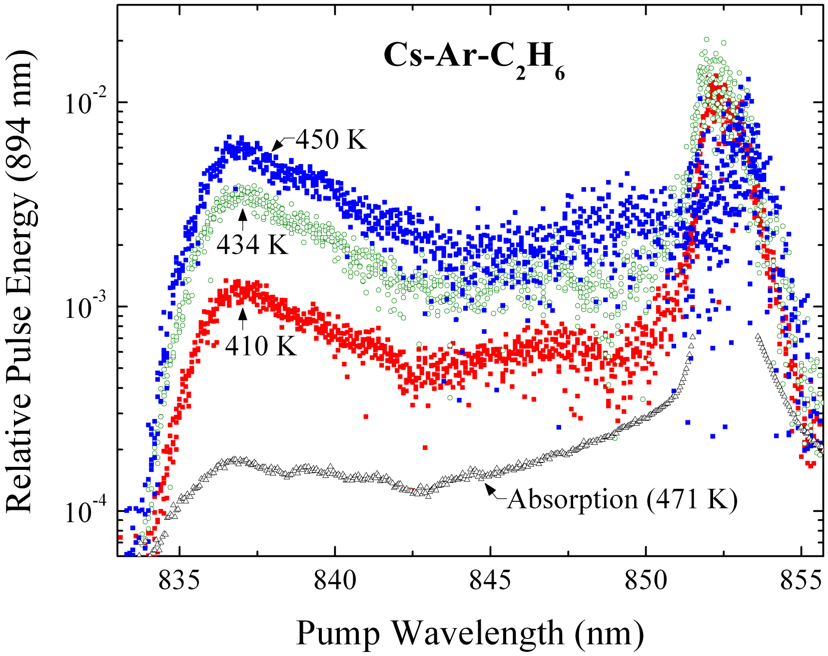

Figure 5.4: Excitation spectra for Cs-Ar-C_2H_6 taken at gas cell temperatures of 410 K, 434 K, and 450 K (corresponding to $[\mathrm{Cs}] = 1.2 \times 10^{14}$ cm^{-3}, 3.6×10^{14} cm^{-3}, and 7.2×10^{14} cm^{-3}, respectively). An absorption trace for 471 K ($[\mathrm{Cs}] = 1.7 \times 10^{15}$ cm^{-3}) is included for comparison. Note that the ordinate is logarithmic.

Figure 5.4 illustrates several important characteristics of laser operation. First, at these temperatures, the blue satellite retains essentially all of the characteristics of the absorption spectrum. These include a steep rise from ~834 to ~836 nm, a peak at approximately 838 nm, and a plateau which only changes gradually from ~842.5 nm to ~850 nm. It should be noted that the data variance in this plateau region is greater than other regions with the exception of the region near the D_2 resonance at 450 K. At present, this observation remains unexplained. At 450 K, a FWHM $\gtrsim$5 nm is observed which is more than twice as large as the bandwidth of a typical laser diode array (~2 nm).

The increase of output energy with [Cs] is attributed to more Cs atoms available to participate in the stimulated emission process. However, the laser output energy on and near the D_2 resonance line at 852.1 nm increases at a slower rate with [Cs] near the other spectral regions of Fig. 5.4. This is attributed to the combination of parasitic oscillations occurring between the gas cell windows and multiphoton ionization. The observation of parasitic laser action is believed to be particularly significant as this experiment employed a cell with plane parallel windows. Finally, it should be noted that the significant and asymmetric increase of the FWHM of the D_2 line bandwidth to ~1.5 nm is attributed, particularly on the red side, to excitation of the large R portion of both the $B^2\Sigma^+_{1/2}$ and $A^2\Pi_{3/2}$ Cs-Ar states.

The first step in characterizing the laser involved measuring the output pulse energy (E_o) as a function of incident pump energy (E_i). This data is presented in Fig. 5.5 for [Cs] = 1.1×10^{14} cm^{-3} (solid black circles), 3.8×10^{14} cm^{-3} (open red squares), and 7.2×10^{14} cm^{-3} (solid blue triangles). These values of [Cs] correspond to gas cell temperatures of 409 K, 435 K, and 450 K, respectively. In these and subsequent absolute energy curves, measurements of E_o and E_a (pump energy absorbed) were made while sweeping E_i by means of a variable attenuator.

An important characteristic of Fig. 5.5 is that, over this temperature range, the threshold energy is a weak function of temperature with values of approximately 0.45 mJ at 409 K, 0.38 mJ at 435 K and 0.40 mJ at 450 K. This is attributed to

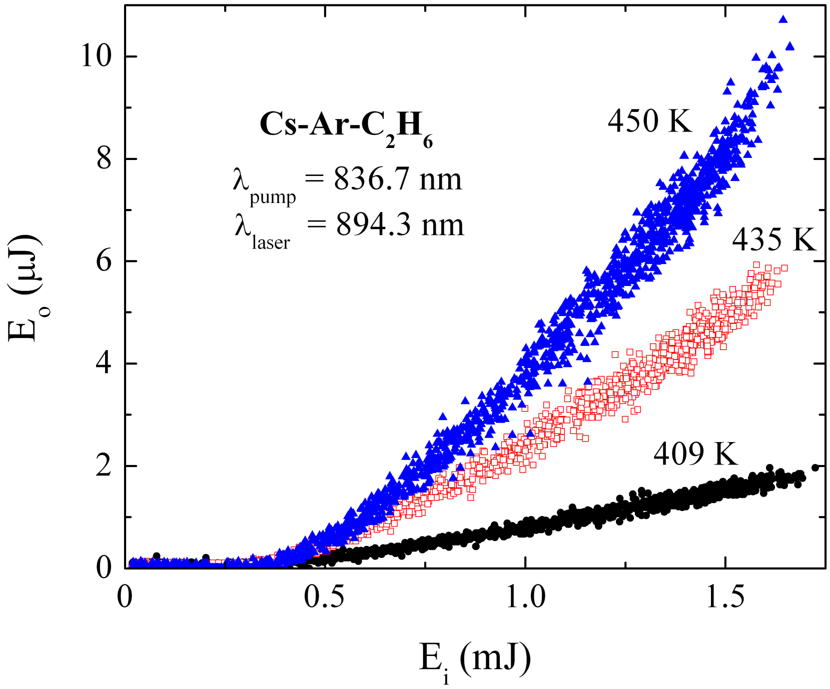

Figure 5.5: Output pulse energy (E_o) as a function of incident energy (E_i) for Cs-Ar-C_2H_6 measured at gas cell temperatures of 409 K, 435 K, and 450 K (corresponding to [Cs] = 1.1×10^{14} cm^{-3}, 3.8×10^{14} cm^{-3}, and 7.2×10^{14} cm^{-3}, respectively).

the competition between the requirement to excite more Cs atoms from the ground state in order to reach inversion at higher temperatures and the linear increase of α with [Cs], as indicated by Eqn. 3.5. Slope efficiencies are estimated to increase from approximately 0.2% at 409 K to 0.4% at 435 K to 0.9% at 450 K. As in the case of Fig. 5.4, this increase is attributed to a greater number of Cs atoms in the pump volume with which the pump field may interact.

It is also possible to obtain plots of E_o as a function of laser pump energy absorbed (E_a) as opposed to E_i. Because this conversion eliminates the temperature dependence of α, this type of graph provides better insight into the relaxation pathways of an excited Cs atom. More specifically, it also gives clues as to how a well designed, large-scale system may behave. To this end, Fig. 5.6 is a graph comparing the three-level alkali laser pumping process (directly photoexciting the 852.1 nm resonance, indicated by solid circles) with the XPAL scheme (pumping on the peak of the blue satellite, indicated by open circles). A temperature of 435±2 K ([Cs] = 3.8×10^{14} cm^{-3}) was chosen for these experiments because parasitic processes (which manifested as reduced efficiency when pumping the D_2 line in Fig. 5.4) were not observed at this temperature.

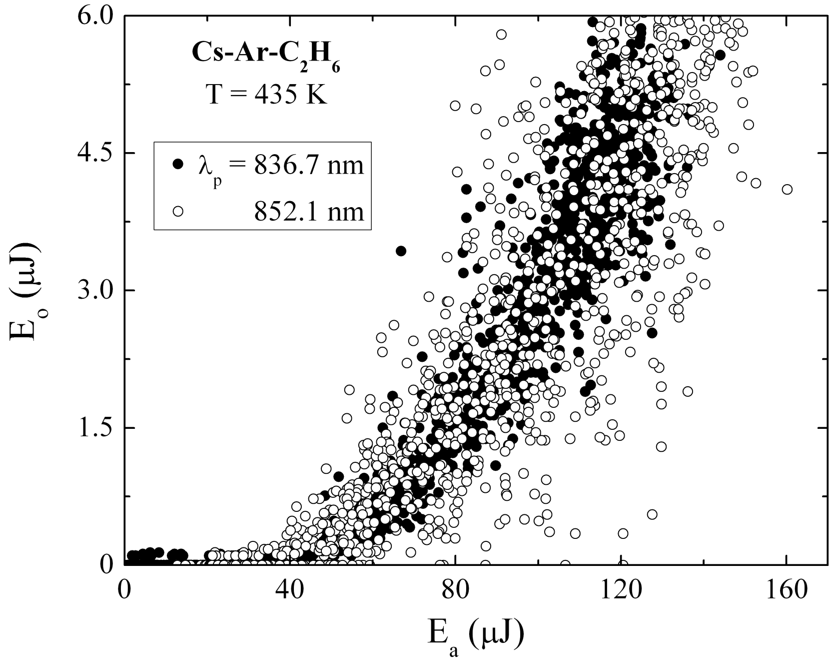

Figure 5.6: Output pulse energy (E_o) as a function of energy absorbed (E_a) for [Cs] = 3.8×10^{14} cm^{-3} (435 K) at pump wavelengths of 836.7 nm (●) and 852.1 (○).

For both pump wavelengths presented in Fig. 5.6, threshold is ∼40 μJ and the slope efficiency approaches ∼10%. This result demonstrates that, on a per photon absorbed basis, there are no additional loss mechanisms present in the XPAL scheme which do not exist with direct atomic excitation. This behavior is attributed to the fast (ps time scale) dissociation of Cs-Ar($B^2\Sigma^+_{1/2}$) into Cs($6^2P_{3/2}$) which occurs sufficiently rapidly that competitive loss processes are negligible. With regard to the ultimate performance of a high power diode-pumped system, this result implies that the XPAL scheme is just as viable for scaling as are the three-level alkali laser systems.

5.2.2 Cs-Kr-C_2H_6 Laser Operation at 894 nm

Following the demonstration of five-level operation in Cs-Ar-C_2H_6 mixtures, similar observations of 894 nm laser action were made in Cs-Kr-C_2H_6 [57] mixtures with the goal of highlighting the flexibility of the XPAL scheme based on perturber selection. The Cs-Kr D_2 blue satellite peaks at approximately 841.1 nm as is observed in the excitation spectra of Fig. 5.7 for 894 nm laser operation for $[Cs] = 1.6 \times 10^{13}$ cm^{-3}, 5.4×10^{14} cm^{-3}, and 1.5×10^{15} cm^{-3} (corresponding to 374 K, 443 K, and 468 K, respectively). The region of λ_p<847 nm has been magnified by a factor of ten for clarity.

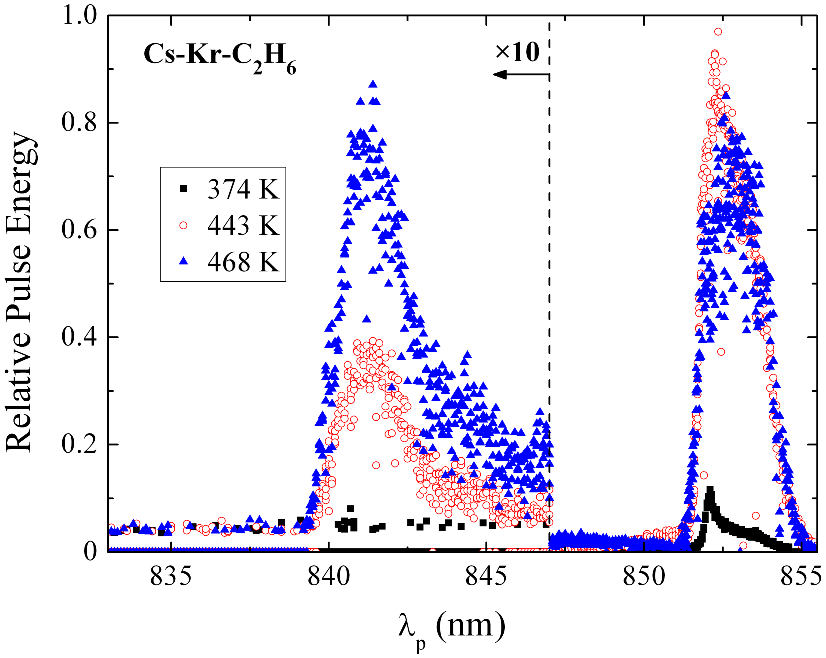

Figure 5.7: Excitation spectra for Cs-Kr-C_2H_6 taken at gas cell temperatures of 374 K, 443 K and 468 K (corresponding to $[Cs] = 1.6 \times 10^{13}$ cm^{-3}, 5.4×10^{14} cm^{-3}, and 1.5×10^{15} cm^{-3}, respectively). The region of λ_p<847 nm has been magnified by a factor of ten for clarity.

In addition to the blue satellite at ~841 nm, the red satellite peaking at ~853.3 nm is most clearly defined at 374 K. As observed in the Cs-Ar-C_2H_6 excitation spectra of Fig. 5.4, the blue satellite strength increases with [Cs] while the slope efficiency corresponding to direct atomic excitation declines significantly by T = 468 K. This decline is similarly attributed to excited state absorption, multiphoton ionization, and parasitic oscillation between the cell windows.

Figure 5.8 compares direct atomic photoexcitation at 852.1 nm (solid circles) with pumping on the peak of the blue satellite at 841.1 nm (open circles) at a temperature of 458 K, corresponding to [Cs] = 1.0×10^{15} cm^{-3}. For blue satellite pumping, threshold is observed to be ∼85 μJ. The slope efficiency appears to increase with E_a, increasing from $3.3 \pm 1.1\%$ immediately above threshold to >5% for pump pulse energies beyond ∼100 μJ. In contrast to the observations of Fig. 5.6 for Cs-Ar-C_2H_6, direct D_2 excitation does not have the same characteristics as do those observed when pumping the blue satellite. For λ_p = 852.1 nm, threshold is approximately 120 μJ, ∼40% larger than that observed when λ_p = 836.7 nm. The slope efficiency is also lower, with a value of $2.4 \pm 0.6\%$ immediately after threshold. The mean threshold for D_2 excitation is estimated to be 30% lower than that observed for excimer pumping. These differences in threshold and slope efficiency are attributed to the increased prominence of competitive processes for higher values of [Cs] as observed in Fig. 5.7.

Figure 5.9 compares Cs-Kr-C_2H_6 laser operation under λ_p=841.1 nm for gas cell temperatures of three sets of 444 K, 458 K, and 468 K (corresponding to [Cs] = 5.6×10^{14} cm^{-3}, 1.0×10^{15} cm^{-3}, and 1.5×10^{15} cm^{-3}, respectively). The pump threshold energies at these temperatures (40 μJ, 85 μJ, and 140 μJ, respectively) are approximately linear with [Cs] as is expected for a laser transition terminating on the ground state. The slope efficiencies of the curves slowly decrease with [Cs], behavior that appears to be related to decline in efficiency observed for D_2 excitation in Fig. 5.4.

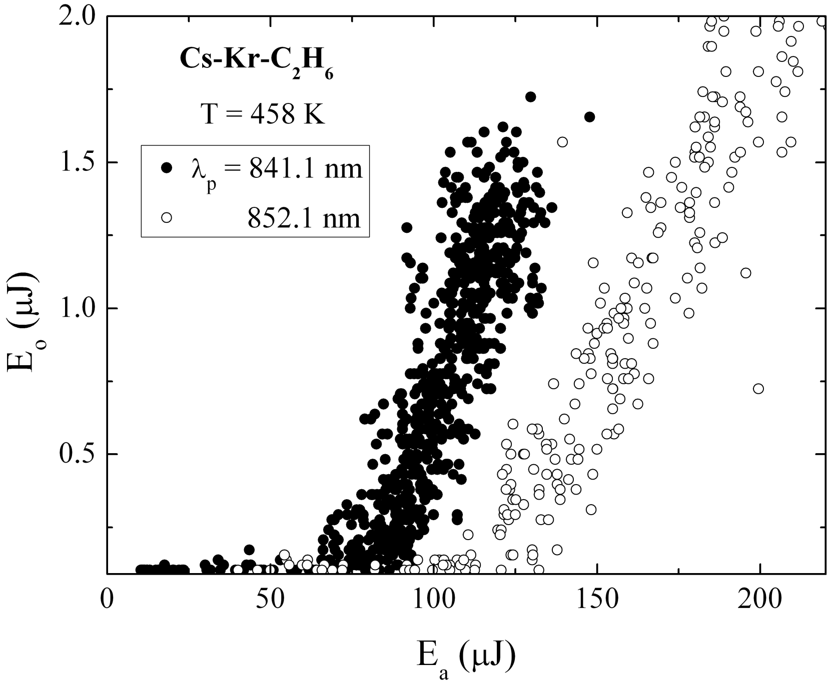

Figure 5.8: Output pulse energy (E_o) as a function of energy absorbed (E_a) for [Cs] = 1.0×10^{15} cm^{-3} (458 K) at pump wavelengths of 841.1 nm (•) and 852.1 (◦).

5.2.3 Rb-Kr-C_2H_6 Laser Operation at 795 nm

In order to demonstrate that the XPAL scheme is applicable to a variety of alternative lasing species and perturbers, oscillator experiments were also performed with a Rb-Kr gas mixture. In these experiments, the high reflector was replaced with a flat mirror having R>99% over the 700-900 nm spectral range. Figure 5.10 shows the excitation spectra obtained for laser output on the D_1 transition at 795 nm in a gas cell containing Rb, [Kr] = 1.6×10^{19} cm^{-3}, and [C_2H_6] = 3.2×10^{18} cm^{-3} at temperatures of 435 K and 454 K (corresponding to [Rb] = 1.5×10^{14} and 3.6×10^{14}, respectively).

For Rb, the D_2 transition occurs at 780 nm. The significant, asymmetrical broadening to the red of the D_2 line as observed in Fig. 5.10 is attributed to the red satellite of this transition. The blue satellite peaks at approximately 760 nm. An interesting feature in Fig. 5.10, not observed in the Cs experiments, is the sharp peak at

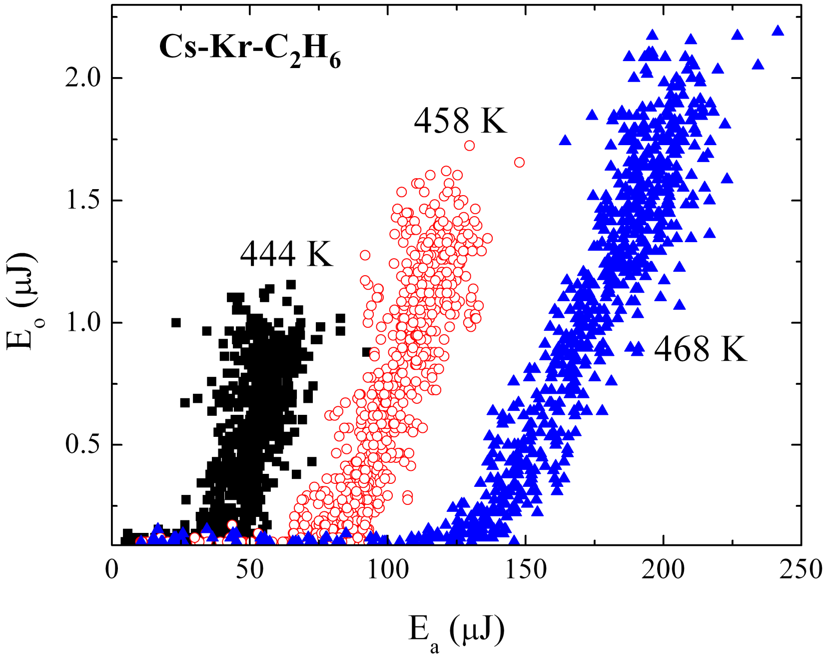

Figure 5.9: Plot of output pulse energy (E_o) as a function of energy absorbed (E_a) in a Cs-Kr-C_2H_6 mixture at gas cell temperatures of 444 K, 458 K, and 468 K (corresponding to [Cs] $= 5.6\times10^{14}$ cm^{-3}, 1.0×10^{15} cm^{-3}, and 1.5×10^{15} cm^{-3}, respectively).

777.8 nm. This corresponds to a two-photon absorption process which populates the $5^2D_{5/2}$ state. This state appears to decay primarily to the $5^2P_{3/2}$ state since spontaneously emitted 420 nm light corresponding to the $6^2P_{3/2} \rightarrow 5^2S_{1/2}$ transition was observed by eye in the presence of the dye laser pump. This fluorescence was too weak too be detected by the spectrometers available at the time.

As indicated by Fig. 5.10, pumping these two-photon transitions also produces lasing at 795 nm. Because the $6^2P_{3/2} \rightarrow 5^2P_{1/2,3/2}$ transition is forbidden by the $\Delta L = \pm 1$ selection rule for dipole transitions, it is presumed that there is a multiple step relaxation process involved in repopulating the $5^2P_{1/2}$ state. Since the lifetimes of the Rb 5P states are short (∼27 ns [58]), these relaxation processes must occur quickly, and it is possible that lasing is occurring on the intermediate transitions as well. Figure 5.11 illustrates one possible variant of the two-photon excitation and subsequent relaxation which would result in the observation of $6^2P_{3/2} \rightarrow 5^2S_{1/2}$

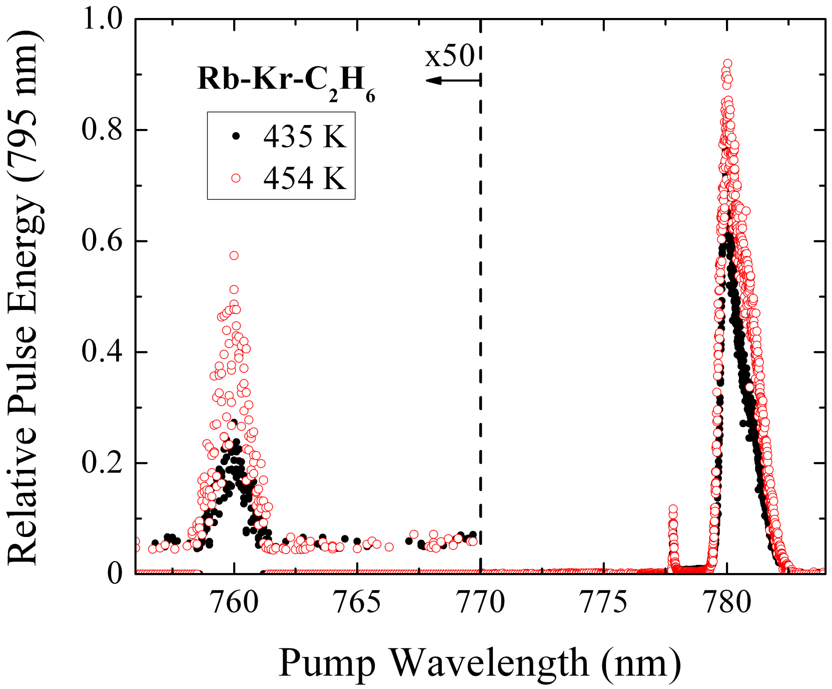

Figure 5.10: Excitation spectra for Rb-Kr-C_2H_6 taken at gas cell temperatures of 435 K and 454 K (corresponding to [Rb] = 1.5×10^{14} cm^{-3} and 1.3×10^{15} cm^{-3}, respectively). Note that the region $\lambda_p \leq 770$ nm has been magnified by a factor of 50 for clarity.

(420 nm) fluorescence and $6^2P_{3/2} \rightarrow 5^2S_{1/2}$ (795 nm) laser action. Unfortunately, the Pyrex gas cell absorbs the radiation in the 1–4 μm region, preventing observation of the emission from many of the intermediate transitions. Further experiments employing cell materials transmissive in this spectral region (e.g. Al_2O_3) are necessary in order to probe the decay channels involved in producing the observed D_1 laser action.

5.3 Four-Level Laser Operation on the $n^2P_{3/2} \rightarrow n^2S_{1/2}$ Transition

At the onset of this work, it was unclear whether or not it would be possible to obtain lasing on an $n^2P_{3/2} \rightarrow n^2S_{1/2}$ alkali transition with collision pair photoexcitation. Although dissociation of alkali-rare gas diatomics populates the $^2P_{3/2}$ state,

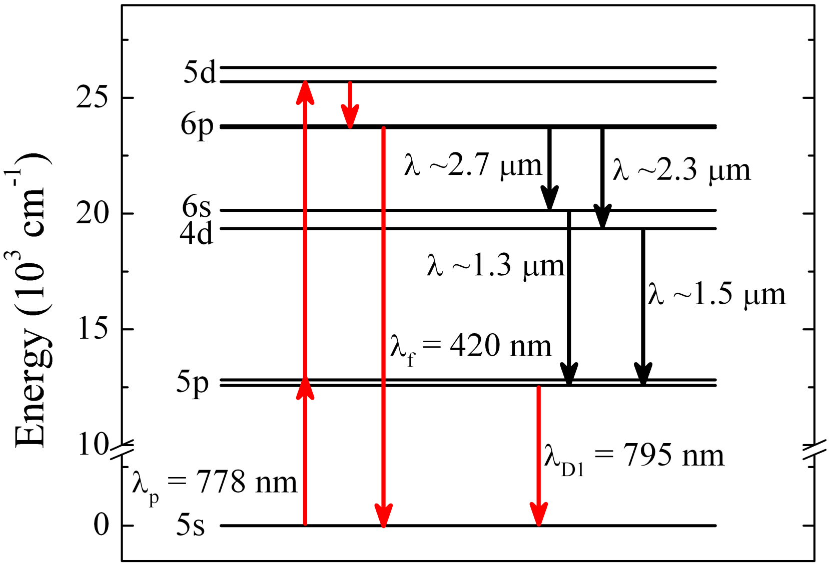

Figure 5.11: Energy level diagram of atomic Rb indicating the lowest lying excited state energy levels and one variant of the possible two-photon excitation and subsequent relaxation which would lead to the observed 420 nm fluorescence and laser action at 795 nm.

the degeneracy of the level is twice that of the $^2P_{1/2}$ state and correspondingly raises the pump power threshold. If pump intensity was not a concern, it was hypothesized that removal of the collisional relaxant from the gas mixture would allow for sufficient population buildup in the $^2P_{3/2}$ state. This laser scheme is illustrated in Fig. 5.12.

Beyond pump limitations, there was concern that four-level operation would be equivalent to a two-level system on which inversion would not be possible. The interpretation of the system as two or four-levels depends on the nature of collisional coupling between the molecular and atomic states, specifically the $^2P_{3/2}/B^2\Sigma^+_{1/2}$ and $^2S_{1/2}/X^2\Sigma^+_{1/2}$ energy level pairs. If these levels were collisionally coupled to such a degree that population transfer between the members of each pair is essentially instantaneous, as may be suggested by the ps-scale time between collisions, the states would behave as a quasi two-level system in which it would be impossible to observe laser action. Fortunately, as is discussed in the following sections, this was not the case as the molecular states, although extremely short lived, behave as unique, discrete

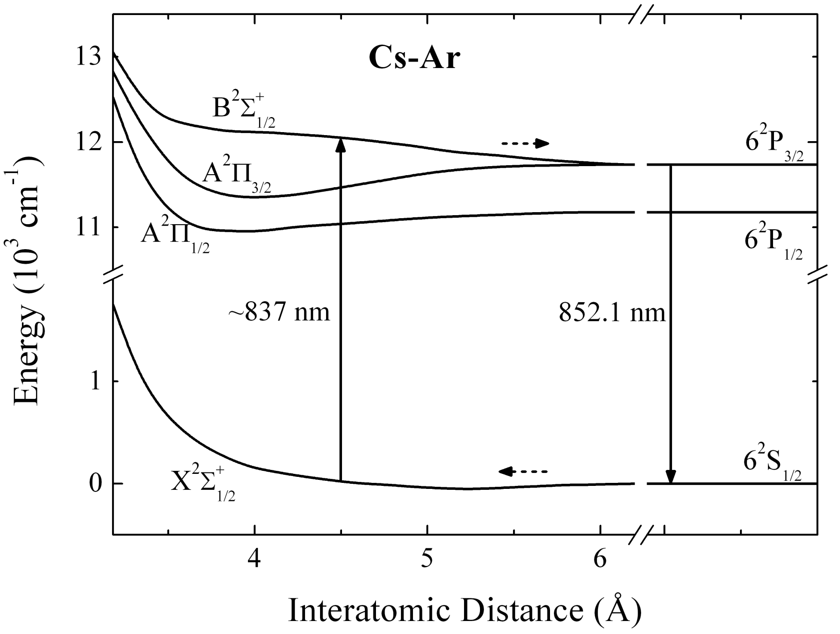

Figure 5.12: Interaction potentials of Cs-Ar adapted from [14]. The arrows indicate the pumping pathway utilized in obtaining lasing on the $6^2P_{3/2}$→$6^2S_{1/2}$ transition at 852.1 nm.

states and make a four-level XPAL possible. As discussed in Chapter 1, four-level operation has the added advantages of increased quantum efficiency relative to five-level operation and not requiring a collisional relaxant species, particularly one such as C_2H_6 which degrades over time.

5.3.1 Cs-Ar Laser Operation at 852 nm

Figure 5.13 presents the excitation spectra obtained in a binary gas mixture containing Cs and [Ar] $= 1.6 \times 10^{19}$ cm^{-3} [59]. As in previous excitation spectra, the output energy was normalized to the input energy to account for the dye tuning curve. However, every point in Fig. 5.13 corresponds to the average of four such measurements instead of a single pulse. A bandpass filter centered at 852 nm with a spectral width of ~8 nm and a transmission of 45±5% was used to ensure the that the pump did not contribute to output energy measurements. The spectral proximity of the pump and output wavelengths limited λ_p to $\leq$841 nm, as signal isolation was not guaranteed for longer wavelengths. Data are shown for gas cell temperatures of 464 K, 475 K, and 485 K, corresponding to [Cs] values of 1.3×10^{15} cm^{-3}, 1.9×10^{15} cm^{-3}, and 2.8×10^{15} cm^{-3}, respectively.

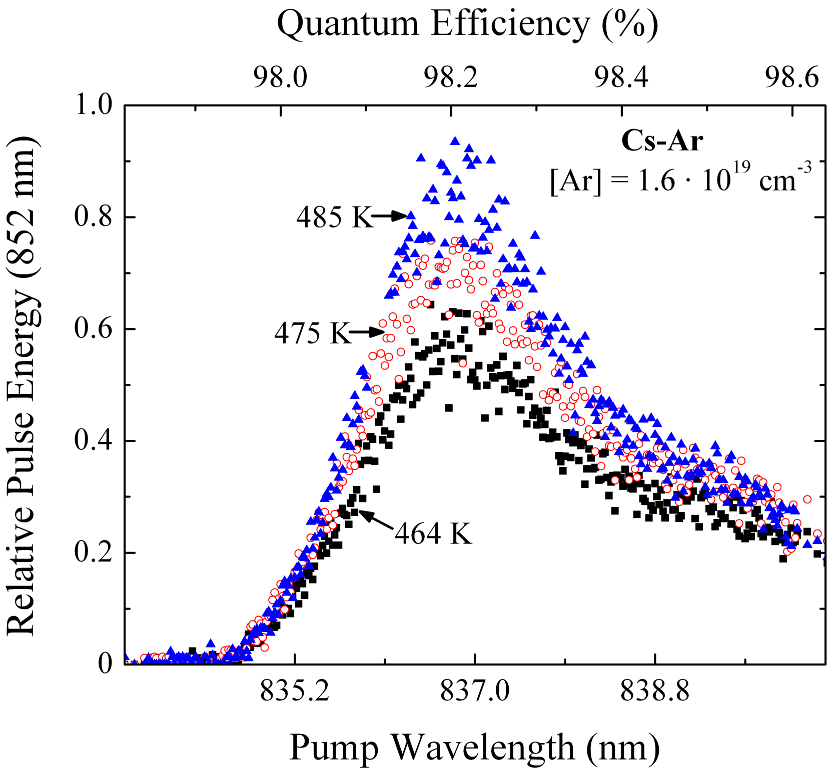

Figure 5.13: Excitation spectra obtained by monitoring the relative output pulse energy at 852.1 nm as a function of the pump laser wavelength. Each point is the average of four measurements. The black squares correspond to T = 464 K ([Cs] = 1.3×10^{15} cm^{-3}), the red circles to T = 475 K ([Cs] = 1.9×10^{15} cm^{-3}), and the blue triangles to T = 485 K ([Cs] = 2.8×10^{15} cm^{-3}).

At all of these temperatures, the blue satellite is well defined and peaks at approximately 836.7 nm with a spectral breadth of $\gtrsim$3 nm. The upper abscissa of Fig. 5.13 indicates the quantum efficiency calculated from the pump wavelength, and illustrates that >98% is obtained for all values of $\lambda_p \gtrsim 835$ nm.

The corresponding plot of E_o as a function of E_i is presented in Fig. 5.14. For each of the temperatures presented (T =464 K, 475 K, and 485 K), threshold is observed to be approximately constant with a value of ~0.8 mJ. This is consistent with the observations of Fig. 5.5.

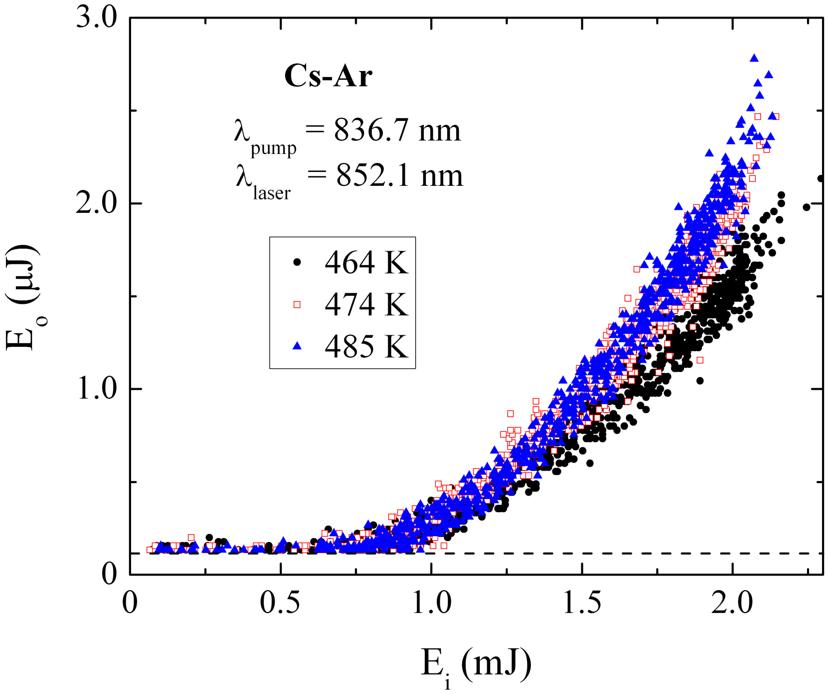

Figure 5.14: Output pulse energy (E_o) as a function of incident energy (E_i) at $\lambda_p =$ 836.7 nm. The solid black circles correspond to T = 464 K ([Cs] = 1.3×10^{15} cm^{-3}), the open red squares to T = 474 K ([Cs] = 1.9×10^{15} cm^{-3}), and the solid blue triangles to T = 485 K ([Cs] = 2.8×10^{15} cm^{-3}). The dashed horizontal line indicates the minimum detectable energy.

Figure 5.15 depicts E_a as a function of E_o with a pump wavelength of 836.7 nm for temperatures almost identical to those in Fig 5.13 (464 K, 474 K, and 485 K), which correspond to [Cs] values of 1.3×10^{15} cm^{-3}, 1.9×10^{15} cm^{-3}, and 2.8×10^{15} cm^{-3}. Threshold energies of approximately 130 μJ, 175 μJ and 250 μJ are approximately linear with [Cs], as was also observed in Fig. 5.9. The overall slope efficiencies increase with [Cs], but for a fixed temperature appear to increase with E_a. These observations and behaviors are consistent with those obtained for excimer-pumped Cs D_1 line laser operation [56], [57].

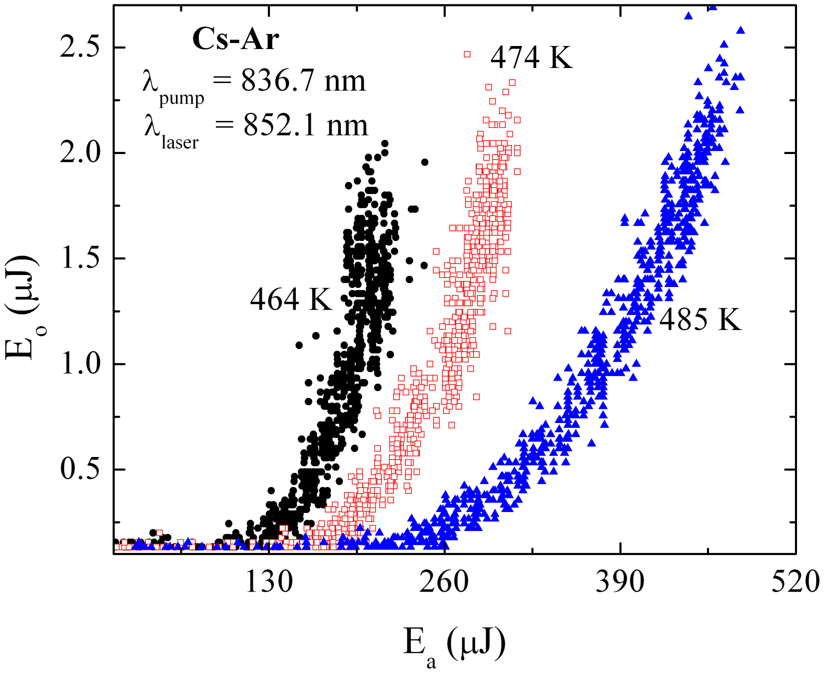

Figure 5.15: Output pulse energy (E_o) as a function of energy absorbed (E_a) at $\lambda_p =$ 836.7 nm. The solid black circles correspond to T = 464 K ([Cs] = 1.3×10^{15} cm^{-3}), the open red squares to T = 474 K ([Cs] = 1.9×10^{15} cm^{-3}), and the solid blue triangles to T = 485 K ([Cs] = 2.8×10^{15} cm^{-3}).

5.3.2 Observation of Three-Body Photoassociation in Laser Characteristics

The impact of three-body photoassociation resulting in overall absorption enhancement was not limited to the absorption experiments described in Section 4.2. This is exemplified by oscillator experiments performed in Cs-Ar-Kr mixtures containing [Ar] = [Kr] = 8.1×10^{18} cm^{-3} [59]. As illustrated in Fig. 5.16, the excitation spectrum obtained for [Cs] = $1.3 \pm 0.1 \times 10^{15}$ cm^{-3} (464±2 K) in the Cs-Ar-Kr mixture has a lineshape almost identical to that of Cs-Ar with both peaking at ∼836.7 nm. The absence of a peak near 841 nm, corresponding to Cs-Kr absorption, indicates that the Cs-Kr contribution at 841.1 nm is suppressed in these experiments just as was observed in the absorption experiments of Fig. 4.4.

The upper graph of Fig. 5.17 plots E_o as a function of E_i in both Cs-Ar and Cs-Ar-

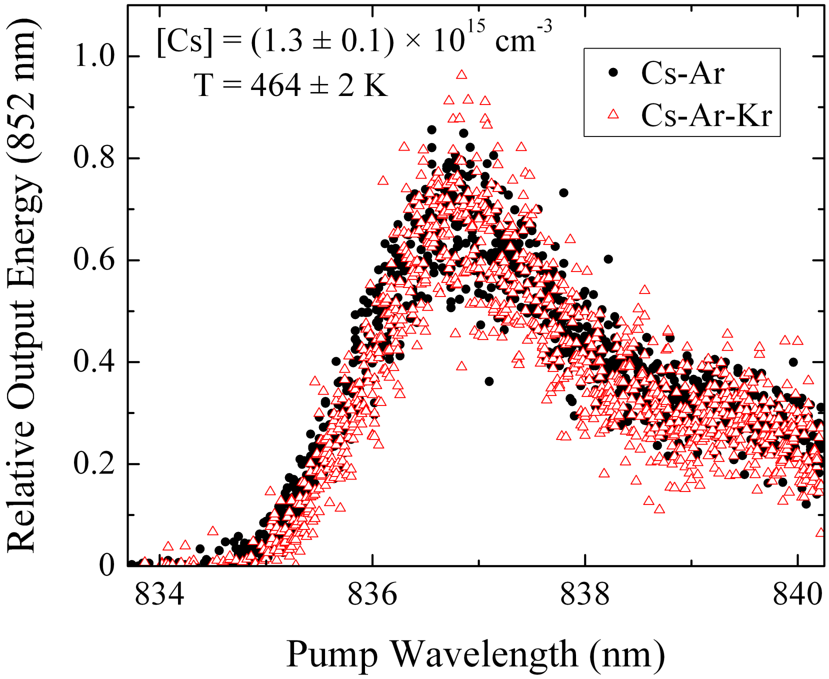

Figure 5.16: Comparison of excitation spectra for laser action at 852 nm in Cs-Ar and Cs-Ar-Kr mixtures at a cell temperature of 464 K ([Cs] = 1.3×10^{15} cm^{-3}).

Kr mixtures at 464±2 K. Under these conditions, threshold is observed to be ~830 μJ for Cs-Ar and ~600 μJ for Cs-Ar-Kr. This makes the threshold for Cs-Ar-Kr ~28% less than that for Cs-Ar mixtures, although this value may be exaggerated somewhat by the minimum detectable energy as indicated by the horizontal dashed line.

The lower graph of Fig. 5.17 plots E_o as a function of E_a. This data shows that, to within experimental uncertainty, the two lasers are identical on a per-photon-absorbed basis. This indicates that three-body photoassociation can be employed as a means of adjusting the absorption coefficient without decreasing laser efficiency.

A similar effect is evident in the absorption observed for the quaternary mixture of Cs-Ar-Kr-C_2H_6. The composition of this mixture (discussed in Sect. 4.2.2) was [Ar] = [Kr] = 8.0×10^{18} cm^{-3} and [C_2H_6] = 3.2×10^{18} cm^{-3} and it was expected that the presence of C_2H_6 would result in five-level operation at 894 nm. However, laser action was instead observed at 852 nm. This unexpected behavior is attributed to the increase in absorption which, in turn, provides sufficiently high gain that

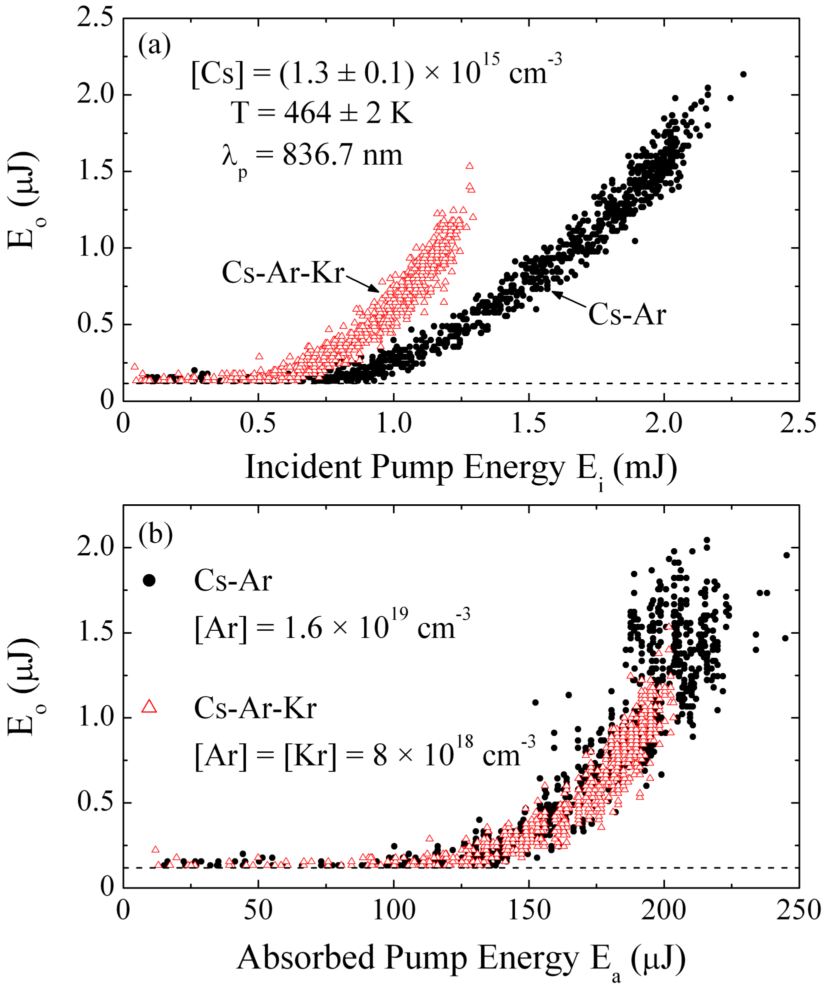

Figure 5.17: (a) Output pulse energy (E_o) as a function of incident energy (E_i) and (b) energy absorbed (E_a) at $\lambda_p = 836.7$ nm in both Cs-Ar and Cs-Ar-Kr mixtures. The cell temperature of 464 K corresponds to [Cs] $= 1.3 \times 10^{15}$ cm^{-3}.

the stimulated emission rate is faster than collisional relaxation. Figure 5.18 plots excitation spectra obtained in this mixture for gas cell temperatures of 429 K, 444 K, and 460 K corresponding to [Cs] $= 2.9 \times 10^{14}$ cm^{-3}, 5.6×10^{14} cm^{-3}, and 1.1×10^{15} cm^{-3}, respectively.

Although much remains to be explained about three-body photoassociation, the results of these oscillator experiments further underscore the potential utility of introducing multiple perturbing species into an XPAL. Furthermore, using the laser itself as an extremely sensitive probe of the photoassociation kinetics will provide

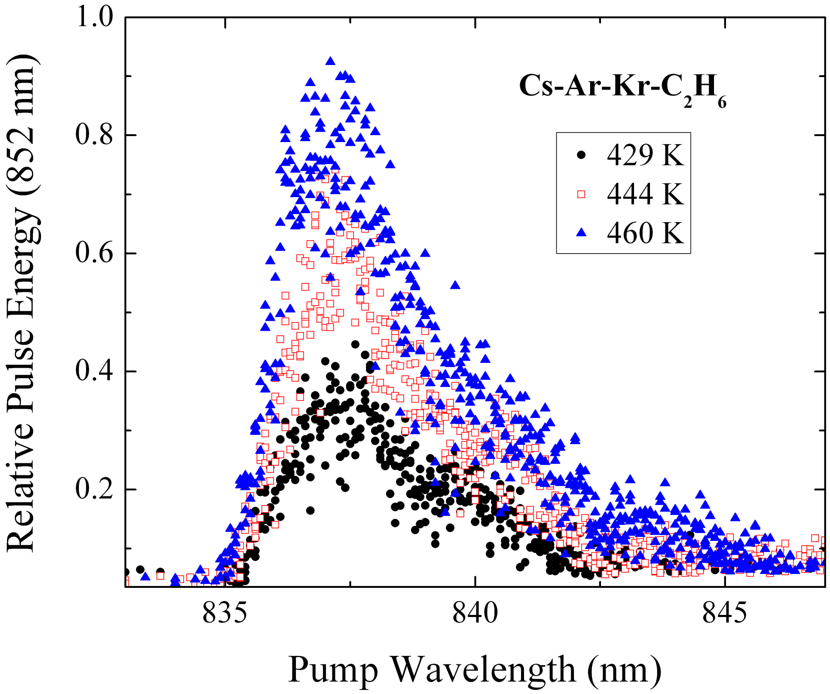

Figure 5.18: Excitation spectra for laser action at 852 nm in a Cs-Ar-Kr-C_2H_6 mixture where at temperatures of 429 K, 444 K, and 460 K ([Cs] = 2.9×10^{14} cm^{-3}, 5.6×10^{14} cm^{-3}, and 1.1×10^{15} cm^{-3}, respectively).

additional insight into these processes by complementing the absorption data.

CHAPTER 6

TIME-DEPENDENT RATE EQUATION MODELING

In order to fully utilize an XPAL laser as a sensitive probe of the underlying photoassociation kinetics, it is necessary to develop a model which includes as many of the relevant processes as possible. In the following sections, the development of a time-dependent rate equation XPAL model for pumping near the peak of the Cs D_2 blue satellite is described and its predictions compared with experimental results. This model, which was written in Mathematica, is capable of accepting a temporally arbitrary pump pulse, making it suitable for study of the short, high intensity pulses incident from the dye laser.

6.1 Assumptions and Approximations

There are several key assumptions and approximations made in the model which are important to consider. The first of these is the strong-pump approximation, in which the intensity of the incident pump beam is treated as being uniform along the length of the gas cell. Assuming a fixed value of $[\mathrm{Ar}] = 1.6 \times 10^{19}$ cm^{-3}, this approximation is accurate to within ~15% after a double pass through a 10 cm cell for temperatures <435 K. Figure 6.1 illustrates the temperature dependence of the transmission of the pump through 20 cm of the gain medium. In order to explore temperatures significantly higher than 435 K, the model would require the introduction of a spatially dependent pump along the optical axis. Similarly, the pump intensity was assumed to be uniform over the entire elliptical cross section of the pump beam. A more thorough treatment would include the spatial variation of the pump beam.

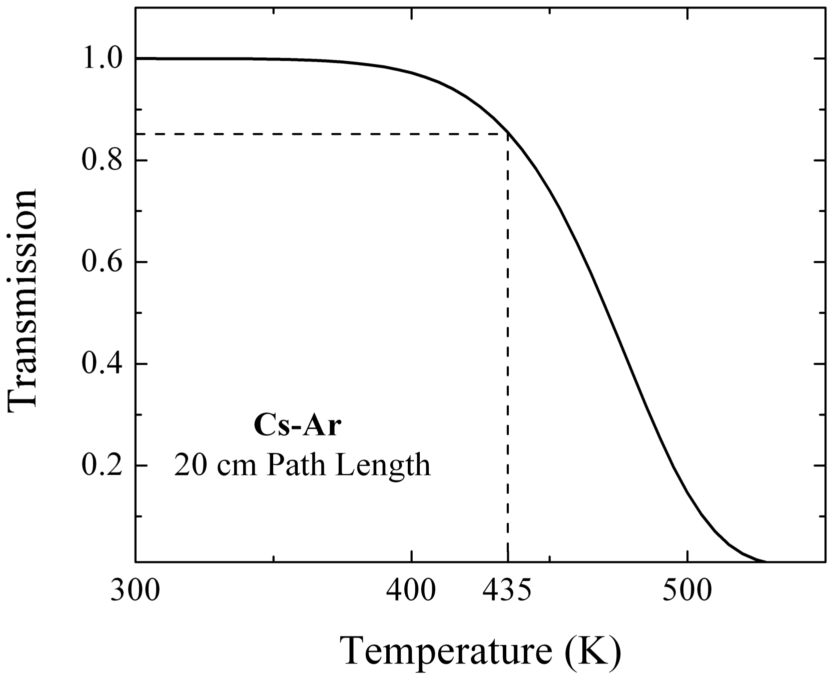

Figure 6.1: The transmission through a 20 cm long Cs-Ar ([Ar] = 1.6×10^{19} cm^{-3}) gas cell versus temperature for the peak of the blue satellite at 836.7 nm.

In addition to the aforementioned pump beam approximations, several assumptions were also made regarding the molecular kinetics. The first is the omission of the $A^2\Pi_{1/2}$ and $A^2\Pi_{3/2}$ states. Because both of these states are weakly bound (~1-3 k_BT), the steady state populations in both states are assumed to be negligible. Although the actual $B^2\Sigma^+_{1/2}$ and $X^2\Sigma^+_{1/2}$ states are continuous functions of R, each is treated as a distinct state extending over the blue satellite region.

Excited state absorption, multi-photon ionization (MPI), and energy pooling collisions all serve as loss mechanisms for XPAL operation [60–62]. For the pump intensities employed (on the order of 1 MW/cm^2), cross sections available in the literature suggested that excited state absorption was the strongest competitor with laser operation. Although the cross sections for excited state absorption from the $6^2P_{1/2}$ and $6^2P_{3/2}$ energy levels to higher lying atomic states (particularly $6^2D_{3/2,5/2}$) via the optical fields present in these experiments have never been measured, a cross section of $\sigma_e = 1 \times 10^{-17}$ cm^2 was estimated from that for resonant excitation of the $6^2\mathrm{D}_{3/2,5/2} \leftarrow 6^2\mathrm{P}_{1/2,3/2}$ transitions [63]. As will be discussed in more detail, laser behavior is closely tied to the exact value of σ_e. Energy pooling collisions and MPI were both omitted from the simulations due to their relatively small cross sections, as compared to excited state absorption.

6.2 Rate Constants

The model results described here correspond to both Cs-Ar and Cs-Ar-C_2H_6 mixtures in which [Ar] $= 1.6 \times 10^{19}$ cm^{-3} and [C_2H_6] varied depending on the simulation. This section discusses the rates of all the processes included in the model, along with derivations where necessary.

In order to determine the rates of atomic association and molecular dissociation, the average relative velocity between the Cs and Ar atoms must first be calculated using the relation

$$v_{Cs-Ar} = \sqrt{\frac{8\mathrm{k_B T}}{\pi}\left(\frac{1}{m_{Cs}} + \frac{1}{m_{Ar}}\right)}, \tag{6.1}$$

where m_{Cs} and m_{Ar} are the Cs and Ar masses, respectively [46]. The value of v_{Cs-Ar} can be then be employed in the expression for the collision rate between two different species,

$$Z_{Cs-Ar} = \pi \; v_{Cs-Ar} \; d_{Cs-Ar} \; [\mathrm{Ar}], \tag{6.2}$$

where d_{Cs-Ar} is the interatomic separation at which the interaction is considered a collision [46]. A value of $d_{Cs-Ar} = 5 \times 10^{-8}$ cm is chosen, as this is the approximate separation of Cs and Ar which corresponds to the peak blue satellite absorption. Defining Z_{Cs-Ar} as the $\mathrm{X}^2\Sigma^+_{1/2}$ state association rate γ_{xa}, the $\mathrm{X}^2\Sigma^+_{1/2}$ state dissociation rate γ_{xd} is estimated with the expression

$$\gamma_{xd} = \gamma_{xa}\frac{[\mathrm{Cs}]_0}{[\mathrm{CsAr}]_0}, \tag{6.3}$$

where $[\mathrm{CsAr}]_0$ is the density of ground state Cs-Ar pairs that are available to contribute to the blue satellite feature. The subscript 0 indicates that these values correspond to the steady-state distributions in the absence of an optical field. Knowledge of $[\mathrm{Cs}]_{0,total}$, which corresponds to the total vapor pressure when no Cs atoms are excited, allows for calculation of $[\mathrm{Cs}]_0$ via $[\mathrm{Cs}]_{total}$ = $[\mathrm{Cs}]_0$ - $[\mathrm{CsAr}]_0$ where $[\mathrm{CsAr}]_0$ may be obtained from the expression [64]

$$[\mathrm{CsAr}]_0 = 4\pi R^2 \Delta R\ [\mathrm{Ar}]\ [\mathrm{Cs}]_{0,total}\ e^{\frac{-\Delta E}{\mathrm{k_B T}}}, \tag{6.4}$$

in which the ΔE is the energy difference between the satellite region of the X potential and the dissociation limit. The values of R^2 and ΔR were estimated from the Cs-Ar potential curves reported by Pascale and Vandeplanque [14].

An important characteristic of the values of γ_{xa} and γ_{xd} is that their ratio is such that the system returns to the equilibrium populations after the pump pulse is gone. Using these values, it is possible to estimate the $\mathrm{B}^2\Sigma^+_{1/2}$ state association and dissociation rates, denoted γ_{ba} and γ_{bd}, respectively. This calculation begins with the Boltzmann relation

$$\frac{N_u}{N_l} = \frac{g_u}{g_l} e^{\frac{-\Delta E}{\mathrm{k_B T}}}, \tag{6.5}$$

where N_u and N_l correspond to the populations in the upper and lower states, respectively. Similarly, g_u and g_l correspond to the degeneracies of the upper and lower states. This relationship can be employed to estimate γ_{ba} and γ_{bd} using γ_{xa} and γ_{xd} as follows:

$$\gamma_{bd} = \gamma_{xd}\frac{1}{2}\exp\left[\left((E_{X^2\Sigma^+_{1/2}} - E_{6^2S_{1/2}}) - (E_{6^2P_{3/2}} - E_{B^2\Sigma^+_{1/2}})\right)/\mathrm{k_B T}\right] \tag{6.6}$$

and

$$\gamma_{ba} = \gamma_{xa}2\exp\left[\left((E_{6^2P_{3/2}} - E_{B^2\Sigma^+_{1/2}}) - (E_{X^2\Sigma^+_{1/2}} - E_{6^2S_{1/2}})\right)/\mathrm{k_B T}\right], \tag{6.7}$$

where the ΔE values correspond to the energy separation between the subscripted energy levels. The factors of 1/2 and 2 were determined from the degeneracy ratios.

Upon determining all of the association and dissociation rates, the excited atomic states may be coupled using C_2H_6 as a collisional relaxant. The relative velocity between Cs and C_2H_6 species may be calculated from the expression

$$v_{Cs-C_2H_6} = \sqrt{\frac{8\mathrm{k_B T}}{\pi}\left(\frac{1}{m_{Cs}} + \frac{1}{m_{C_2H_6}}\right)}. \tag{6.8}$$

The corresponding transfer rate may then be obtained with the relation

$$\gamma_r = \sigma_{C_2H_6}\ v_{Cs-C_2H_6}\ [\mathrm{C_2H_6}], \tag{6.9}$$

where the value $\sigma_{C_2H_6} = 5.2\times10^{-15}$ cm^2 is assumed to be approximately constant over the 400-500 K range of temperatures [9]. Although the value has never been measured in Cs, experiments in Rb indicate that quenching of Cs($6^2P_{1/2}$) and Cs($6^2P_{3/2}$) by C_2H_6 has a rate constant ∼10% of that of γ_r [65].

Photons exit the laser resonator at a rate of $1/\tau_c$ where τ_c is the cavity lifetime which can be determined from the expression [66]

$$\tau_c = \frac{-2l_c}{c\ \log R_1 R_2}, \tag{6.10}$$

where R_1 and R_2 are the reflectivities of the two resonator mirrors and l_c is the length of the cavity.

One of the most important rates to determine is the pumping rate between the ground $\mathrm{X}^2\Sigma^+_{1/2}$ and excited $\mathrm{B}^2\Sigma^+_{1/2}$ molecular states. Pump intensity (W/cm^2) can be calculated via

$$I_p = \frac{E_p}{\tau_p A_p} \tag{6.11}$$

in which E_p is the energy of the pump pulse, τ_p is the pulse duration, and A_p is the cross sectional area of the beam. Using values of $E_p = 2$ mJ, $\tau_p = 4$ ns, and $A_p = 0.27$ cm^2 (for a 5 mm by 7 mm elliptical beam) yields $I_p = 1.9 \times 10^6$ W/cm^2-s. This value can then be used to determine the pumping rate Γ_p, by means of the expression

$$\Gamma_p = \frac{\sigma_{837} I_p}{h\nu_{837}}, \tag{6.12}$$

where σ_{837} is the absorption cross section and $h\nu_{837}$ is the energy of an 836.7 nm photon. Using a value of $\sigma_{837} = 2.1 \times 10^{-17}$cm^2 (estimated from the reduced absorption coefficient and the ratio of [Cs]$_0$/[CsAr]$_0$) and the I_p value calculated previously yields $\Gamma_p = 1.7 \times 10^8$ s^{-1}. Because I_p and Γ_p are functions of time in these experiments, they will be denoted as $I_p(t)$ and $\Gamma_p(t)$, respectively.

6.3 Rate Equations

Once rates have been estimated for all of the kinetics processes under consideration, a system of rate equations can be developed and solved to describe the time evolution of the populations under study. Figure 6.2 indicates all energy levels and transition rates included in the model. The solid and dashed lines in Fig. 6.2 correspond to radiative and nonradiative processes, respectively. Any rates or constants which appear in Fig. 6.2 (or are otherwise included in the model) which have not been explicitly discussed are tabulated and referenced in Table 6.1.

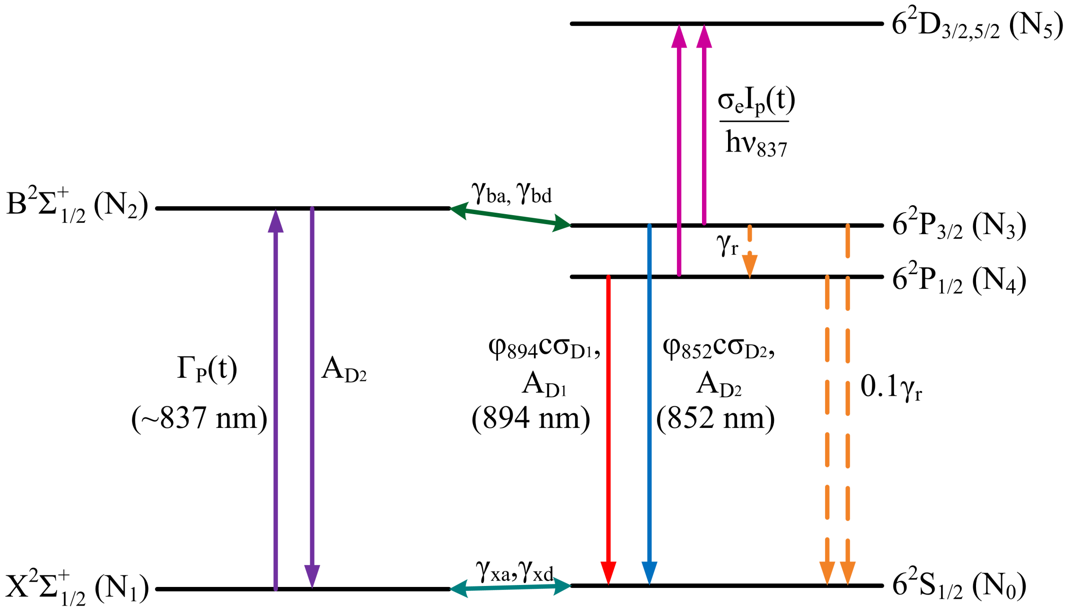

Figure 6.2: Energy level diagram indicating the various population transfer processes considered in the model. Solid lines indicate radiative transitions. Note that this diagram is not to scale.

Table 6.1: Important rates and constants which have not been previously discussed.

Symbol (Units)	Value	Reference
g_0, g_4	2	[46]
g_3	4	[46]
A_{D_2} (s^{-1})	3.28×10^7	[67]
A_{D_1} (s^{-1})	2.87×10^7	[67]
σ_{D_2} (cm^2)	$\approx 7.7 \times 10^{-12}$	[68]
σ_{D_1} (cm^2)	$\approx 5.0 \times 10^{-12}$	[68]
$\frac{p_l}{p_{D_2}}$	$\approx 10^{-8}$	[23]
$\frac{p_l}{p_{D_1}}$	$\approx 10^{-8}$	[23]

Assuming that the spontaneous emission rate A varies slowly with R, the rate equations can be written as

$$
\begin{aligned}
N_0'(t) = {} & \gamma_{xd}N_1(t) - \gamma_{xa}N_0(t) + A_{D_2}\left[N_2(t)+N_3(t)\right] + A_{D_1}N_4(t) \\
& + \phi_{894}(t)c\sigma_{D_1}\left[N_4(t) - \frac{g_4}{g_0}N_0(t)\right] + \phi_{852}(t)c\sigma_{D_2}\left[N_3(t) - \frac{g_3}{g_0}N_0(t)\right] \\
& + 0.1\gamma_r\left[N_3(t)+N_4(t)\right] \\
N_1'(t) = {} & \gamma_{xa}N_0(t) - \gamma_{xd}N_1(t) - \Gamma_p(t)\left[N_1(t) - \frac{g_1}{g_2}N_2(t)\right] - A_{D_2}N_2(t) \\
N_2'(t) = {} & \gamma_{ba}N_3(t) - \gamma_{bd}N_2(t) + \Gamma_p(t)\left[N_1(t) - \frac{g_1}{g_2}N_2(t)\right] - \frac{\sigma_e I_p(t)}{h\nu_{837}}N_2(t) \\
N_3'(t) = {} & \gamma_{bd}N_2(t) - \gamma_{ba}N_3(t) - \gamma_r\left[N_3(t) - \frac{g_3}{g_4}N_4(t)e^{\Delta E_{34}/\mathrm{k_B T}}\right] - A_{D_2}N_3(t) \\
& - 0.1\gamma_r N_3(t) - \frac{\sigma_e I_p(t)}{h\nu_{837}}N_3(t) - \phi_{852}(t)c\sigma_{D_2}\left[N_3(t) - \frac{g_3}{g_0}N_0(t)\right] \\
N_4'(t) = {} & \gamma_r\left[N_3(t) - \frac{g_3}{g_4}N_4(t)e^{\Delta E_{34}/\mathrm{k_B T}}\right] - A_{D_1}N_4(t) - 0.1\gamma_r N_4(t) \qquad (6.13) \\
& - \frac{\sigma_e I_p(t)}{h\nu_{837}}N_4(t) - \phi_{894}(t)c\sigma_{D_1}\left[N_4(t) - \frac{g_4}{g_0}N_0(t)\right] \\
N_5'(t) = {} & \frac{\sigma_e I_p(t)}{h\nu_{837}}\left[N_2(t)+N_3(t)+N_4(t)\right] \\
\phi_{852}'(t) = {} & \phi_{852}(t)c\sigma_{D_2}\left[N_3(t) - \frac{g_3}{g_0}N_0(t)\right] - \frac{\phi_{852}(t)}{\tau_c} + \frac{p_l}{p_{D_2}}A_{D_2}N_3(t) \\
\phi_{894}'(t) = {} & \phi_{894}(t)c\sigma_{D_1}\left[N_4(t) - \frac{g_4}{g_0}N_0(t)\right] - \frac{\phi_{894}(t)}{\tau_c} + \frac{p_l}{p_{D_1}}A_{D_1}N_4(t)
\end{aligned}
$$

where ϕ_{852} and ϕ_{894} are the photon number fluxes (photons/cm^3) at 852.1 nm and 894.3 nm, respectively [66]. In order to match the experimental work, a pulse duration of 4 ns (FWHM), a cavity length of 80 cm, and a double-pass pump geometry were assumed. Because population in the $6^2\mathrm{D}_{3/2,5/2}$ states (N_5) are relatively long-lived compared to the pump pulse duration and may not relax to populate the $6^2\mathrm{P}_{3/2}$ or $6^2\mathrm{P}_{1/2}$ upper laser levels, the model assumes that population does not exit the

$6^2D_{3/2,5/2}$ states. The initial conditions for this system of equations are

$$
\begin{aligned}
N_0(0) &= [\mathrm{Cs}]_0 \\
N_1(0) &= [\mathrm{CsAr}]_0 \\
N_2(0) &= N_3(0) = N_4(0) = N_6(0) = 0 \\
\phi_{852}(0) &= \phi_{894}(0) = 0
\end{aligned}
\tag{6.14}
$$

where it is clear that, prior to the pump pulse, no population exists in the excited energy levels. It is important to verify that the populations will decay back to these values after the optical pump field has exited the cavity.

6.4 Sensitivity Analysis

By integrating the photon fluxes obtained from a series of simulations with different pump intensities, the model can predict the threshold and slope efficiency of laser action. Using these results, a sensitivity analysis of the model was performed in order to determine which parameters these predictions are most dependent on. The results of this investigation are valuable because they indicate which constants future experiments should be designed to measure more accurately.

It was determined that the two most sensitive model parameters were the absorption coefficient of the blue satellite and the geometry of the pump laser beam. As discussed in Chapter 4, there is roughly a ±10% uncertainty in the measured values of α. Figure 6.3 presents E_o as a function of E_i for three values of α in a Cs-Ar-C_2H_6 gas mixture at 435 K (corresponding to $[\mathrm{Cs}] = 8.7 \times 10^{-3}$ cm^{-1}). The solid line corresponds to the experimentally determined value of $\alpha = 9.7 \times 10^{-3}$ cm^{-1}, where a threshold of $\sim$3.5 mJ is predicted. The two dashed curves of Fig. 6.3 illustrate the impact of varying α from its measured value by ±10%.

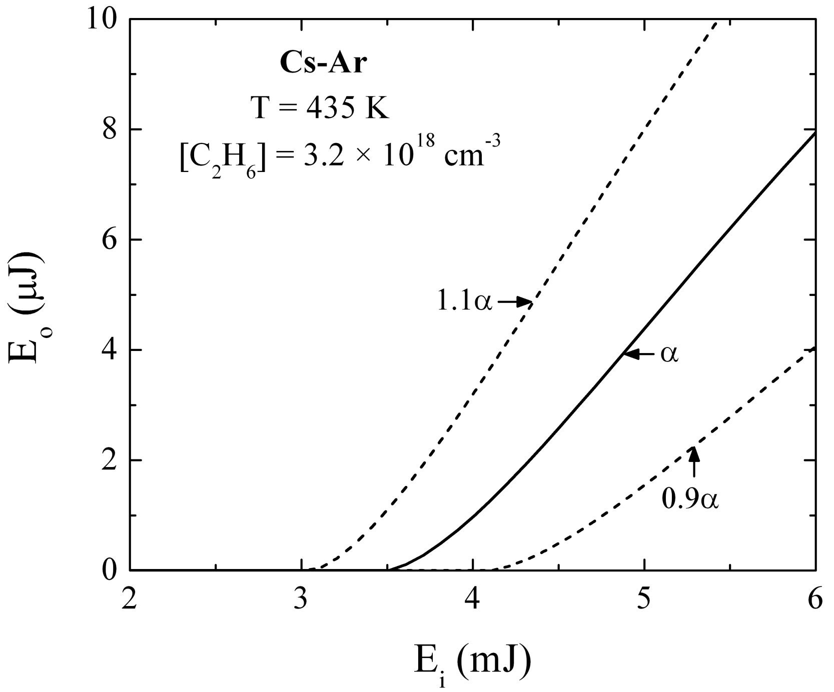

Figure 6.3: Predicted output pulse energy E_o as a function of incident pump energy E_i for $\alpha = 8.7 \times 10^{-3}$ cm^{-1} (0.9α), 9.7×10^{-3} cm^{-1} (α), and 10.7×10^{-3} cm^{-1} (1.1α).

The predictions presented in Fig. 6.3 illustrate the sensitivity of threshold and slope efficiency to the absorption coefficient. It is precisely this level of sensitivity that makes the laser itself such an excellent probe of the photoassociation and laser kinetics. This result corroborates the observed experimental observation of a ~6% increase in α at 836.7 nm manifesting in a ~28% decrease in threshold (in terms of E_i) when Kr is added to a Cs-Ar mixture as described in Subsection 5.3.2.

Because the incident photon density is paired with α in the rate equations, the model is similarly sensitive to the transverse pump beam characteristics. Since the measurements of the incident pump pulses are accurate to within ±5%, the primary source of error in matching the model to experiment comes from the approximations made regarding the shape and size of the pump beam as described in Section 6.1. However, although this can complicate the model, it also highlights the importance of resonator design for most efficient coupling of the pump into the gain medium.

6.5 Model Predictions

Because the model is designed to give time-dependent results, one of the most powerful methods of exploring the laser kinetics is by observing how the populations in the various states change over time. Figure 6.4 shows the temporal behavior of the relevant atomic and molecular population after the arrival of a 6.5 mJ, temporally Gaussian 4 ns pump pulse arriving at time t = 0. The shaded region corresponds to the approximate FWHM of the incident pump field. The laser is operating as a four-level system with 852.1 nm output due to the absence of C_2H_6.

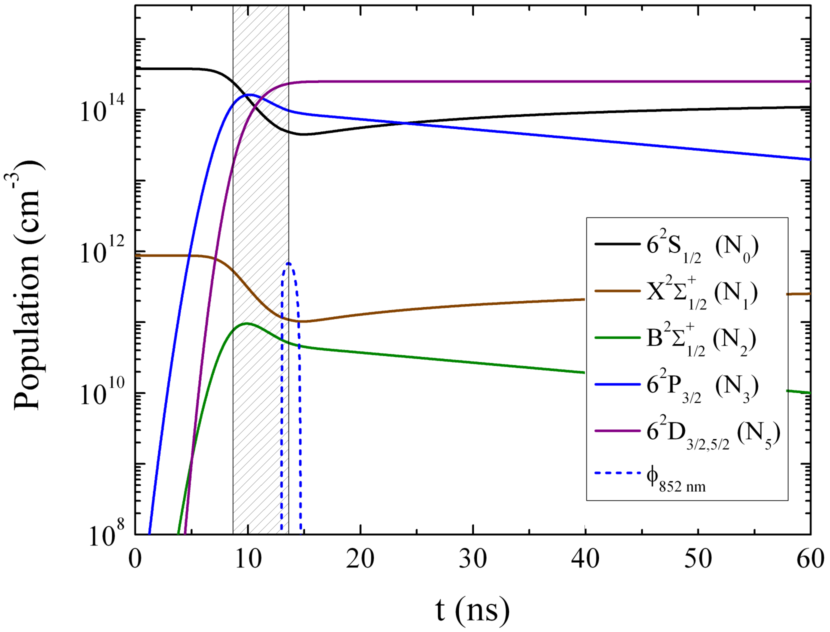

Figure 6.4: Predicted time dependence of the populations in various atomic and molecular states for a Cs-Ar mixture. The cell is at a temperature of T = 435 K ([Cs] = 3.8×10^{14} cm^{-3}) and interacts with a 6.5 mJ pump pulse which has a temporal FWHM indicated by the shaded region. Note that the ordinate is logarithmic.

For t≤0, the alkali population exists exclusively in the $6^2S_{1/2}$ and $X^2\Sigma^+_{1/2}$ ground states. After the pulse arrives, the excited state populations increase until inversion is observed between the $6^2S_{1/2}$ and $6^2P_{1/2}$ states. Shortly after laser threshold is reached, gain clamping is observed and the photon density at 852 nm increases rapidly. At these pump intensities, a significant portion of the population is excited to the $6^2D_{3/2,5/2}$ states. For t$\gtrsim$20 ns, the pump pulse has exited the system and, shortly thereafter, inversion can no longer be maintained. This corresponds to the termination of laser action and is most readily observed by the sharp decrease in 894 nm photon density. The laser output is observed to have a temporal FWHM of ~1 ns. This is temporally narrower than the pump pulse and further corroborates the experimental results of Fig. 5.3, both supporting the validity of the model and further illustrating the high gain of the system. In the absence of the pump field, population never leaves the $X^2\Sigma^+_{1/2}$ and $^2S_{1/2}$ ground states and the system remains in thermal equilibrium. Similar results corresponding to the introduction of C_2H_6 ($[C_2H_6] = 3.1 \times 10^{18}$ cm^{-3}) are presented in Fig. 6.5 for an incident pump pulse energy of 4 mJ.

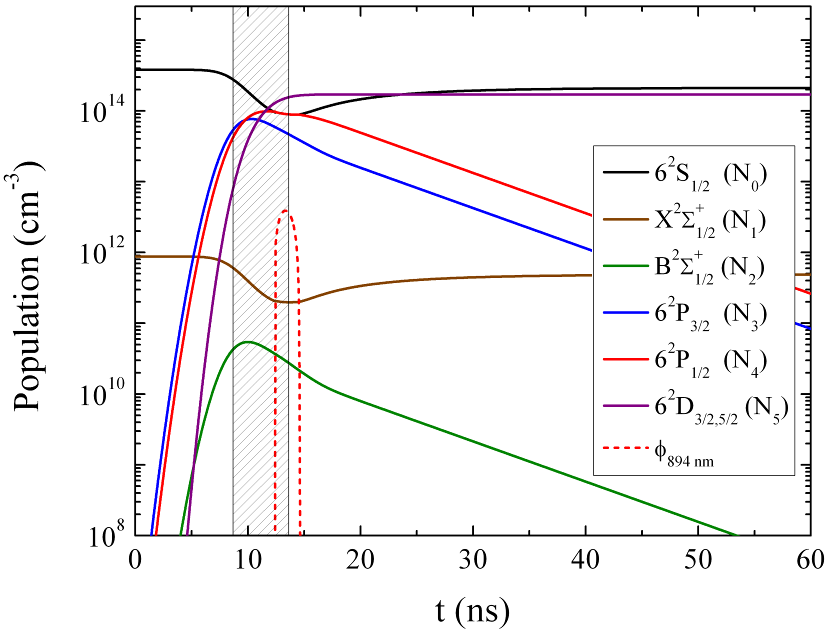

Figure 6.5: Predicted time dependence of the populations in various atomic and molecular states for a Cs-Ar-C_2H_6 gas mixture where $[C_2H_6] = 3.1 \times 10^{18}$ cm^{-3}. The cell is at a temperature of T = 435 K ([Cs] = 3.8×10^{14} cm^{-3}) and interacts with a 4 mJ pump pulse which has a temporal FWHM indicated by the shaded region. Note that the ordinate is logarithmic.

As indicated by Fig 6.5, the value of $[C_2H_6]$ determines the coupling between the $6^2P_{3/2}$ and $6^2P_{1/2}$ states as expected. In the absence of C_2H_6, the model predicts four-level operation with laser action at 852.1 nm. For sufficient values of $[C_2H_6]$, five-level operation was observed with laser emission at 894.3 nm. Figure 6.6 compares the output energy at each of these wavelengths as a function of [C_2H_6] with an 8 mJ pump pulse in the absence of excited state absorption ($\sigma_e = 0$). The results of Fig. 6.6 predict that 852.1 nm laser efficiency decreases with increasing [C_2H_6], as expected. The onset of 894 nm laser operation occurs at [C_2H_6]$\sim 1.7 \times 10^{17}$ cm^{-3}, but for [C_2H_6]$\geq 6.3 \times 10^{17}$ cm^{-3}, 852.1 nm output is essentially extinguished. However, between these values of [C_2H_6], it is predicted that laser output at both wavelengths may be observed simultaneously. This has been observed experimentally for Na-He mixtures and is intriguing from both physical and application standpoints [35]. Detailed characterization of this competition together with the possible observation of coherent effects between the beams would provide immediate insight into the laser kinetics. In terms of applications, multi-wavelength operation may be useful for a variety of tasks; a laser source capable of emitting simultaneously on the D_1 and D_2 lines of Na would be a valuable tool for the laser remote sensing community.

Figure 6.7 compares laser operation predicted for purely four-level ([C_2H_6] = 0) and five-level ([C_2H_6] $= 3.1 \times 10^{18}$ cm^{-3}) operation. For five-level operation, threshold is observed to be ∼3.5 mJ. The threshold for four-level operation is ∼6 mJ, a factor of ∼2 higher. This difference is attributed to the factor of two difference in the degeneracy ratios for the two laser transitions. Degradation in slope efficiency becomes significant for both curves in the region $E_i \gtrsim 10$ mJ and is attributed to the increasing rate of excited state absorption. It should be noted that excited state absorption does not eliminate the possibility for high power, CW XPALs as the pump intensities in these systems will be significantly smaller than those present in this work.

The following model predictions correspond to five-level operation in Cs-Ar-C_2H_6 because experimental data for this mixture is available at temperatures for which the strong-pump approximation is more accurate. Nevertheless, these results are all qualitatively representative of the model predictions under four-level operation due

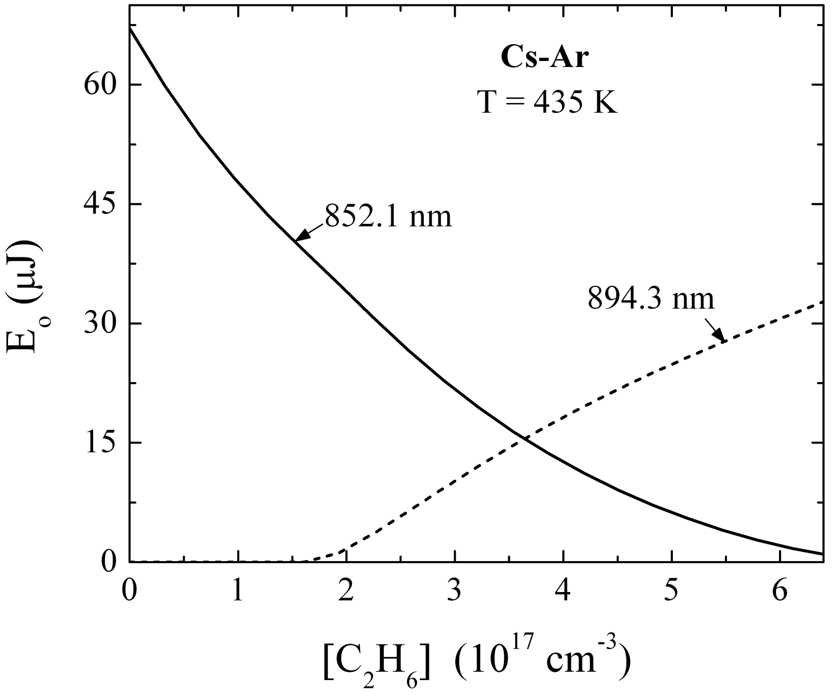

Figure 6.6: Predicted output pulse energy E_o at 852.1 nm (solid line) and 894.3 nm (dashed line) as a function of $[C_2H_6]$. Note that these results were obtained by assuming σ_e=0 and a pump pulse energy of 8 mJ when λ_p=836.7 nm.

to the similarity in kinetics.

The effect of varying only the output coupler reflectivity R is explored in Fig. 6.8. For values of R = 10%, 50%, and 90%, a pump energy threshold of ∼3.5 mJ is observed to remain approximately constant. This result further supports the validity of the model as these predictions corroborate the experimentally observed threshold insensitivity with variation of the output coupler. It should be noted that the rate equations do not include any terms which would explicity introduce this behavior.

As discussed previously, the most significant of the processes competing with laser operation appears to be excited state absorption. Most of the model predictions presented here assumed a value of $\sigma_e = 1 \times 10^{-17}$ cm^2. Because excited state absorption is an optically driven process, it becomes more significant at higher pump intensities. Figure 6.9 compares laser operation for σ_e values of 0, 5, and 10×10^{-18} cm^2. As expected, larger values of σ_e correspond to larger pump energy threshold and a decline

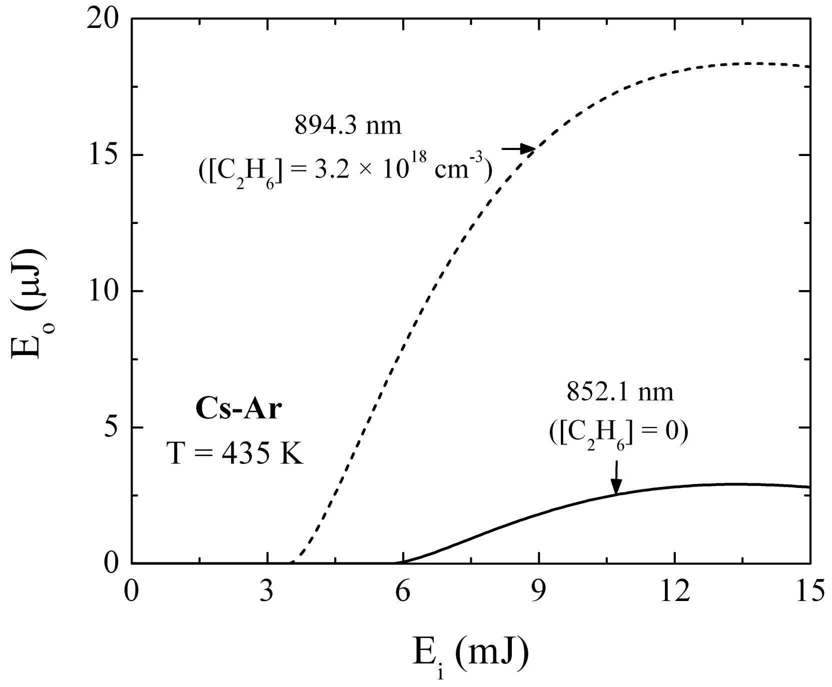

Figure 6.7: Predicted output pulse energy E_o as a function of incident pump energy E_i for four-level, 852.1 nm and five-level, 894.3 nm operation.

in slope efficiency. Threshold values of 2.6 mJ, 2.9 mJ, and 3.5 mJ are observed for $\sigma_e = 0$, 5, and 10×10^{-18} cm^2, respectively.

Figure 6.10 compares these model predictions with experimental results for five-level operation with $[C_2H_6] = 3.1 \times 10^{18}$ cm^{-3} for [Cs] $= 1.1 \times 10^{14}$ cm^{-3}, 3.8×10^{14} cm^{-3}, and 7.2×10^{14} cm^{-3} (T = 409 K, 435 K, and 450 K, respectively). For both the experimental data and the model predictions, threshold is approximately constant despite variations in temperature. The largest discrepancy in these results comes from a quantitative comparison of the thresholds, which is ∼0.44 mJ for the experimental data and ∼3.7 mJ, a factor of ∼8 larger, in the simulations.

The result of shifting the predicted data of Fig. 6.10 such that the threshold values approximately match those of the experimental data is presented in Fig. 6.11 and is useful as a means of qualitatively evaluating the slope efficiencies. The predicted curve for 409 K very closely matches that obtained experimentally. As the tem-

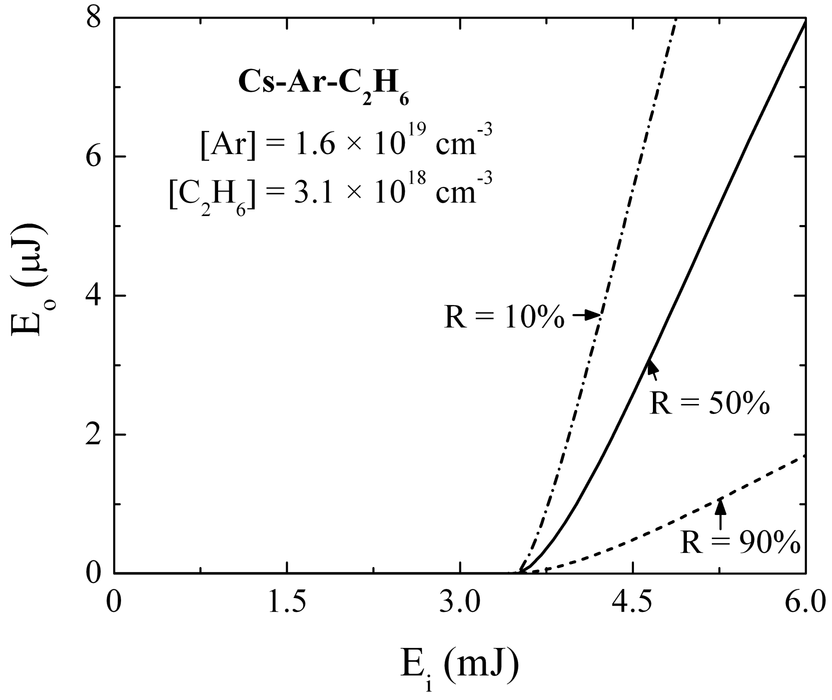

Figure 6.8: Predicted output pulse energy E_o as a function of incident pump energy E_i for five-level, 894.3 nm operation with output coupler reflectivities of 10%, 50%, and 90%.

perature increases, the model increasingly overstates slope efficiency. Despite these discrepancies, the slope efficiencies at each temperature are surprisingly accurate, indicating that much of the relevant physics is included in the model. However, as mentioned in Section 6.1, there are a number of assumptions and approximations which are necessary at this time. It is considered likely that a combination of rates and constants require adjustment so as to bring the predicted thresholds in line with the experimental data while maintaining agreement in slope efficiency.

As these results demonstrate, the rate equation model is a valuable tool for probing laser kinetics. In particular, the simulations provide insight into the impact of slight variations of the gas densities which would be difficult to realize experimentally. This is illustrated in Fig. 6.3 for changes in α and in Fig. 6.6, where interesting behavior is observed over a small range of [C_2H_6]. By employing the model in this way, it serves as an aid for selecting the critical problems to be pursued experimentally. At present,

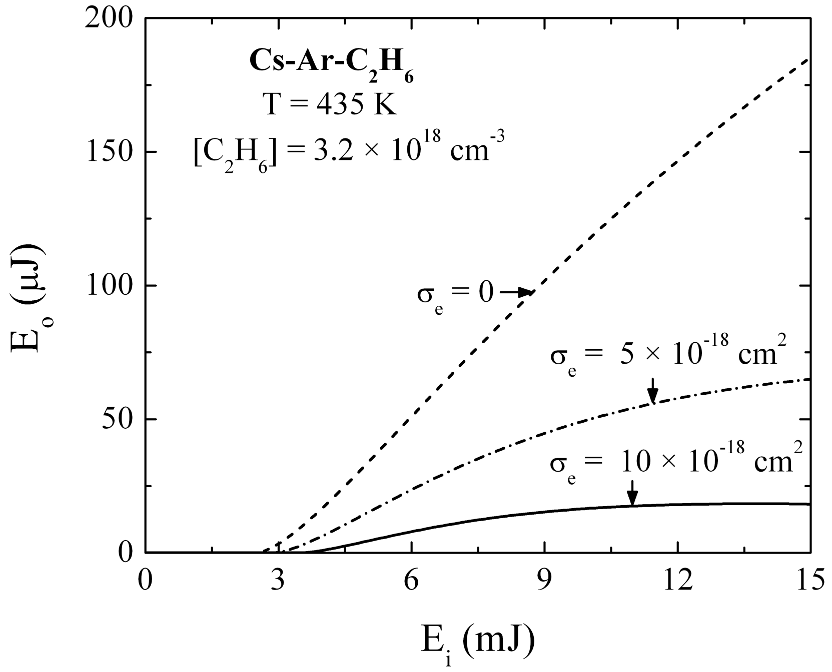

Figure 6.9: Predicted output pulse energy $\mathrm{E_o}$ as a function of incident pump energy $\mathrm{E_i}$ for $\sigma_e = 0$, 5, and 10×10^{-18} cm^2.

the most pressing experimental issues appear to be further investigation of three-body photoassociation (which can dramatically alter the absorption coefficient) and measurements of the cross section associated competitive processes such as excited state absorption.

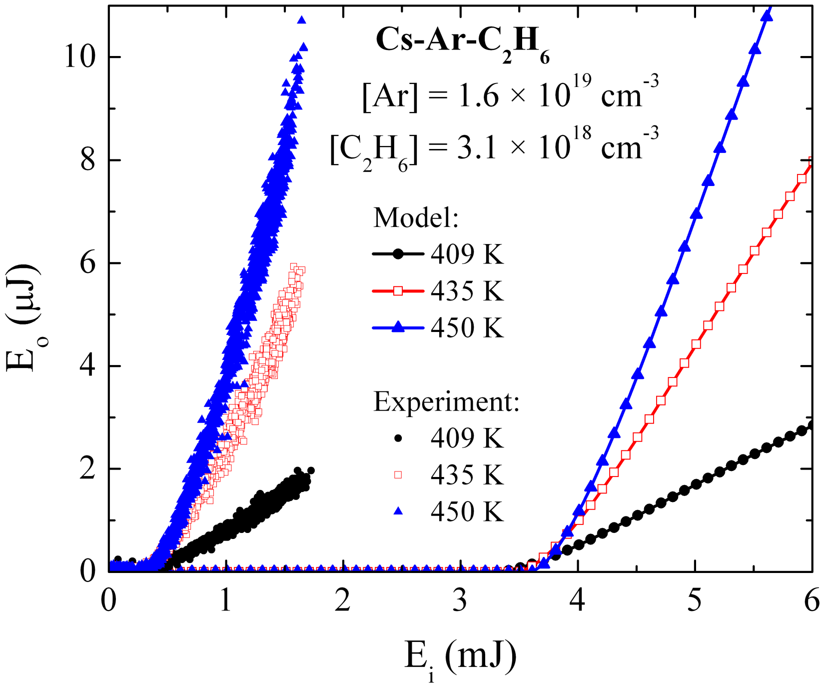

Figure 6.10: Comparison of model predictions for E$_o$ as a function of E$_i$ for Cs-Ar-C$_2$H$_6$ taken at gas cell temperatures of 409 K, 435 K, and 450 K (corresponding to [Cs] = 1.1 × 10^{14} cm^{-3}, 3.8 × 10^{14} cm^{-3}, and 7.2 × 10^{14} cm^{-3}, respectively).

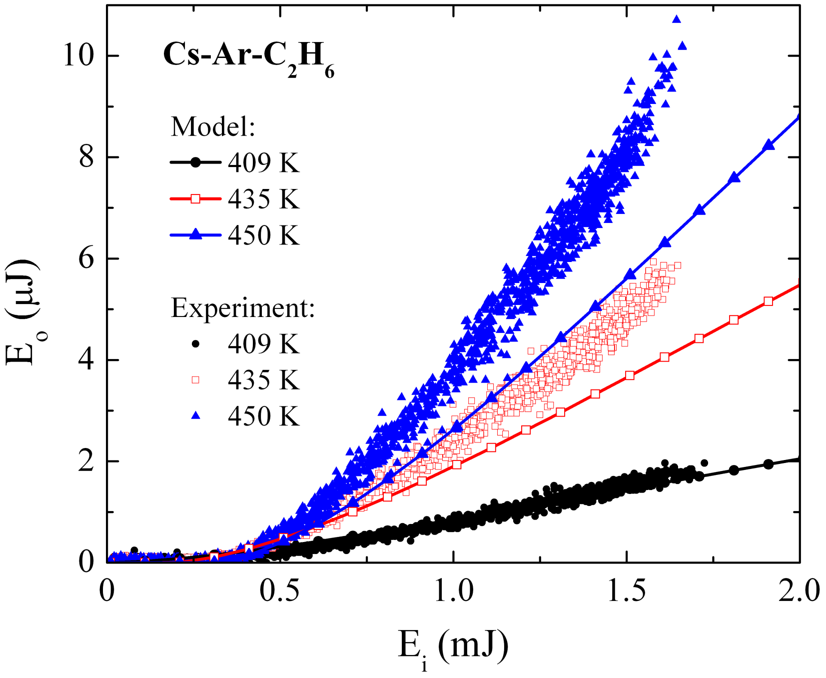

Figure 6.11: Data matching that of Fig. 6.10 with the exception that the predicted values of E$_i$ have been shifted by -3.3 mJ.

CHAPTER 7

CONCLUSION

The work presented in this thesis represents a new class of photoassociation lasers in which optically pumped transient collision pairs provide an efficient means of coupling energy into excited atomic states. Although most of the experiments described here employ Cs as the lasant species, this technique is applicable to *any* combination of species for which satellite behavior is observed. Correspondingly, these demonstrations have laid the groundwork for the development of a variety of new lasers which will employ alternative quasi-molecules.

Spectroscopically, these lasers are unique in that they involve molecular states which are never bound. Because of the relative complexity of extracting interaction potentials from free↔free transitions in comparison to free↔bound, and bound↔bound transitions, studies to date concerning photoassocation between two repulsive electronic molecular states have been limited. As illustrated by the new Cs-Ar B potential derived in this work, many of the assumptions and semiclassical approximations which were previously necessary are no longer required. This allows for a more thorough investigation of these systems than was previously possible. Furthermore, employment of the XPAL itself as a probe of the underlying physical processes provides unrivaled sensitivity which can be combined with these new numerical capabilities.

The experimental results obtained thus far for XPAL lasers are encouraging for future scaling efforts. The observation of identical (and in some cases even superior) values for threshold and slope efficiency for excimer-pumping as compared to direct atomic excitation demonstrates that there is no inherent disadvantage to introducing transient molecular states to the pumping scheme. Spectral bandwidths as large as ≥5 nm have been observed for excimer photoexcitation in both absorption and oscillator experiments, making the XPAL immediately compatible with commercial diode arrays. This avoids the reduction in pump efficiency and cost inherent to diode line narrowing and eliminates the need for frequency stabilization of the diode arrays as is necessary for direct atomic excitation. Nevertheless, the knowledge and publicity generated since the first three-level alkali laser was demonstrated in 2003 are invaluable in realizing high power, diode pumped XPALs.

It is quite possible that in the years to come these lasers will advance from the proof-of-concept work presented here to compact and robust commercial systems useful for a wide range of medical, industrial, and military applications. However, even if another technology supplants diode-pumped gas lasers as a promising approach to achieving such systems, successful demonstration of the XPAL concept will have conclusively shown how unbound, short-lived molecules can play a critical role in gas-phase kinetics.

REFERENCES

[1] D. Basting and G. Marowsky, *Excimer Laser Technology.* Berlin, Germany: Springer, 2005.

[2] D. Barton et al., "Report of the American Physical Society study group on boost-phase intercept systems for national missile defense: Scientific and technical issues," *Rev. Mod. Phys.*, vol. 76, no. 3, pp. S1–S424, 2004.

[3] H. Li et al., "Near 1 kW of continuous-wave power from a single high-efficiency diode-laser bar," *IEEE Photonic. Tech. Lett.*, vol. 19, no. 13, pp. 960–962, 2007.

[4] F. Bachmann, P. Loosen, and R. Poprawe, Eds., *High Power Diode Lasers.* New York, NY: Springer, 2007.

[5] J. Marmo, H. Injeyan, H. Komine, S. McNaught, J. Machan, and J. Sollee, "Joint high power solid state laser program advancements at Northrop Grumman," in *Proc. SPIE*, vol. 7195, 2009, p. 719507.

[6] W. F. Krupke, R. J. Beach, V. K. Kanz, and S. A. Payne, "Resonance transition 795-nm rubidium laser," *Opt. Lett.*, vol. 28, no. 23, pp. 2336–2338, Dec. 2003.

[7] R. J. Beach, W. F. Krupke, V. K. Kanz, S. A. Payne, M. A. Dubinskii, and L. D. Merkle, "End-pumped continuous-wave alkali vapor lasers: experiment, model, and power scaling," *J. Opt. Soc. Am. B*, vol. 21, no. 12, pp. 2151–2163, Dec. 2004.

[8] B. Zhdanov et al., "Optically pumped potassium laser," *Opt. Commun.*, vol. 270, no. 2, pp. 353–355, Sept. 2007.

[9] E. Walentynowicz, R. Phaneuf, and L. Krause, "Inelastic collisions between excited alkali atoms and molecules X. Temperature dependence of cross sections for ${}^2P_{1/2} \leftrightarrow {}^2P_{3/2}$ mixing in cesium, induced in collisions with deuterated hydrogens, ethanes, and propanes," *Can. J. Phys.*, vol. 52, no. 7, pp. 589–591, 1974.

[10] A. K. Majumdar and J. C. Ricklin, *Free-Space Laser Communications: Principles and Advances.* New York, NY: Springer, 2007.

[11] B. V. Zhdanov, T. Ehrenreich, and R. J. Knize, "A laser diode array pumped cesium vapor laser," in *Proc. SPIE Conf.*, 2007, p. 64540M.

[12] J. F. Sell, W. Miller, D. Wright, B. V. Zhdanov, and R. J. Knize, "Frequency narrowing of a 25 W broad area diode laser," *App. Phys. Lett.*, vol. 94, p. 051115, 2009.

[13] J. Zweiback and B. Krupke, "Rubidium and potassium alkali lasers," in *Proc. SPIE*, vol. 7196, 2009, p. 71960E.

[14] J. Pascale and J. Vandeplanque, "Excited molecular terms of the alkali-rare gas atom pairs," *J. Chem. Phys.*, vol. 60, no. 6, pp. 2278–2289, Mar. 1974.

[15] A. Tam, G. Moe, and W. Happer, "Particle formation by resonant laser light in alkali-metal vapor," *Phys. Rev. Lett.*, vol. 35, no. 24, pp. 1630–1633, 1975.

[16] B. V. Zhdanov and R. J. Knize, "Hydrocarbon-free potassium laser," *Electron. Lett.*, vol. 43, no. 19, pp. 1024–1025, 2007.

[17] N. G. Basov, V. A. Danilychev, and Y. M. Popov, "Stimulated emission in the vacuum ultraviolet region," *Sov. J. Quantum Electron.*, vol. 1, no. 1, pp. 18–22, 1971.

[18] P. W. Hoff, J. C. Swingle, and C. K. Rhodes, "Demonstration of temporal coherence, spatial coherence, and threshold effects in the molecular xenon laser," *Opt. Comm.*, vol. 8, no. 2, pp. 128–131, 1973.

[19] P. W. Hoff, J. C. Swingle, and C. K. Rhodes, "Observations of stimulated emission from high-pressure krypton and argon/xenon mixtures," *Appl. Phys. Lett.*, vol. 23, p. 245, 1973.

[20] S. K. Searles and G. A. Hart, "Stimulated emission at 281.8 nm from XeBr," *Appl. Phys. Lett.*, vol. 27, no. 4, pp. 243–245, Aug. 1975.

[21] J. J. Ewing and C. A. Brau, "Laser action on the $^2\Sigma^+_{1/2} \rightarrow ^2 \Sigma^+_{1/2}$ bands of KrF and XeCl," *Appl. Phys. Lett*, vol. 27, no. 6, pp. 350–352, Sept. 1975.

[22] J. G. Eden, "From N_2 (337 nm) to high-order harmonic generation: 40 years of coherent source development in the UV and VUV," *IEEE J. Sel. Topics Quantum Electron.*, vol. 6, no. 6, pp. 1051–1060, 2000.

[23] J. T. Verdeyen, *Laser Electronics*, 3rd ed. Englewood Cliffs, NJ: Prentice Hall, 1994.

[24] H. H. Michels and L. A. Hobbs, "The electronic structure of ArF and Ar_2F^*," *Chem. Phys. Lett.*, vol. 48, no. 1, pp. 158–161, 1977.

[25] A. V. Phelps, "Tunable gas laser utilizing ground state dissociation," JILA, Tech. Rep. 110, 1972.

[26] G. York and A. Gallagher, "High power gas laser on alkali-dimer A-X band radiation," JILA, Tech. Rep. 114, 1974.

[27] S. Shahdin, K. Ludewigt, and B. Wellegehausen, "Photodissociative generation of population inversion in alkali noble gas excimer systems," *IEEE J. Quantum Electron.*, vol. 17, no. 7, pp. 1276–1280, 1981.

[28] S. Y. Ch'en and M. Takeo, "Broadening and shift of spectral lines due to the presence of foreign gases," *Rev. Mod. Phys.*, vol. 29, no. 1, pp. 20–73, Jan. 1957.

[29] R. E. M. Hedges, D. L. Drummond, and A. Gallagher, "Extreme-wing line broadening and Cs-inert-gas potentials," *Phys. Rev. A*, vol. 6, no. 4, pp. 1519–1544, Oct. 1972.

[30] S. Chilukuri, "Selective optical excitation and inversions via the excimer channel: Superradiance at the thallium green line," *App. Phys. Lett.*, vol. 34, no. 4, pp. 284–286, 1979.

[31] S. N. Atamas, L. M. Bukshpun, Yu. V. Koptev, E. L. Latush, and M. F. Sém, "Stimulated emission of the 535 nm thallium line as a result of quasiresonant optical pumping of a Tl-He mixture by radiation from a recombination He-Ca laser," *Sov. J. Quantum Electron.*, vol. 14, no. 2, pp. 161–162, 1984.

[32] R. H. Page, R. J. Beach, V. K. Kanz, and W. F. Krupke, "Multimode-diode-pumped gas (alkali-vapor) laser," *Opt. Lett.*, vol. 31, no. 3, pp. 353–355, 2006.

[33] B. Zhdanov and R. J. Knize, "Diode-pumped 10 W continuous wave cesium laser," *Opt. Lett.*, vol. 32, no. 15, pp. 2167–2169, Aug. 2007.

[34] S. S. Q. Wu, T. F. Soules, R. H. Page, S. C. Mitchell, V. Keith Kanz, and R. J. Beach, "Hydrocarbon-free resonance transition 795-nm rubidium laser," *Opt. Lett.*, vol. 32, no. 16, pp. 2423–2425, 2007.

[35] R. V. Markov, A. I. Plekhanov, and A. M. Shalagin, "Population inversion induced by collisions in a two level system under nonresonance optical excitation," *Phys. Rev. Lett.*, vol. 88, no. 21, p. 213601, 2002.

[36] S. Y. Ch'en and A. T. Lonseth, "Pressure effects of rare gases on the absorption line Ca 4227. I. The effects of argon and helium," *Phys. Rev. A*, vol. 3, no. 3, pp. 946–950, 1971.

[37] S. Y. Ch'en, M. R. Atwood, and T. H. Warnock, "Collision induced satellite bands of In and Tl lines in the presence of rare gases," *Physica*, vol. 27, pp. 1170–1176, 1961.

[38] O. Jefimenko and S. Y. Ch'en, "Modifications of the Cs absorption spectrum due to interatomic interactions," *J. Chem. Phys*, vol. 26, no. 4, pp. 913–919, 1957.

[39] C. L. Chen and A. V. Phelps, "Absorption coefficients for the wings of the first two resonance doublets of cesium broadened by argon," *Phys. Rev. A*, vol. 7, no. 2, pp. 470–479, Feb. 1973.

[40] J. Tellinghuisen, *Photodissociation and Photoionization.* New York, NY: John Wiley & Sons, 1985, ch. The Franck-Condon principle in bound-free transitions, pp. 299–369.

[41] R. B. Jones, J. H. Schloss, and J. G. Eden, "Excitation spectra for the photoassociation of Kr–F and Xe–I collision pairs in the ultraviolet (208–258 nm)," *J. Chem. Phys.*, vol. 98, no. 6, pp. 4317–4334, 1993.

[42] F. Shen, "Theoretical investigation of photoassociative excitation spectroscopy of xenon monoiodide," Ph.D. dissertation, University of Illinois at Urbana-Champaign, 2004.

[43] J. W. Cooley, "An improved eigenvalue corrector formula for solving the schrodinger equation for central fields," *Math. Comput.*, vol. 15, no. 76, pp. 363–374, 1961.

[44] R. A. Buckingham, *Quantum Theory I, Elements*, D. R. Bates, Ed. New York, NY: Academic Pess, 1961.

[45] W. R. Jarmain, "Realistic Franck-Condon factors and related integrals for diatomic molecules–I. Method," *J. Quant. Spectrosc. Radiat. Transfer*, vol. 11, no. 5, pp. 421–426, 1971.

[46] D. A. McQuarrie and J. D. Simon, *Physical Chemistry: A Molecular Approach.* Saulsalito, CA: University Science Books, 1997.

[47] D. Cvetko, A. Lausi, A. Morgante, F. Tommasini, P. Cortona, and M. G. Dondi, "A new model for atom-atom potentials," *J. Chem. Phys.*, vol. 100, no. 3, pp. 2052–2057, 1994.

[48] W. E. Baylis, "Semiempirical, pseudopotential calculation of alkali–noble-gas interatomic potentials," *J. Chem. Phys.*, vol. 51, no. 6, pp. 2665–2679, 1969.

[49] *Handbook of Chemistry and Physics*, 90th ed. Boca Raton, FL: CRC Press, 2009-2010, ch. Index of Refraction of Air, pp. 10–252.

[50] D. A. Steck, "Cesium D line data," Oct. 2003, unpublished.

[51] D. A. Steck, "Rubidium 87 D line data," Oct. 2003, unpublished.

[52] T. M. Spinka, "Nonlinear optical processes and the nearest neighbor distribution in rubidium vapor," Ph.D. dissertation, University of Illinois at Urbana-Champaign, 2010.

[53] A. M. Farkas and J. G. Eden, “Pulsed dye amplification and frequency doubling of single longitudinal mode semiconductor lasers,” *IEEE J. Quant. Elect.*, vol. 29, no. 12, pp. 2923–2927, 1993.

[54] D. A. Hostutler and W. L. Klennert, “Power enhancement of a rubidium vapor laser with a master oscillator power amplifier,” *Opt. Exp.*, vol. 16, no. 11, pp. 8050–8053, 2008.

[55] J. D. Readle, C. J. Wagner, J. T. Verdeyen, D. L. Carroll, and J. G. Eden, “Lasing in Cs at 894.3 nm pumped by the dissociation of CsAr excimers,” *Electron. Lett.*, vol. 44, no. 25, pp. 1466–1467, 2008.

[56] J. D. Readle, C. J. Wagner, J. T. Verdeyen, T. M. Spinka, D. L. Carroll, and J. G. Eden, “Pumping of atomic alkali lasers by photoexcitation of a resonance line blue satellite and alkali-rare gas excimer dissociation,” *App. Phys. Lett.*, vol. 94, p. 251112, 2009.

[57] J. D. Readle, J. T. Verdeyen, J. G. Eden, S. J. Davis, K. L. Galbally-Kinney, W. T. Rawlins, and W. J. Kessler, “Cs 894.3 nm laser pumped by photoassociation of Cs-Kr pairs: excitation of the Cs D_2 blue and red satellites,” *Opt. Lett.*, vol. 34, no. 23, pp. 3638–3640, 2009.

[58] D. C. Morton, “Atomic data for resonance absorption lines. II. Wavelengths longward of the Lyman limit for heavy elements,” *Astrophys, J. Suppl. Ser.*, vol. 130, pp. 403–436, Oct. 2000.

[59] J. D. Readle, J. G. Eden, J. T. Verdeyen, and D. L. Carroll, “Four level, atomic Cs laser at 852.1 nm with a quantum efficiency above 98%: Observation of three body photoassociation,” *Appl. Phys. Lett.*, to be published.

[60] Z. J. Jabbour, R. K. Namiotka, J. Huennekens, M. Allegrini, S. Milošević, and F. De Tomasi, “Energy-pooling collisions in cesium: $6P_J + 6P_J \rightarrow 6S + (nl = 7P, 6D, 8S, 4F)$,” *Phys. Rev. A*, vol. 54, no. 2, pp. 1372–1384, 1996.

[61] C. Vadla, K. Niemax, and J. Brust, “Energy pooling in cesium vapor,” *Z. Phys. D.*, vol. 37, no. 3, pp. 241–247, 1996.

[62] T. Ohno, T. Okuda, and J. Yamada, “Two-photon ionization of excited cesium atoms by ruby laser light,” *J. Phys. Soc. Jpn.*, vol. 45, no. 1, pp. 244–246, 1978.

[63] J. Lahiri and S. T. Manson, “Oscillator-strength distributions for discrete and continuum transitions of excited states of cesium,” *Phys. Rev. A*, vol. 33, no. 5, pp. 3151–3165, 1986.

[64] J. G. Eden, B. E. Cherrington, and J. T. Verdeyen, “Optical absorption and fluorescence studies in high pressure cesium-xenon mixtures,” *IEEE J. Quant. Elect.*, vol. 12, no. 11, pp. 698–704, Nov. 1976.

[65] E. S. Hrycyshyn and L. Krause, “Inelastic collisions between excited alkali atoms and molecules. VII. Sensitized fluorescence and quenching in mixtures of rubidium with H_2, HD, D_2, N_2, CH_4, CD_4, C_2H_4, and C_2H_6,” *Can. J. Phys.*, vol. 48, no. 22, pp. 2761–2768, 1970.

[66] W. Koechner, *Solid-State Laser Engineering*, 4th ed. New York, NY: Springer, 1996.

[67] R. J. Rafac and C. E. Tanner, “Measurement of the ^{133}Cs $6p^2P_{1/2}$ state hyperfine structure,” *Phys. Rev. A*, vol. 56, no. 1, pp. 1027–1030, 1997.

[68] E. Bernabeu and J. M. Alvarez, “Shift and broadening of hyperfine components of the first doublet of cesium perturbed by foreign gases,” *Phys. Rev. A*, vol. 22, no. 6, pp. 2690–2695, 1980.